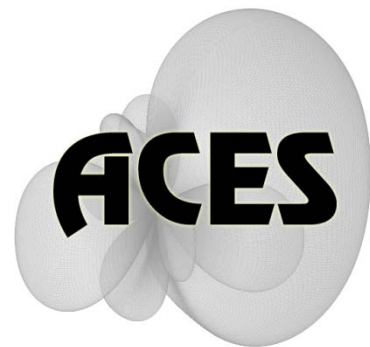**GENERAL PURPOSE AND SCOPE:** The Applied Compu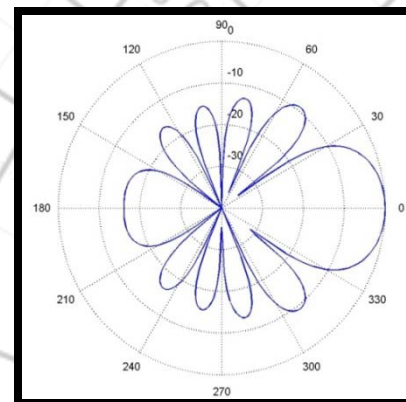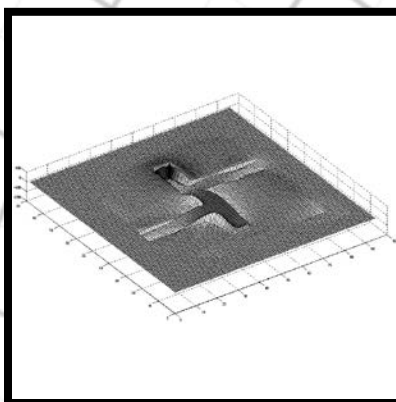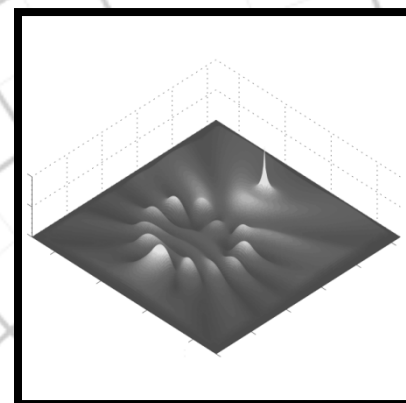tational Electromagnetics Society *(ACE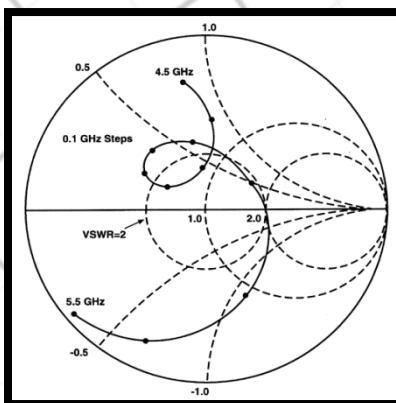S)* Journal hereinafter known as the *ACES Journal* is devoted to the exchange of information in computational electromagnetics, to the advancement of the state-of-the art, and the promotion of related technical activities. The primary objective of the information exchange is to inform the scientific community on the developments of new computational electromagnetics tools and their use in electrical engineering, physics, or related areas. The technical activities promoted by this publication include code validation, performance analysis, and input/output standardization; code or technique optimization and error minimization; innovations in solution technique or in data input/output; identification of new applications for electromagnetics modeling codes and techniques; integration of computational electromagnetics techniques with new computer architectures; and correlation of computational parameters with physical mechanisms.

SUBMISSIONS: The *ACES Journal* welcomes original, previously unpublished papers, relating to applied computational electromagnetics. Typical papers will represent the computational electromagnetics aspects of research in electrical engineering, physics, or related disciplines. However, papers which represent research in applied computational electromagnetics itself are equally acceptable.

Manuscripts are to be submitted through the upload system of *ACES* web site http://aces.ee.olemiss.edu See "Information for Authors" on inside of back cover and at *ACES* web site. For additional information contact the Editor-in-Chief:

Dr. Atef Elsherbeni
Department of Electrical Engineering
The University of Mississippi
University, MS 386377 USA
Phone: 662-915-5382
Email: atef@olemiss.edu

SUBSCRIPTIONS: All members of the Applied Computational Electromagnetics Society are entitled to access and download the *ACES Journal* any published journal article available at http://aces.ee.olemiss.edu. Printed issues of the *ACES Journal* are delivered to institutional members. Each author of published papers receives a printed issue of the *ACES Journal* in which the paper is published.

Back issues, when available, are $50 each. Subscription to *ACES* is through the web site. Orders for back issues of the *ACES Journal* and change of address requests should be sent directly to *ACES* office at:

Department of Electrical Engineering
The University of Mississippi
University, MS 386377 USA
Phone: 662-915-7231
Email: aglisson@olemiss.edu

Allow four weeks advance notice for change of address. Claims for missing issues will not be honored because of insufficient notice, or address change, or loss in the mail unless the *ACES* office is notified within 60 days for USA and Canadian subscribers, or 90 days for subscribers in other countries, from the last day of the month of publication. For information regarding reprints of individual papers or other materials, see "Information for Authors".

APPLIED
COMPUTATIONAL
ELECTROMAGNETICS
SOCIETY
JOURNAL

April 2011
Vol. 26 No. 4
ISSN 1054-4887

APRIL 2011 REVIEWERS

Ahmed Abdelrahman

Iftikhar Ahmed

Guido Ala

Saad Alhossin

Mohamed Bakr

Sami Barmada

Raghvendra Chaudhary

William Coburn

Jorge Costa

Khaled ElMahgoub

Nikolaos Kantartzis

Fadi Khalil

Michiko Kuroda

Fernando Las-Heras

David Lautru

Mun Soo Lee

Angelo Liseno

Mingyu Lu

Ricardo Matias

Zahera Mekkioui

Ivor Morrow

Andrew Peterson

Dr. Pichon

Luca Rienzo

Binay Sarkar

Gonul Turhan-Sayan

Katherine Siakavara

Daniela Staiculescu

Ahmet Turk

Yuhao Wang

Steven Weiss

Wenhua Yu

THE APPLIED COMPUTATIONAL ELECTROMAGNETICS SOCIETY

JOURNAL

TABLE OF CONTENTS

Design of UWB Antennas to Monitor Cardiac Activity

Erika Pittella, Paolo Bernardi, Marta Cavagnaro, Stefano Pisa, and Emanuele Piuzzi

Department of Information Engineering, Electronics, and Telecommunications
Sapienza University of Rome, Rome, Italy
pisa@die.uniroma1.it

Abstract — This paper presents two novel ultra wideband (UWB) printed antennas designed to be part of a UWB radar system for cardiac activity monitoring. The two antennas have the same shape but differ in terms of dielectric substrate and dimensions and are designed to be used one in a wearable and the other in non-wearable (fixed) radar. With regard to the fixed antenna, numerical results show an optimum fidelity factor and an almost constant group delay in the 3.1 - 10.6 GHz frequency band. As concerns the wearable antenna, numerical results obtained considering the antenna placed in the vicinity of a box model of the thorax, containing a spherical model of the heart, show that small heart movements can be detected. Eventually, the two antennas have been realized and measured by means of a vector network analyzer finding a return loss lower than -10 dB in the 3.1 - 10.6 GHz frequency band with a good agreement between simulations and measurements. Also, measurements of the fixed antenna gain and radiation pattern, performed in an anechoic chamber, show a good agreement with simulations.

Index Terms — Heart-activity monitoring, remote sensing, UWB antenna.

I. INTRODUCTION

The cardiac activity involves changes in shape, dimension, and dielectric properties of the heart muscle. These variations can be monitored by using a UWB radar system equipped with a suitable antenna. In a possible arrangement, the radar transmits very short pulses towards the human thorax and receives the echoes containing information on the heart variations [1, 2]. The remote monitoring of cardiac activity is a crucial and useful application in various situations. For example, in emergency rooms or intensive care units it is more comfortable for the patient with respect to conventional techniques (e.g., electrocardiogram - ECG). Moreover, it can be performed in a continuous way, becoming very useful in the monitoring of pathologies of the cardiac apparatus, for home therapy, or hospital confinement. Finally, it allows monitoring of patients with burns or chemical contaminations without contacting electrodes.

With reference to UWB radar systems, their main advantages are the very high resolution, the low power spectral density, and the low electromagnetic interference with other systems; furthermore, UWB radars are based on a quite low cost technology. In February 2002, the Federal Communications Commission (FCC) gave the permission for the development of new products incorporating UWB technology. To this day, the FCC allocated a 7.5 GHz band in the range from 3.1 GHz to 10.6 GHz [3, 4] providing a mask for the maximum power spectral density (PSD), settled to the value of -41.3 dBm/MHz, over the whole band. These low levels are due to the fact that UWB systems work in a region of the spectrum in which other services already operate. UWB radar systems can be realized in hybrid or monolithic microwave integrated circuit (MMIC) technology with very small dimensions so that portable (wearable) radars can be built. Otherwise, in many applications, the dimensions are not a strong constrain and the radar can be fixed on the roof or on a wall of a room. These two

applications will need antennas with different dimensions and properties.

For this reason, in this work, two novel UWB antennas have been proposed and designed, one for wearable and one for fixed radars.

II. ANTENNAS DESIGN

A. Antenna geometry

The main goal of the two antenna designs is to obtain a return loss lower than -10 dB in the 3.1 - 10.6 GHz band. Moreover, the wearable antenna has to be portable and light while for the fixed one the directivity constrain is more important. To fulfill these requirements, printed UWB antennas can be used [5-11]. In particular, among these antennas, the microstrip-fed monopole structure has been considered, where the radiating element and the feeding microstrip line are realized over one of the substrate faces, while a suitable ground plane is etched on the other face. Such structure has been chosen considering the broadband and good radiation properties of the printed heart monopole antenna [5]. Finally, taking into account the directivity performance of the truncated planar configuration proposed in [12], a half-heart shape geometry has been chosen.

B. Antenna optimization

The considered half-heart shape geometry is shown in Fig. 1. The radiator is located on the top layer of the substrate and the ground plane on the bottom layer. The dielectric substrates utilized in this project are: Rogers RO4003 with relative permittivity $\varepsilon_{r1} = 3.38$, thickness $h_1 = 0.508$ mm, and copper thickness $t_1 = 0.035$ mm, and Rogers RT6010 with $\varepsilon_{r2} = 10.2$, thickness $h_2 = 0.640$ mm, and copper thickness $t_2 = 0.035$ mm, for the antenna to be used in fixed and wearable systems, respectively. With reference to the other dimensions, l and w are the height and width of the substrate. The shape of the half heart on the top layer is obtained through a semicircle of radius r_c and through a three control-points spline defined assigning the initial point $P_i(x_i, y_i, z_i)$, the final point $P_f(x_f, y_f, z_f)$, and the central point $P_s(x_s, y_s, z_s)$. The shape of the ground on the bottom layer of the antenna is also obtained through a three control-points spline specular to the previous one (see Fig. 1). It is worth noting that, in all the simulations, the feeding microstrip line has been

curved away from the edge of the structure to facilitate the connection with the coaxial feed line.

The antenna geometry has been optimized through parametric simulations using CST Microwave Studio® software [13]. In these simulations the antenna parameters have been varied inside realistic ranges and the $S_{11}(f)$ results
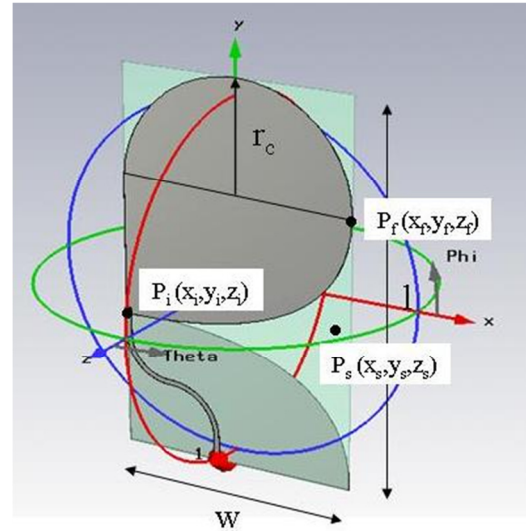
Fig. 1. Geometry of the proposed antenna.

have been analyzed. Only geometries giving $S_{11}(f)$ absolute values lower than -10 dB ($\rho = 0.316$) between $f_1 = 3.1$ GHz and $f_2 = 10.6$ GHz band have been considered and, among those selected, the one maximizing the cost function:

$$C = \frac{1}{(f_2 - f_1)} \int_{f_1}^{f_2} \left(\frac{\rho - |S_{11}(f)|}{\rho} \right) df, \qquad (1)$$

has been chosen.

Among the antenna parameters, the central control-point of the spline (x_s, y_s) plays a fundamental role for the antenna matching. This parameter has been varied at 1 mm step in the 10-50 mm range. Figure 2 shows the results for $l = 85$ mm, $w = 50$ mm, $r_c = 25$ mm, $x_s = 50$ mm and for three values of the y_s parameter.

The best value of the cost function is obtained with $y_s = 30$ mm and corresponds to $C = 0.633$.

The final antenna dimensions are: $l_1 = 85.0$ mm, $w_1 = 50$ mm, $r_{c1} = 25$ mm, $x_{s1} = 50$ mm, $y_{s1} = 30$ mm for the fixed antenna, and $l_2 = 48.5$ mm, $w_2 = 25$ mm, $r_{c2} = 12.5$ mm, $x_{s2} = 25$ mm, $y_{s2} = 20$ mm for the wearable one.
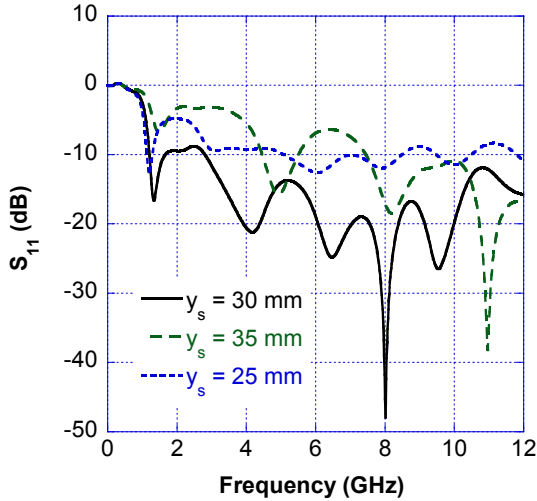
Fig. 2. Results of a parametric analysis.

III. NUMERICAL SIMULATION RESULTS

A. Antennas performances in free space

Figure 3 shows the return loss as a function of the frequency for the two designed UWB antennas. The obtained results indicate that the antennas have a return loss below -10 dB in the 3.1-10.6 GHz frequency band.
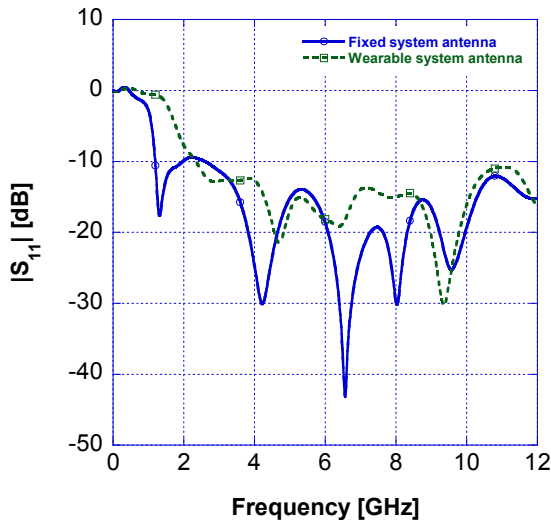
Fig. 3. Return loss of the two proposed antennas.

B. Fixed system antenna

Concerning the antenna radiation pattern, Fig. 4 shows polar plots on the x-y vertical plane at 4, 6, 8, and 10 GHz for the antenna designed for the fixed system. The plot highlights that the direction

of maximum radiation is close to the x direction of Fig. 1 with a -3 dB aperture varying between 55° and 58.5°.

Figure 5 shows the peak gain behavior as a function of the frequency as well as the φ value ($\theta = 90°$) for which the gain achieves its maximum value. As it can be seen, the gain values increase with the frequency. In particular, the minimum value is 4.6 dBi at 3.0 GHz, while the maximum is 9.4 dBi at 11 GHz; these gain values are comparable with the gain values of other UWB antennas reported in literature [8].
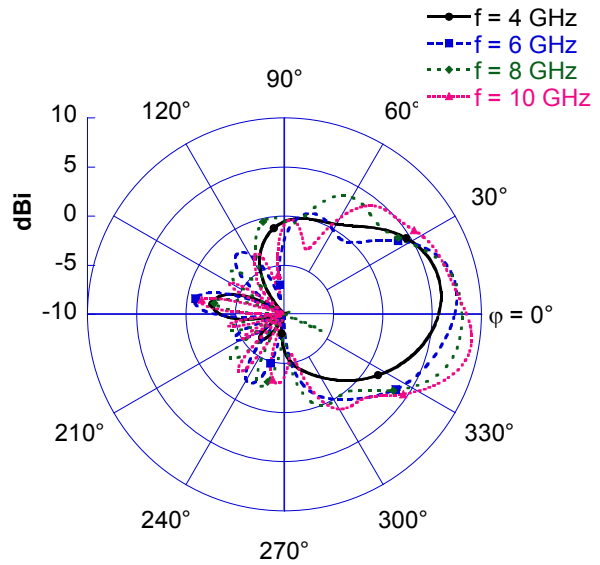
Fig. 4. Polar plot of the gain at 8 GHz for the fixed antenna.

Concerning the direction of maximum radiation, Fig. 5 shows that it is almost constant with the frequency with variations mostly within ± 10 °.

An important parameter of a UWB antenna is the fidelity factor that is the peak value of the cross correlation function between the observed pulse $s_2(t)$ (electric field (E_θ)), at a given distance from the antenna, and the excited pulse $s_1(t)$ (input voltage) [14, 15]:

$$F = \max_{\tau} \frac{\int_{-\infty}^{+\infty} s_1(t)\, s_2(t+\tau)dt}{\sqrt{\int_{-\infty}^{+\infty} s_1^2(t)dt}\sqrt{\int_{-\infty}^{+\infty} s_2^2(t)dt}}, \qquad (2)$$

where τ is the delay that maximizes F in (2). Considering that, for an antenna, the time behavior of the radiated electric field is an approximation of the derivative of the input excitation,

$s_1^{'}(t) = ds_1 / dt$ can be used in place of $s_1(t)$ [14]. The UWB signal used in [14, 16] is assumed to excite the designed antenna. This UWB signal is the 5th-derivative of the Gaussian pulse, given by:

$$s_1(t) = k\left(-\frac{t^5}{\sqrt{2\pi}\sigma^{11}} + \frac{10t^3}{\sqrt{2\pi}\sigma^9} - \frac{15t}{\sqrt{2\pi}\sigma^7} \right) e^{\left(-\frac{t^2}{2\sigma^2} \right)}, \quad (3)$$

where k is a constant which can be chosen to comply with the peak power spectral density allowed by the FCC, while σ is taken equal to 51 ps to ensure that the spectrum shape complies with the FCC spectral mask. The fidelity factor has been calculated at a distance from the antenna of 100 cm and for various directions. Results concerning the fidelity ($s_1(t)$ and its derivative) are summarized in Tab. 1. The values reported in the table highlight a very high fidelity factor of the proposed antenna, for all the considered directions apart from small θ angles.

Another important goal of the UWB antenna design is to achieve a linear dependence of the radiated field phase as a function of the frequency in order to minimize pulse distortion. The parameter that describes the phase response of the antenna is the group delay, defined as the negative derivative of the phase response with respect to the frequency. Figure 6 shows the group delay values as calculated from the time-domain response. The figure reveals that the antenna group delay is almost constant, with less than 0.1 ns fluctuations, across the whole considered frequency band.

C. Wearable antenna in the presence of a box model of the thorax

In order to check the ability of the wearable antenna to monitor the heart activity, the radiating structure has been placed 1 cm from a box model

of the chest (9×9×6 cm) with the direction of maximum radiation toward the thorax (see Fig. 7).

Inside the box, at a depth of 3 centimeters, a sphere of variable radius (from 20 to 25 mm) has been placed to simulate the presence of the heart.
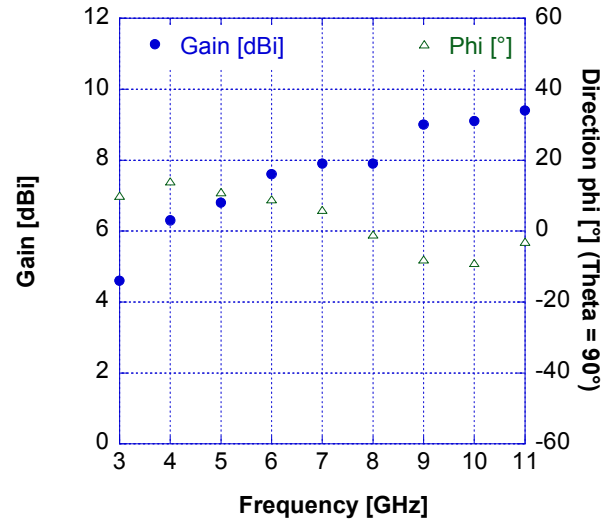
Fig. 5. Peak gain behavior of the fixed system antenna and direction of maximum gain as a function of the frequency.

The thorax is constituted by an equivalent body tissue whose parameters have been taken from those recommended by the IEEE SCC-34/SC-2 [17]. The values in [17] have been interpolated by using a Cole-Cole equation [18] with $\varepsilon_s = 993$, $\varepsilon_\infty = 54$, and relaxation frequency $f_r = 20.8$ MHz. For the sphere representing the heart, $\varepsilon_r = 48.62$ and $\sigma = 6.12$ S/m [19, 20] have been considered.

To simulate the heart movements, a set of simulations have been performed varying the sphere radius and measuring the received voltage at the feed point considering as a source signal the 5th derivative of the Gaussian pulse.

Table 1. Simulated fidelity of the proposed antenna.

	Probe position (xy plane)	Fidelity $s_1(t)$	Fidelity $s_1^{'}(t) = ds_1 / dt$	Probe position (xz plane)	Fidelity $s_1(t)$	Fidelity $s_1^{'}(t) = ds_1 / dt$
Antenna (fixed system)	$\theta = 90°$ $\varphi = 0°$	0.947	0.983	$\varphi = 0°$ $\theta = 0°$	0.700	0.706
	$\theta = 90°$ $\varphi = 30°$	0.961	0.964	$\varphi = 0°$ $\theta = 30°$	0.825	0.767
	$\theta = 90°$ $\varphi = 60°$	0.964	0.975	$\varphi = 0°$ $\theta = 60°$	0.948	0.964
	$\theta = 90°$ $\varphi = 90°$	0.925	0.928	$\varphi = 0°$ $\theta = 90°$	0.925	0.983
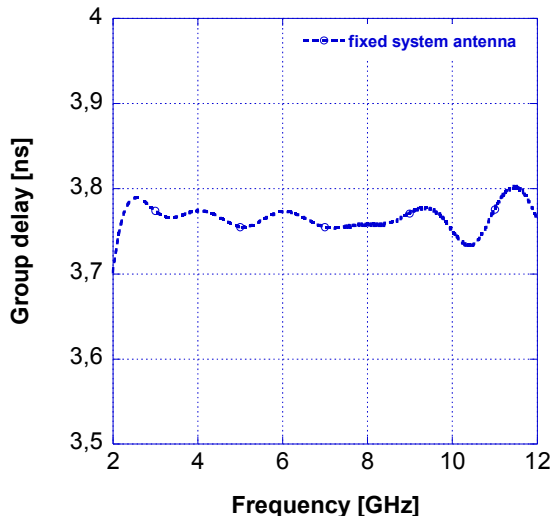
Fig. 6. Group delay of the proposed fixed system antenna.

Since the early time contents of this signal are dominated by the antenna and skin reflection, a calibration procedure has been implemented. The calibration signal has been calculated as the average value of all the measured voltages and has been subtracted from each received signal thus obtaining the calibrated signals. Figure 8 shows the calibrated signals corresponding to the minimum and maximum sphere radius, i.e. 2 cm and 2.5 cm respectively, simulating the end-systole and the end-diastole conditions.
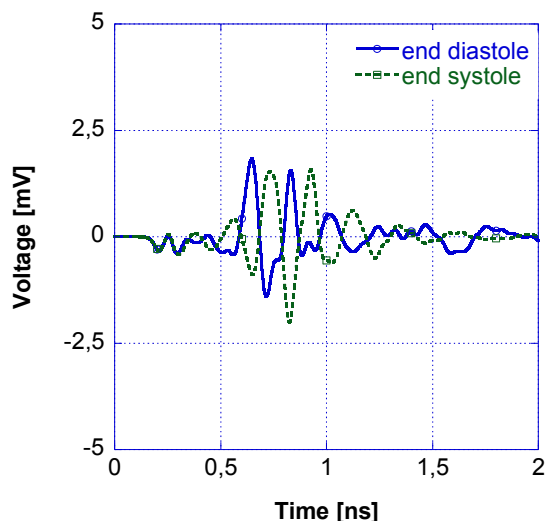
Fig. 8. Received signals for two cardiac phases.
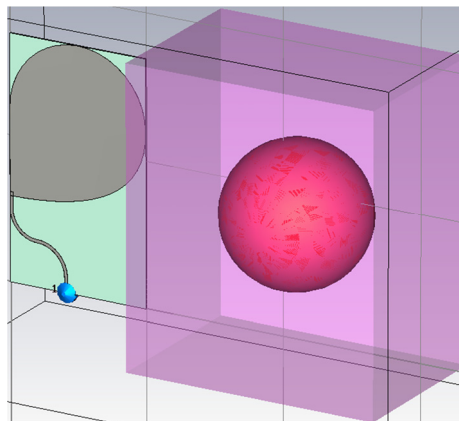
Fig. 7. Antenna in the presence of biological tissues.

The figure highlights that it is possible to distinguish between the two positions; in fact the corresponding signals arrive at the antenna feed point at different time instants (about 120 ps distance between the absolute minimum of the two signals) and, consequently, the heart movements can be detected through a suitable radar receiver.

IV. MEASUREMENT RESULTS

The two UWB antennas have been realized using a milling table and a SMA connector has been soldered at the input of the microstrip line. The photograph of the manufactured antennas including the coaxial connector is shown in Fig. 9.
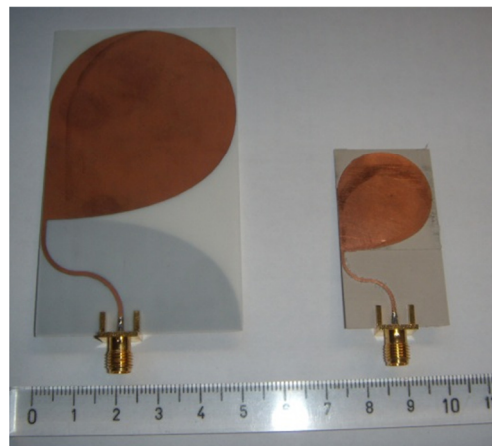
Fig. 9. Realized UWB antennas.

Return loss measurements were performed using a PNA E8363B network analyzer and placing the antenna in an anechoic chamber.

The measured return loss for the fixed antenna printed on RO4003 is reported in Fig. 10 indicating that the antenna features UWB behavior with a bandwidth from 3.1 GHz to more than 10.6 GHz assuming a -10 dB return loss reference. On the same figure, simulation results obtained adding the SMA connector to the antenna is also reported. A good agreement between numerical and experimental results is obtained. However, comparing Fig. 10 with Fig. 3 it can be noted that the presence of the connector makes the antenna return loss worse.

With reference to the wearable antenna, both simulations and measurements (not shown) have evidenced that, also in this case, the presence of the connector makes the return loss worse than the one obtained without the connector.

Since, in the final radar layout, the wearable antenna will be directly connected to a microstrip circuit, i.e. without a coaxial connector, the time domain reflectometry (TDR) technique has been used to remove, by means of the gating function, the connector effect from the measured data [21].

The obtained results are shown in Fig. 11, where the TDR measurements are compared with the simulations in the absence of the connector. The figure shows a good agreement between simulations and measurements especially in the 3.1 - 10.6 GHz frequency band.
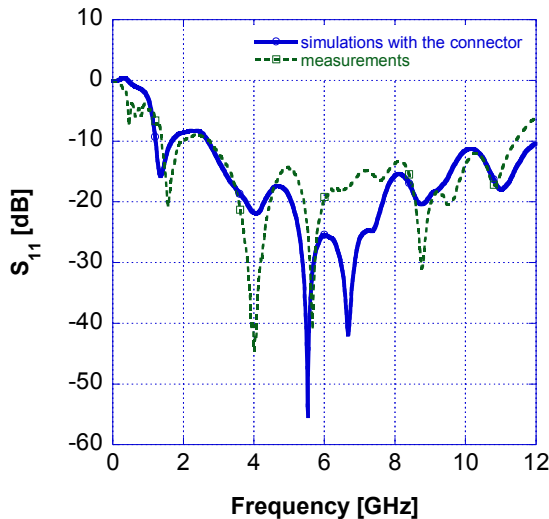
Fig. 10. Comparison between simulations and measurements for the fixed system antenna.
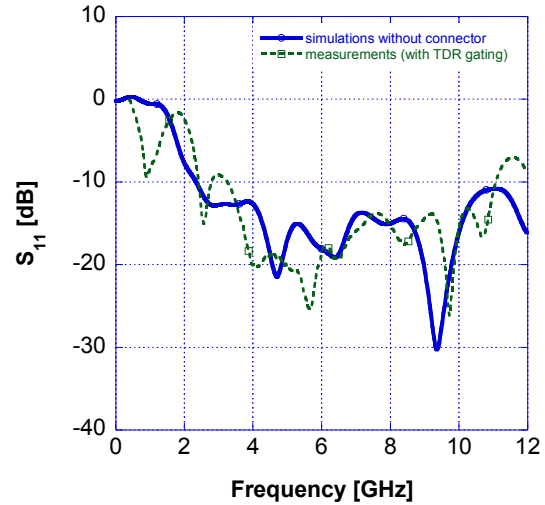
Fig. 11. Comparison between simulations and measurements for the wearable system antenna.

The fixed antenna has been further characterized by measuring the gain for a given direction ($\theta = 90°$, $\varphi = 0°$). This has been done by using the anechoic chamber available at ENEA-Casaccia research center and by using the gain transfer technique [22]. Figure 12 shows a comparison between measured and simulated values. Taking into account the measurement uncertainty of $\pm$ 2 dB the measurements are in good agreement with simulations.
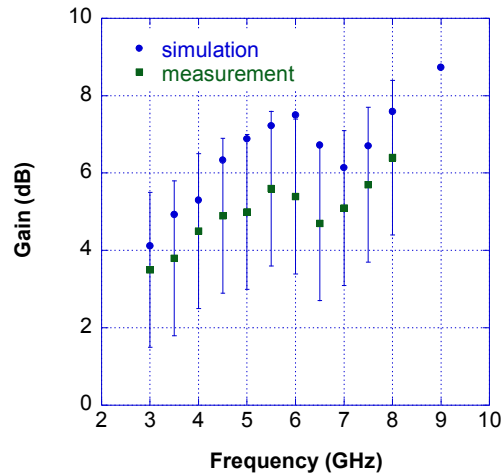
Fig. 12. Comparison between measured and simulated antenna gain.

Finally, by using the facilities available at ENEA Casaccia, the radiation pattern of the antenna has been measured at 4, 6, and 8 GHz.

Figure 13 shows a comparison between the measured and simulated radiation pattern on the x-y vertical plane at 6 GHz. Also in this case, a good agreement between measurements and simulations has been found.
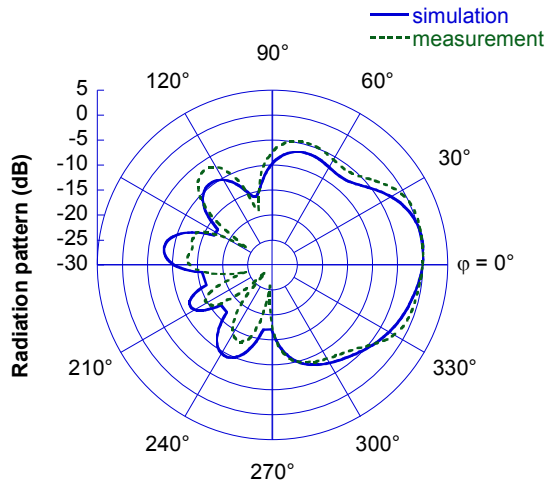
Fig. 13. Radiation pattern at 6 GHz.

V. CONCLUSION

The design of a fixed and a wearable planar UWB antenna usable in biomedical sensing of vital signs has been presented. Simulation results show that both antennas have a return loss better than -10 dB in the 3.1-10.6 GHz frequency band. Time domain performances of the fixed antenna have been investigated showing that it has a very good fidelity factor and an almost constant group delay. Moreover, it has been shown that with a suitable excitation of the wearable antenna it is possible to detect heart movements. Prototypes of the two antennas have been realized and return loss, gain, and radiation pattern have been measured, obtaining a good agreement between simulations and measurements.

VI. ACKNOWLEDGEMENTS

The authors wish to thank Dr. Paolo D'Atanasio and Mr. Alessandro Zambotti for their support during measurements carried out at ENEA-Casaccia.

REFERENCES

[1] E. M. Staderini, "UWB Radars in Medicine," *IEEE Aerospace and Electronic System Magazine*, vol. 17, no.1, pp. 13-18, Jan. 2002.

[2] S. Pisa, P. Bernardi, M. Cavagnaro, and E. Pittella, E. Piuzzi, "Monitoring of Cardio-Pulmonary Activity with UWB Radar: A Circuital Model," *Proc. Asia-Pacific Symp. on EMC & 19th Zurich Symp. on EMC.,* Singapore, pp. 224-227, May 2008.

[3] Federal Communications Commission, "New Public Safety Applications and Broadband Internet Access Among uses Envisioned by FCC Authorization of Ultra-Wideband Technology,"http://www.fcc.gov/Bureaus/Engineering_Technology/News_Releases/2000/nret0006.html, 2002.

[4] Federal Communications Commission, "45 CFR Part 15," http://www.fcc.gov/oet/info/rules, Revision of Part 15 of the Commission's Rules Regarding Ultra-Wideband Transmission, 2002.

[5] W. S. Chen and S. C. Wu "A Printed Heart Monopole Antenna with Band-Rejected Characteristics for IEEE 802.16a and UWB Applications," *Microwave Journal*, vol. 50, no. 5, pp.164, May 2007.

[6] A. M. Abbosh and M. E. Bialkowski, "Design of Ultrawideband Planar Monopole Antennas of Circular and Elliptical Shape," *IEEE Trans. Antennas Prop.*, vol. 56, no. 1, Jan. 2008.

[7] Y. Li et al., "A Novel Time-Domain UWB Antenna", *ICCS Singapore Int. Conf. on Comm. Systems,* pp. 793-796, Nov. 2008.

[8] S. Chamaani and S. A. Mirtaheri, "Planar UWB Monopole Antenna Optimization to Enhance Time-Domain Characteristics using PSO," *Int. J. Electron. Commun.*, AEU, 2008.

[9] H. Kanj and M. Popovic, "Two-Element T-Array for Cross-Polarized Breast Tumor Detection," *Applied Computational Electromagnetic Society (ACES) Journal*, vol. 23, no. 3, Sept. 2008.

[10] E. Gazit, "Improved Design of the Vivaldi Antenna," *IEE Proc., Part H*, vol. 135, no. 2, pp. 89–92, 1988.

[11] K. Yngvesson, T. Korzeniowski, Y. Kim, E. Kollberg, and J. Johansson, "The Tapered Slot Antenna - A New Integrated Element for Millimetre Wave Applications," *IEEE Microwave Theory Tech..*, vol. 37, no. 2, pp. 365–374, Feb. 1989.

[12] A. M. Abbosh, "Compact Antenna for Microwave Imaging Systems," *Proc. Biom. Eng. Conf. CIBEC'08,* 2008.

[13] CST Microwave Studio®, "Workflow and Solver Overview", CST Studio Suite™ 2008.

[14] D. Lamensdorf and L. Susma, "Baseband-Pulse-Antenna Techniques," *IEEE Ant. Prop. Magazine*, vol. 36, no. 1, February 1994.

[15] Z. N. Chen, X. H. Wu, H. F. Li, N. Yang, and Y. W. Chia, "Considerations for Source Pulses and Antennas in UWB Radio Systems," *IEEE Trans. Antennas Prop.*, vol. 52, no. 52, pp. 1739–1748, 2004.

[16] Q. Wu, R. Jin, J. Geng, and M. Ding, "Pulse Preserving Capabilities of Printed Circular Disk Monopole Antennas with Different Grounds for the Specified Input Signal Forms," *IEEE Trans. Antennas Prop.*, vol. 55, no. 10, Oct. 2007.

[17] Federal Communications Commission, "Evaluating Compliance with FCC Guidelines for Human Exposure to Radio Frequency Electromagnetic Fields," Supplement C to OET Bulletin 65 (Edition 97-01), Washington, DC 20554, 2001.

[18] K. S. Cole and R. H. Cole, "Dispersion and Absorption in Dielectrics. I. Alternating Current Characteristics," *J. Chem. Phys,* vol. 9, no. 4, pp. 341-51, 1941.

[19] S. Gabriel, R. W. Lau, and C. Gabriel: "The Dielectric Properties of Biological Tissues: III. Parametric Models for the Dielectric Spectrum of Tissues," *Phys. Med. Biol.,* vol. 41, pp. 2271–2293, 1996.

[20] http://niremf.ifac.cnr.it/docs/DIELECTRIC/AppendixC.html.

[21] H. Songoro, M. Vogel, and Z. Cendes, "Keeping Time with Maxwell's Equations," *IEEE Microwave Magazine,* vol. 11, pp. 42 – 49, April 2010.

[22] C. A. Balanis, "Antenna Theory: Analysis and Design," John Wiley & Sons, 2005.

Computer Simulations of Microwave Heating with Coupled Electromagnetic, Thermal, and Kinetic Phenomena

Malgorzata Celuch[1], Michal Soltysiak[2], and Ulrich Erle[3]

[1] Warsaw University of Technology
Institute of Radioelectronics, Nowowiejska 15/19, Warsaw, 00 − 665, Poland
M.Celuch@ire.pw.edu.pl

[2] QWED Sp. z o. o.
Krzywickiego 12 lok. 1, Warsaw, 02 − 078, Poland
m.soltysiak@qwed.com.pl

[3] Nestle R&D Centre Solon
5750 Harper Road, Solon, OH 44139, USA
Ulrich.Erle@rdsn.nestle.com

Abstract − A new functionality for the hybrid electromagnetic − thermodynamic simulations of microwave heating scenarios in the time domain is presented. The new functionality consists in the modelling of the heated load movement throughout the simulated process. Various types of the movement trajectories have been allowed for, including load rotation and load translation along user-defined piecewise-linear paths. Key aspects of this novel approach are addressed and justified from the computational electromagnetics perspective. Multiphysics simulation results are presented for a fictious and a commercially available microwave oven.

Index Terms − Coupled electromagnetic and thermal simulation, FDTD methods, hybrid modelling, microwave heating, multiphysics modelling,

I. INTRODUCTION

Over the last decade, electromagnetic simulation tools originally designed for telecommunication purposes have made their way into the microwave power industry. The fundamental relevance of those tools for microwave heating applications has been confirmed [1]. Moreover, the purely electromagnetic approach has been extended with other features adequate for the high-power processing, such as automatic variation of material parametres versus temperature [2] or bilateral coupling with the heat transfer equations [3].

A well known problem of microwave heating is spatial non-uniformity of final temperature patterns, which results from non-uniform modal electromagnetic field patterns characteristic for most applicators. In many low-cost domestic microwave ovens, one may observe so-called "hot spots", where the food is overcooked hence losing its nutritional and sensory qualities, as well as "cold spots", where the temperature of bacterial inactivation is not reached. A popular solution for fighting those problems and homogenising the temperature patterns consists in the movement of the heated objects during the microwave process. Examples include linear translation on conveyor belts in industrial tunnel ovens or rotation on the glass plate in household ovens.

In early works on computer simulations of microwave heating, e.g. [4], the effect of load rotation was studied at the post-processing stage. First, independent electromagnetic simulations were run for several angular positions of the load.
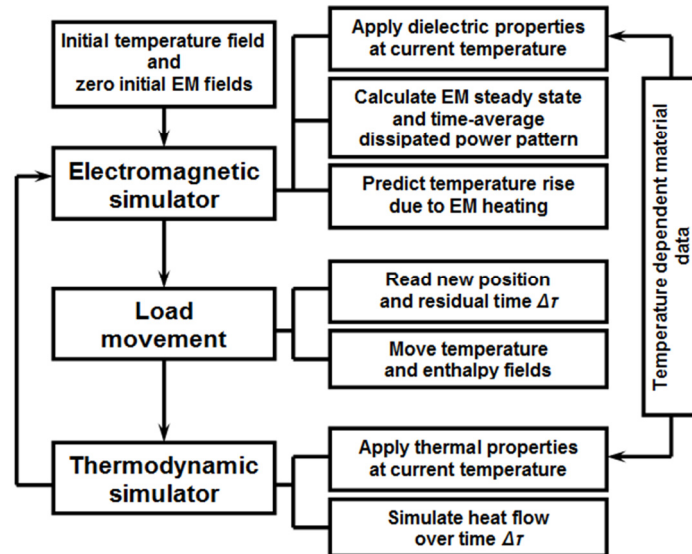
Fig. 1. Flow chart of coupled electromagnetic and thermal simulations with load movement.

Subsequently, the dissipated power patterns for those positions were superimposed and averaged. On their basis, the final temperature was approximated. Such an approach is rigorous if the load parametres remain constant; it provides a physically consistent approximation if the load parametres vary slowly with temperature. However, dielectric and thermal parametres of typical foods are strongly temperature dependent and undergo drastic changes around phase change points. For example, relative permittivity and electric conductivity of beef change from 4.9 and 0.064 S/m, respectively, in the frozen state, to 48.2 and 2.194 S/m at the room temperature. The post-processing approach to the load movement misses the non-linear effects due to the material changes and may end up with physically inconsistent results.

In a recent work [5], the effect of load rotation has been embedded into the electromagnetic-thermal simulation loop. Material parametres are automatically updated at each consecutive position, as a function of the current temperature pattern. This facilitates accurate prediction of the final temperature, even for strongly non-linear problems.

In this work, we extend the methodology of [5] to arbitrary movements of the load. Specifically, the load is translated along piecewise-linear trajectories. For full flexibility, consecutive positions along the trajectory as well as residual times at each position are defined by the user in external text-files. At the conceptual level, the algorithm has been presented at the recent ACES Symposium [6].

In further extension to [5] and [6], which focus on predicting temperature patterns in domestic oven scenarios, our focus herein is on the computational electromagnetics aspects. In particular, we show how a continuous non-linear process is approximated with a discrete parametric one. We also demonstrate a speed-up of the electromagnetic calculations part achieved by resuming those calculations from the previous steady state, rather than the initial conditions. The elaborated algorithms are implemented in the finite-difference time-domain (FDTD) electromagnetic software environment of [7].

Due to the lack of household ovens enabling translation of the object along an arbitrary trajectory, those studies are limited to numerical investigations without further comparison with real measurements.

II. FDTD ALGORITHM OF COUPLED ELECTROMAGNETIC AND THERMAL SIMULATIONS WITH LOAD MOVEMENT

Figure 1 shows the flow chart of the hybrid algorithm, which bilaterally couples the electromagnetic and thermodynamic computations. Strictly speaking, the electromagnetic process is non-linear, as the media

parametres continuously change in response to the dissipated power and increasing temperature. However, we can parameterise the problem taking advantage of the different time-scales characteristic for the electromagnetic and thermal phenomena.

Imagine we wish to raise temperature of the heated beef load by a small but observable amount, e.g. 5 °C. According to Table 1, this requires delivering approximately 15 kJ/kg at the frozen stage (-20°C to -15°C) or approximately 24 kJ/kg at the thawed stage (50°C to 55°C). For a typical load that weighs, for example, 500 g, we would need to deliver about 8-12 kJ. Since domestic ovens operate at below 1 kW, this entails at least 8-12 s of processing.

Industrial installations operate at a few hundred kilowatts but their loads are proportionally bigger, tens or hundreds of kilograms. Thus in any case, significant changes of thermally-dependent material parametres occur in a matter of seconds or tens of seconds. Heat flow effects proceed on a similar time scale.

On the other hand, the operating frequency of domestic ovens is 2.45 GHz, while industrial appliances work at 2.45 GHz or 915 MHz. This corresponds to the period of 0.4 ns or 1.1 ns, respectively, and the EM FDTD analysis proceeds with the time step not exceeding 50 ps. In view of the above contrast in the time scales, there is no need to solve a non-linear problem at each FDTD time-step. Instead, the continuous problem can be discretised into a sequence of discrete heating steps. We shall use the symbol $\Delta\tau$ to denote the duration of each such heating time step, $\Delta\tau$ being of the order of seconds.

Each heating step starts with the EM FDTD analysis, with load parametres adjusted to the previously reached temperature patterns - hence spatially inhomogeneous but constant in time during this EM analysis. It is important to stress that each consecutive EM analysis starts from the previous EM steady state, and not from the initial conditions of zero EM fields. As computational experiments show, such an approach allows reducing the number of FDTD iterations needed to reach a new steady state by at least a factor of 10. Since the EM FDTD analysis is the most time-consuming part of the developed hybrid system, overall efficiency is also improved by nearly a factor of 10.

When the EM steady state is reached, the time-averaged value of power dissipated within each FDTD cell over the volume of the heated object is calculated. Temperature rise is then predicted under the assumption that the heating is purely electromagnetic (with no heat flow effects) and proceeds with the constant dissipated power pattern for the $\Delta\tau$ duration. The enthalpy density is thus updated by the following predictor equation:

$$H_p^{n+1}(x,y,z) = H^n(x,y,z) + \frac{P^{n+1}(x,y,z)\cdot\Delta\tau}{\Delta V(x,y,z)} \quad , \qquad (1)$$

where H^n is enthalpy density in J/m³ at the previous heating time step, H_p^{n+1} - predicted enthalpy density at the current step, P^{n+1} - time-averaged dissipated power in each cell in W, ΔV - volume of the cell in m³, and $\Delta\tau$ in s. A new temperature pattern T_p^{n+1} is now also predicted, based on the enthalpy pattern and the material parametre files provided by the user for each temperature-dependent medium (see Table 1).

The new geometry due to the load movement is then read. It is assumed that the temperature and enthalpy patterns follow the load, while the electromagnetic field patterns remain bound to the cavity. This assumption is physically viable since enthalpy is bound to materials. On the other hand, microwave power applicators are designed so as to work with various types of loads. This requires that their modal patterns be cavity-controlled, with load-focussing effects suppressed as much as possible.

Now heat diffusion effects are considered. The enthalpy H and temperature T patterns are corrected by solving the heat transfer equation:

$$\frac{\partial H(x,y,z)}{\partial t} = \nabla\left(k(T)\nabla T\right) \quad , \qquad (2)$$

where k is thermal conductivity expressed in W/(m°C). The dependence between temperature and enthalpy can be non-linear and it is read from the material parametre files (see Table 1). The initial conditions for eq.(2) are H_p^{n+1} and T_p^{n+1} predicted by eq.(1). The diffusion time is $\Delta\tau$. The solution is accomplished by the thermal FDTD algorithm operating on the same mesh as the EM FDTD algorithm. Such an approach avoids numerical diffusion errors, which occur if additional interpolations between the EM and thermal meshes are required [8]. The results of solving eq.(2) are the corrected enthalpy H^{n+1} and

temperature T^{n+1} patterns, fed back to the EM solver.

Before the EM FDTD algorithm proceeds to calculate the next EM steady state, it updates the dielectric properties of the heated load (or more precisely, of each FDTD cell within the load) based on the temperature-dependent characteristics provided in the material files (see Table 1). At this point, a numerical challenge arises. Since the material parametres change between the two EM analyses, care must be taken not to induce numerical parasites violating the Gauss law. It has been shown [9] that such modes with non-zero divergence can exist on the FDTD mesh and remain static. They do not interact with the propagating microwave solutions but they would contaminate the calculated power envelopes and thus the predicted temperature. The procedure proposed in [10] and based on the *E, H* to *D, B* conversion is therefore adapted to our coupled system before each media parametres update, in order to suppress such numerical artifacts.

III. NUMERICAL MODELS OF THE INVESTIGATED CASES

Two test cases are considered: one based on a fictious oven cavity and the other being a numerical replica of the Whirlpool Max oven available on the market.

The first cavity (upper in Fig. 2) is 267 mm in width (*x*-direction in Fig. 2), 270 mm in length (*y*-direction in Fig. 2), and 188 mm in height (*z*-direction in Fig. 2). The feeding waveguide of 78 mm in width (*y*-direction in Fig. 2), 18 mm in height (*x*-direction in Fig. 2), and 80 mm in length (*z*-direction in Fig. 2) launches the fundamental TE01 waveguide mode, at the ISM frequency of 2.45 GHz.

The plate of 227 mm diametre and 6 mm height is located centrally in the cavity, 15 mm above its floor. The material of the plate is lossless and its relative permittivity is equal to 6. The waveguide is excited by the magnetron of 650 W time-averaged available power.

The other oven is shown in the lower part of Fig. 2. The main cavity is semi-cylindrical in shape. Its sophisticated feeding system including two apertures separated by a septum is modelled in detail.
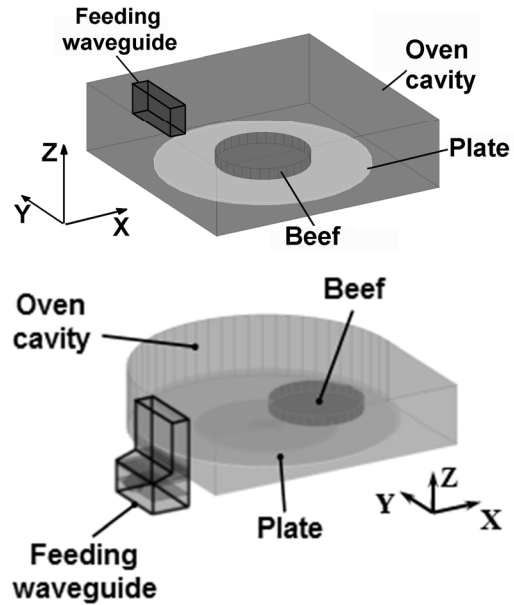
Fig. 2. Numerical model of the investigated microwave ovens: upper – the fictious oven, lower – Whirlpool Max.

The heated object of a cylindrical shape, 100 mm diametre and 30 mm height possesses electromagnetic and thermal properties of beef. Those properties are listed in Table 1 as a function of temperature. The values of enthalpy density (column 2) are taken from [11]. The dielectric properties (columns 3 and 4) are based on measurements published in [12]. Heat conductivity (column 5) is based on the measurements performed by the authors for raw beef at room temperature. Adiabatic boundary conditions (zero heat flux) are set at the boundaries between the heated element and air as well as the heated element and the plate.

Within this work we do not consider the influence of convection and radiation on temperature of the heated object. However, as shown in [13], the amount of emitted heat is proportional to the fourth power of temperature and thus it has a strong impact on thermal behaviour of the object only when heated to very high temperatures.

IV. RESULTS OF MULTIPHYSICS COMPUTATIONS

Three cases regarding the object's kinetics during its electromagnetic heating are considered: rotation of the plate is blocked and the object

remains static at the centre of the plate (Fig. 3), the plate rotates at 5 r.p.m and the object moves along a circular trajectory of 120 mm diametre (Fig. 4), the object moves along a piecewise linear trajectory (Fig. 5).

Table 1: Dielectric and thermal properties of beef

Temperature	Enthalpy density [11]	Relative permittivity [12]	Electric conductivity [12]	Heat conductivity
°C	J/kg	(-)	(S/m)	W/(m°C)
-20	0.0	4.9	0.064	0.69
-15	14840.0	5.5	0.093	0.69
-10	36464.0	6.1	0.153	0.69
-5	75684.0	12.3	0.573	0.69
-3	117024.0	22.0	1.118	0.69
-2.2	153064.0	30.0	1.636	0.69
-1.6	203944.0	42.0	2.113	0.69
-1.3	254824.0	46.0	2.385	0.69
-1.1	290864.0	48.9	2.426	0.69
-1	305704.0	49.2	2.440	0.69
10	347574.0	48.9	2.317	0.69
20	405874.0	48.2	2.194	0.69
35	477424.0	46.9	2.072	0.69
50	548974.0	45.5	1.949	0.69
65	620524.0	43.6	1.922	0.69
80	692074.0	41.7	1.908	0.69
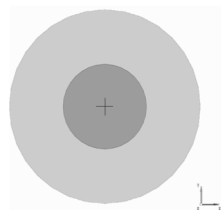
Fig. 3. Static object located at the centre of the plate.
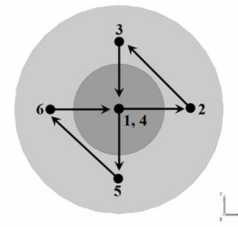
Fig. 5. Object moving along a piecewise-linear trajectory.
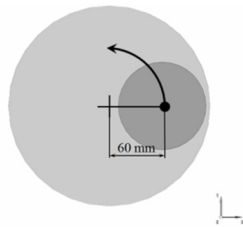
Fig. 4. Object located off-centre, rotating with constant speed.

The total heating time for each of the cases is set to 180 sec. In the case with rotation (Fig. 4), the continuous motion of the object is approximated by a set of 9 angular positions, with 40 degree step. In the case with the piecewise linear trajectory (Fig. 5), the heating sub-time at each position is 5 sec. and the trip along the trajectory is repeated until the total heating time is reached.
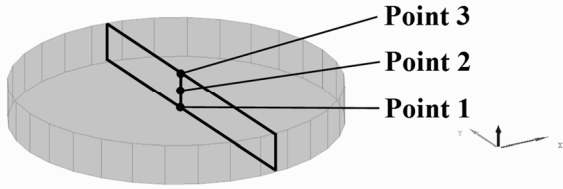
Fig. 6. Positions of the points inside beef whereat temperature is recorded over time.

Figure 7 shows evolution of temperature over time at the centre of the load (Point 2 in Fig. 6) in the fictious oven. Results for other points have been reported in [6]. Changes of the object's trajectory significantly influence the temperature
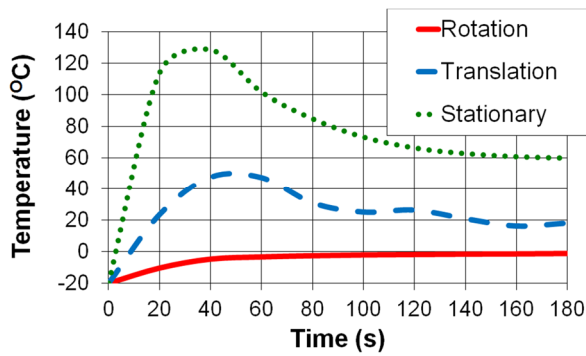
Fig. 7. Evolution of temperature over time for Point 2.

at Point 2. When the load is static, maximum temperature at Point 2 is reached after 40 s. This maximum temperature is equal 128.5 ^{o}C and subsequently decreases due to heat diffusion.
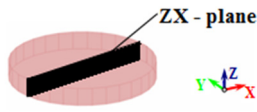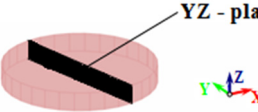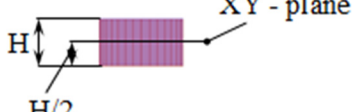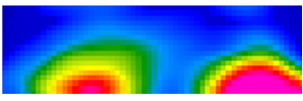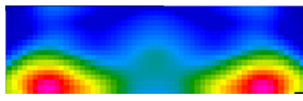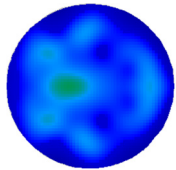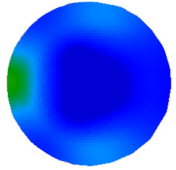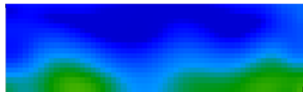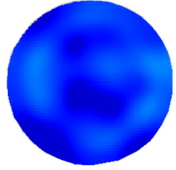
When the object moves along the piecewise-linear trajectory, the maximum temperature at Point 2 is substantially lower (47.6 ^{o}C) and occurs later in time. When the object moves along the circular trajectory, the temperature at Point 2 increases very slowly and hardly exceeds 0 ^{o}C over the simulated 180 sec heating time.

Table 3 shows the final temperature patterns for the three investigated cases in the fictious oven. The patterns were taken across the 2D cuts defined in the first row of Table 3. As expected, the highest non-uniformity of the final temperature across the load results from the heating of the static object. This is because the heat transfer capabilities of beef are too weak to compensate for the inherent non-uniformity of the microwave dissipated power patterns in the considered scenario. The non-uniformities decrease when the object rotates in the cavity, as it is the case in most domestic ovens on the European market. However, the central cold spot and edge overheating effects along the object circumference cannot be compensated by the rotation.

Table 2: Temperature patterns across the *xy*, *zx*, *yz* planes after 180 sec of heating in Whirlpool Max

Table 3: Temperature patterns across the *xy*, *zx*, *yz* planes after 180 sec of heating in the fictious oven

The most uniform final temperature pattern is produced when the object moves along the piecewise-linear trajectory. Simulations in the other oven (Table 2) also support this claim. While the rotating load suffers from the edge overheating, the translation leads to more uniform radial temperature distribution.

The translation trajectory in this experiment has been proposed *ad hoc* for the purpose of demonstrating the new computational feature and it does not necessarily give the best possible performance. However, the results confirm that introducing load movements other than rotation is a promising way towards designing new microwave cavities with enhanced heating uniformity.

V. CONCLUSIONS

The coupled electromagnetic-thermodynamic simulations toolkit based on the concepts summarized in [1-5] and implemented in [7] has been extended with new capabilities pertaining to different load kinetics during the heating process. In particular, load movement along piecewise-linear trajectories has been facilitated. For maximum flexibility, the trajectory as well as the speed of load movement along each segment are defined by the user in text files. Specific numerical challenges related to the parameterisation of the non-linear electromagnetic problem, suppressing numerical parasitic modes in the parameterised EM FDTD algorithm, and accelerating the overall analysis have been addressed.

Computational experiments with the *ad hoc* constructed piecewise-linear trajectory show its superiority in terms of the final temperature patterns. The resulting electromagnetic-thermodynamic-kinetic simulation methodology becomes a convenient tool for the design of new microwave heating appliances.

REFERENCES

[1] M. Celuch and W. K. Gwarek, "Properties of the FDTD Method Relevant to the Analysis of Microwave Power Problems," *J. Microwave Power and Electromagnetic Energy*, vol. 41, no.4, pp. 62-80, 2007.

[2] M. Celuch-Marcysiak, W. K. Gwarek, and M. Sypniewski, "A Novel FDTD System for Microwave Heating and Thawing Analysis with Automatic Time-Variation of Enthalpy-Dependent Media Parameters," in *Advances in Microwave and Radio-Frequency Processing*, Springer Verlag, pp. 199-209, 2006.

[3] P. Kopyt and M. Celuch, "Coupled Electromagnetic-Thermodynamic Simulations of Microwave Heating Problems using the FDTD Algorithm," *J. Microwave Power and Electromagnetic Energy*, vol. 41, no. 4, pp. 18-29, 2007.

[4] P. Kopyt, M. Celuch-Marcysiak, and W. K. Gwarek, "FDTD Modelling of Electromagnetic Power Dissipation in Rotated Objects," *3rd World Congress on Microwave & Radio Frequency Applications*, Sydney, Australia, session T2C, Sept. 2002.

[5] M. Celuch and P. Kopyt, "Modeling Microwave Heating in Foods, " in: *Development of packaging and products for use in microwave ovens*, ed. M. W. Lorence and P. S. Pesheck, Woodhead Publishing Limited and CRC Press LLC, pp. 305-348, Aug. 2009.

[6] M. Celuch, M. Soltysiak, and U. Erle, "Coupled Electromagnetic - Thermodynamic Simulations Including Load Movement," *The 26th Annual Review of Progress in Computational Electromagnetics ACES-2010*, Tampere, Finland, pp.410-415, April 2010.

[7] QuickWave-3D (1997-2010), QWED Sp. z o.o., http://www.qwed.eu.

[8] P. Kopyt and M. Celuch, "Coupled FDTD - FEM Approach to Modelling of Microwave Heating Process," *Fifth IEE Intl. Conf. on Computation in Electromagnetics CEM 2004, Stratford-upon-Avon*, UK, pp.171-172, April 2004.

[9] M. Celuch-Marcysiak and W.K.Gwarek, "On the Nature of Solutions Produced by Finite Difference Schemes in Time Domain," *Intl. Journal of Numerical Modelling – Electronic Networks, Devices and Fields*, vol. 12, no. 1/2, pp. 23-40, Jan.-Apr. 1999.

[10] M.Celuch-Marcysiak, "Extended Theory of FDTD S- and P-eigenmodes in Lossy Media and its Application to the Analysis of Coupled Problems," *IEEE MTT-S Intl. Microwave Symp. Dig*, Fort Worth, pp.1713-1716, June 2004.

[11] A. M. Tocci and R. H. Mascheroni, "Characteristics of Differential Scanning Calorimetry Determination of Thermophysical Properties of Meats," *Lebensmittel-Wissenschaft und –Technologie*, vol. 31, no. 5, pp. 418-426, 1998.

[12] T. Ohlsson, N. E. Bengtsson, and P. O. Risman, "The Frequency and Temperature Dependence of Dielectric Food Data as Determined by a Cavity Perturbation Technique," *J. Microwave Power and Electromagnetic Energy*, vol. 9, pp. 129-145, 1974.

[13] J. Haala, J. V. Hagen, W. Wiesbeck, Fast Implementation of Heat Radiation in a Self-Consistent FDTD Analysis Tool for Microwave and Hybrid Ovens," *Applied Computational Electromagnetic Society (ACES) Journal*, vol. 16, no. 1, pp. 11-19, Mar. 2001.

Malgorzata Celuch received the International Baccalaureate (honours) at the United World College of the Atlantic, UK. She then graduated from the Warsaw University of Technology, receiving M.Sc. (honours) and Ph.D. (honours) in 1988 and 1996, respectively. Since 1996 she has been Assistant Professor at the Warsaw University of Technology (www.ire.pw.edu.pl). Her main fields of research are electromagnetic modelling of microwave circuits and numerical methods for computational electromagnetics, including conformal FDTD methods, new applications of FDTD with enthalpy-dependent material parametres, and frequency-domain parametre extraction from FDTD simulations.

Dr. Celuch is author of over 120 publications including 18 journal papers (6 in the IEEE series). Malgorzata Celuch is co-author of QuickWave software, co-founder and vice-president of QWED

(www.qwed.eu). QWED team is recipient of many prestigious awards including the Prime Minister of Poland Award and the European Information Technology Prize. Dr. Celuch has also received personal awards from the Minister of Education, Rector, the Foundation for Polish Science as well as the Highest Quality Workshop Award at IEEE IMS 2009.

Michal Soltysiak received the M.Sc. degree from the Czestochowa University of Technology in 2002. He is a Ph.D. student at the Warsaw University of Technology, Institute of Radioelectronics.

His research activity deals with coupled electromagnetic and thermal simulations of microwave heating and measurements of dielectric properties of food products at microwave frequencies.

He is employed in QWED Company, the vendor of QuickWave software for electromagnetic design.

Urlich Erle received his Master Degree in Industrial Engineering 1994 and his Ph.D. (honours) in Process Engineering 2000 from Karlsruhe Technical University. His work was in the area of microwave applications in food processing, especially microwave vacuum drying. After an assignment as project engineer at Merck (Darmstadt/Germany) he joined the Nestlé Product Technology Centre in Kemptthal/Switzerland in 2001. After several projects in the field of dehydrated food, comprising six years at Nestlé Product Technology Centre Singen/Germany, he was transferred to Nestlé R&D Center Solon/Ohio/USA, where he currently holds the position of a Senior Scientific Advisor.

Ultra High-Resolution FDTD Modeling of a High-Performance VLSI Package for Identifying Resonances and Coupling

César Méndez Ruiz and Jamesina J. Simpson

Electrical and Computer Engineering Department
University of New Mexico, Albuquerque, NM, 87106, USA
cmendezr@unm.edu, simpson@ece.unm.edu

Abstract ─ It is becoming increasingly important to computationally predict, study, and prevent electromagnetic compatibility (EMC) issues arising within and between ICs and other components comprising portable electronic devices. Here, we conduct a phenomenological study involving an ultra high-resolution, three-dimensional finite-difference time-domain (FDTD) model of a sample IC package having over one billion grid cells. Specifically, we determine the resonances and coupling patterns arising within the highly complex IC package. The frequency range of interest extends from 100 MHz to 7 GHz. Results indicate that the arrangement and geometry of the separate power, ground, and signaling networks comprising the IC package greatly influences the electromagnetic behavior within different regions of the package.

Index Terms ─ Digital electronics, EM compatibility, EM coupling, FDTD, resonance, very-large-scale integration.

I. INTRODUCTION

Unintended electromagnetic interference occurring within an integrated circuit (IC) package or via external coupling is a large concern in the design of ICs as well as for the operation of portable electronic devices. ICs are continually being designed to operate at higher clock speeds, be powered with lower supply voltages, and be integrated at higher densities. Further, many modern platforms such as notebooks and ultra mobile devices are continually increasing in functionality while also becoming more compact in size. As a result, ICs must be positioned closer and closer in proximity to other ICs as well as to a variety of high performance wireless communication systems such as Wi-Fi, VoIP, WiMAX, and Bluetooth [1-3], in addition to near field communication technology. All of these trends are causing electromagnetic compatibility (EMC) issues to greatly influence the reliability and operation of electronic devices. As a result, as the technology progresses, EMC must be at the core of the design process of these devices and their components. This is particularly true for ICs, since they tend to be the most susceptible component of the system due to risks of over-voltage or over-current.

Initial EMC research focused on ICs can be traced back to 1965. The effects of EM fields from nuclear explosions on electronic devices were studied at the Special Weapons Center based at Kirtland Air Force Base, Albuquerque, New Mexico, USA. The simulation software SCEPTRE [4] was developed by IBM as a result of this pioneering work. Since this initial research, there have been additional efforts to study the EMC performance of ICs. However, most of the research has been focused on the external region of the packaging. Further, an example analysis of ICs has relied on a complicated integration of measurements, simulations, and analytical calculations through the use of macromodels [5]. In fact, as recently as 2005, the authors of [5] state that for studying ICs, "the combination of propagation effects with possibly very complex geometry… makes a direct full-wave approach not feasible."

More recently, an unconditionally stable time-domain technique using Laguerre polynomials is employed in [6] to develop a methodology for

chip-package cosimulation of ICs. In that work, the IC is divided into sub-blocks (the signal delivery and power delivery networks) for analysis using a full-wave Laguerre equivalent circuit procedure before integrating the results together.

In the present work, we instead take advantage of the computational power afforded by today's supercomputers and simulate on a grand scale a complete IC package as well as the underlying printed circuit board (PCB). Specifically, we solve the full Maxwell's equations using an ultra high-resolution, three-dimensional (3-D) finite-difference time-domain (FDTD) [7, 8] model having over 1 billion grid cells and simultaneously accounting for the power, signal, and ground networks (which we will term functional layers) of the IC package. All of our models are original and do not involve any commercial software.

The simulations and results provided in this paper are directed towards obtaining resonance and coupling patterns throughout the IC package under varying excitation scenarios. Utilizing 384 processors, each of the excitation scenarios for this detailed model takes 26 hours to run. The frequency range of interest extends from 100 MHz to 7 GHz.

This phenomenological study represents a major advance towards enabling engineers to obtain a comprehensive understanding of the fundamental physics behind EMC issues within ICs, and towards providing design parameters necessary for improving and optimizing IC package layouts.

Previously, two related conference abstracts [9, 10] briefly described the general modeling approach employed for this study. A brief description of the sample IC package as well as one example snapshot of electromagnetic energy propagating within one layer of the package was then provided in [11]. This paper, however, significantly builds off of the work of [9-11] by providing a detailed analysis of the electromagnetic behavior, particularly resonances and coupling, within different regions of the IC package and for varying excitations of the IC package. The detailed model descriptions as well as all of the result figures and analyses are original to this paper.

State of the art IC EMC laboratory test techniques are based on measuring either the emissions from the IC (TEM cells, pin current measurements, and near-magnetic field scans) or the susceptibility to electromagnetic noise (bulk current injection, direct power injection, and field coupled) [12]. The common characteristic in all these methods is that the instrumentation is located external to the IC and therefore are not suitable for direct comparisons against the results presented in this paper that concern the inside of the package.

The analysis provided in this paper is unique because the geometry of the layers of the IC package does not behave in an analytically predictable nature. For example, the periodic vias comprising each layer are not all connected to the same adjacent conducting planes (layers); the vias are instead each assigned to one of the three different functional layers (signal, ground, power) and as such many of them must extend through some conducting layers of a different functional type without forming an actual connection. As a result, the vias within the different regions of the package do not behave in a manner according to typical electromagnetic bandgap structures or substrate integrated waveguides as in [13].

The remainder of this paper is organized as follows. Section II below demonstrates the validity of the code by duplicating results of similar structures reported by other authors. Section III below provides an overview of the FDTD model. Section IV describes the general methodology of the analysis and the simulation cases that are considered. The corresponding simulation results are then documented and discussed in Section V. Finally, section VI concludes the paper.

II. CODE VALIDATION

In order to validate the code that is used for the modeling of the IC package we first successfully reproduce results obtained for a similar, but much simpler structure as reported by Shahparnia et al. [14, 15]. In these references, the authors developed an analytical model to predict the resonant properties, pass-band, and stop-band of electromagnetic bandgap (EBG) structures embedded in PCBs and packages. They compare their results against finite element (FE) based results. The frequency range of interest, gap between conducting planes and via diameter are comparable to those corresponding to the IC package analyzed in this paper. A lateral view of the considered 3-D structure is shown in Fig 1.

Table 1: Comparison of FDTD model calculations and results reported in [14]

d (mm)	a (mm)	h_1 (mm)	h_2 (mm)	ε_{r1}	ε_{r2}	Vias diameter (μm)	FE Gap (GHz)	Model Gap (GHz)	FDTD Gap (GHz)
10.4	10×10	1.54	1.54	4.1	4.1	800	2.1-4.0	2.5-4.0	2.0-3.9
10.4	10×10	1.54	1.54	8.2	4.1	800	1.6-3.7	1.8-3.7	1.7-4.0
10.4	10×10	1.54	1.54	12.3	4.1	800	1.3-3.1	1.5-3.5	1.4-3.6
10.4	10×10	1.54	1.54	16.4	4.1	800	1.2-2.9	1.3-3.4	1.3-3.3
2.2	2×2	0.016	0.1	4.1	4.1	125	6.0-18.1	6.1-14.7	7.2-19.5
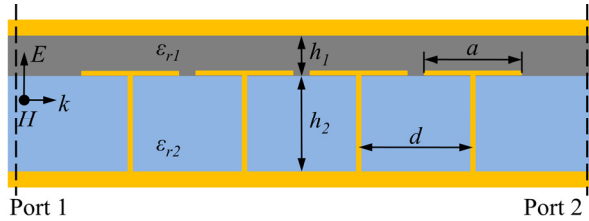
Fig. 1. EBG structure embedded in a PCB. Four infinitely long rows of EBG cells are placed between the 2 ports that are used to calculate the S parameters.

Table 1 collects the band-stop frequency range of various EBG structures. The limits of the gap are determined by a -20 dB criteria of the scattering parameter S_{21}. For all considered cases, the FDTD model shows satisfactory agreement, in particular with the results obtained from the FE simulations.

III. FDTD MODEL OF SAMPLE IC PACKAGE AND PCB
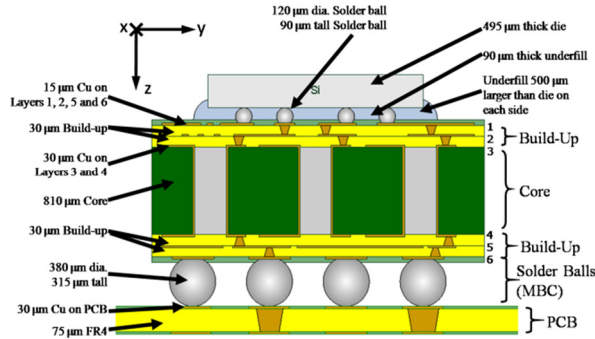
Fig. 2. General cross-sectional view of the sample six-layer IC package with the underlying sample PCB.

The FDTD model employed in this study encompasses 2580×2580×160 grid cells in each x, y, and z Cartesian direction to finely model the sample IC package and the underlying sample PCB. A general schematic of the model is shown in Fig. 2. The complete FDTD model includes details of the conducting layers, silicon,

dielectrics, vias, ground / power traces, and solder balls. For a practical implementation of such demanding computation and storage it becomes necessary to exploit the parallel processing techniques. Specifically, we employ the domain decomposition parallelism scheme in which the computation domain is divided into equal rectangular sub-areas. The essential elements of a parallel algorithm for the FDTD method using the message passing interface (MPI) library are reported in [16].

Figures 3, 5, and 6 are designed with a specific color code to identify materials and functional layers. The white color was defined to represent air, red corresponds to any dielectric, yellow corresponds to ground, green corresponds to power and blue corresponds to signal.

There are in total six conducting layers in the IC package. Conducting layers 2, 4, and 6 are ground planes while conducting layers 3 and 5 belong to the power network. Conducting layer 1 is split into two conducting surfaces of equal area as shown in Fig. 3: the left side is ground and the right is power. The via pitch under the die shadow is denser than outside the die shadow (320 μm vs. 1 mm). The PCB is comprised of two conducting planes; one is power and the other is ground.

Each via within the structure is assigned to the signal, ground, or power function layer. Each via is thus only connected to its corresponding signal / ground / power conducting layer, respectively. That is, the ground and power vias are shorted at each end only to ground and power conducting layers, respectively, and the signal vias are connected to ground conducting layers through lumped resistors. As a result, because the ground, signal, and power conducting layers alternate through the structure, the vias must extend through an opening through some conducting planes to connect to a conducting plane further away. This geometry greatly complicates the electromagnetic behavior throughout the entire IC package.

The FDTD grid has a uniform cell size of $10 \times 10 \times 15$ μm in x, y, and z-directions, respectively. This resolution is high enough to resolve the smallest circular via diameter within the model without introducing stair-casing effects into the computational results.
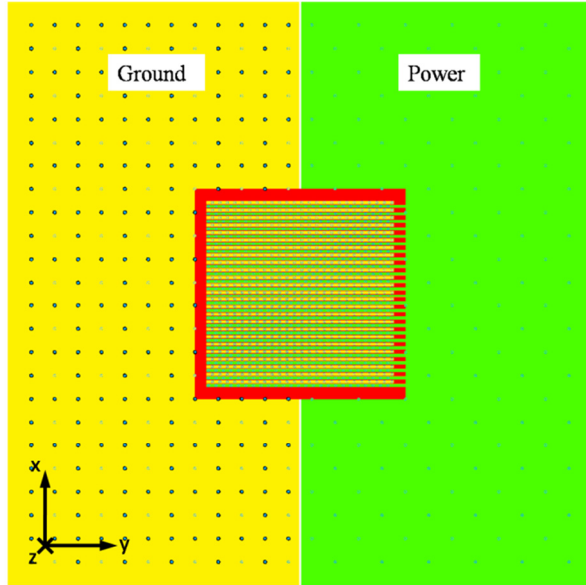
Fig. 3. Detailed top view of the IC package conducting layer 1 of Fig. 1. The circles represent the via/via pad/via anti-pad locations.

Table 2 lists all materials within the model and their corresponding electrical properties. The conductivities are calculated assuming a clock frequency of 1 GHz.

Table 2: Materials properties

Material	Relative Permittivity (ε_r)	Loss Tan	Conductivity (S/m)
Silicon	10.24	0.025	0.01420
Underfill	3.5	0.025	0.00487
Build-Up	3.7	0.017	0.00350
Core	4.6	0.017	0.00435
FR4	4.3	0.017	0.00407

IV. METHODOLOGY AND SIMULATION CASES

A total of six simulation cases are conducted to characterize the resonances and coupling within the package. In all cases, the source is a modulated Gaussian pulse centered at 8 GHz and having spectral energy from 100 MHz to 20 GHz. We primarily consider the frequency range of 100 MHz to 7 GHz, but in a few cases we examine the
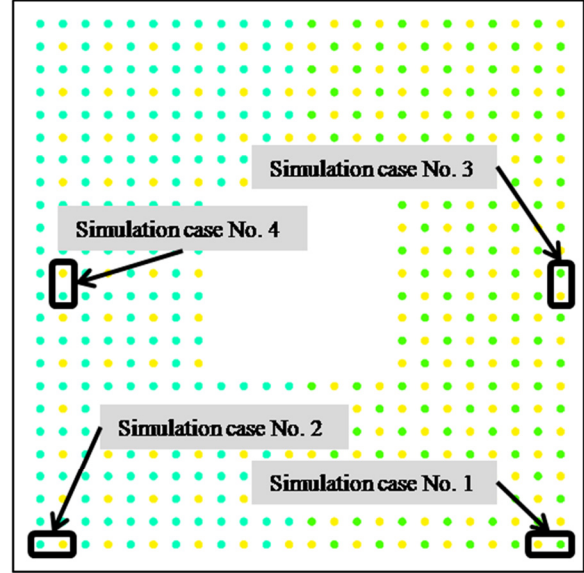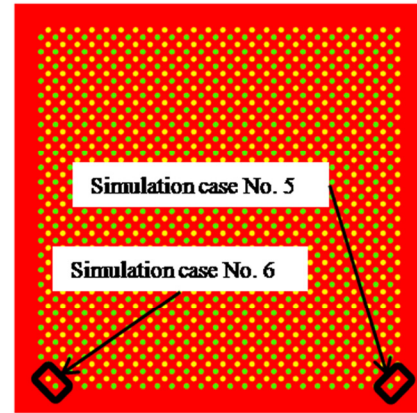
Fig. 4. Sources locations for the different simulation cases. (a) Motherboard connection solder balls. (b) Solder balls in the under-fill region, a zoomed-in view to the under-die zone.

performance of the IC up to 20 GHz for additional behavioral information.

For each simulation case, two neighboring solder balls are excited with the source waveform skewed at 50%. The excitation is implemented as a set of lumped resistive voltage sources [17] along the surface of both solder balls so that the total resistance of each lumped resistive source is 50 ohms. The unique feature of each simulation case is the location of these sourced pair of solder balls. Figure 4(a) shows the source locations for simulation cases 1 – 4 having the excitation implemented at two motherboard connection
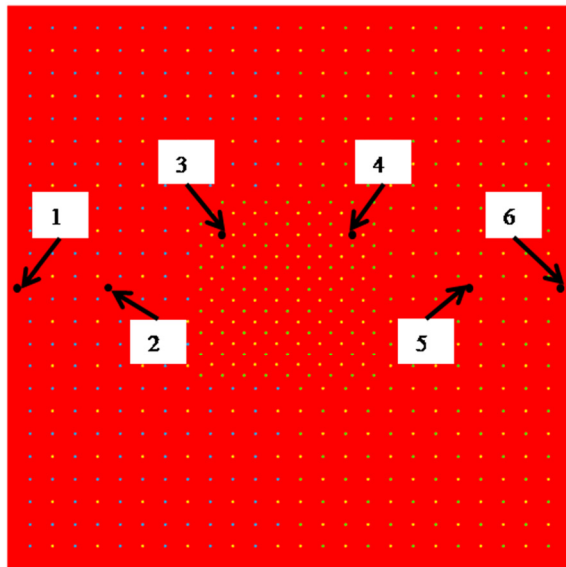
(a)
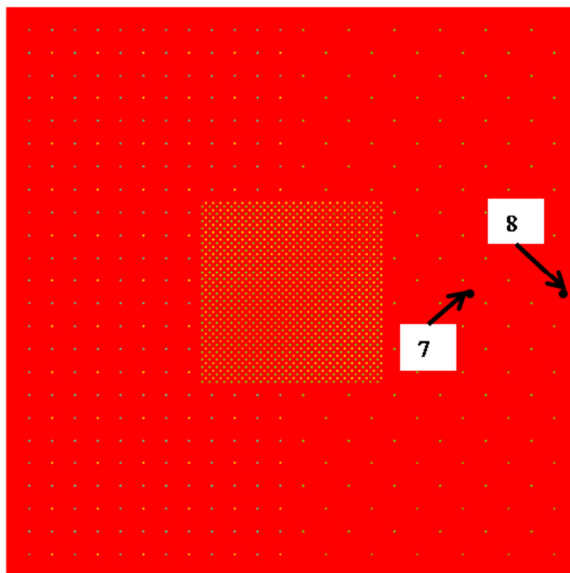
(b)

Fig. 5. Locations and numbering of each observation point at which the electric fields are recorded. (a) Build-up between conducting layers 4 and 5. (b) Build-up between conducting layers 1 and 2.

solder balls between conducting layer 6 and the PCB upper conducting layer. Likewise, Fig. 4(b) shows the source locations for simulation cases 5 and 6 having the excited solder balls in the underfill region connecting the die with the packaging. Each of the two exited solder balls belongs to a different functional layer.   For example, for Simulation Case 1, a solder ball at
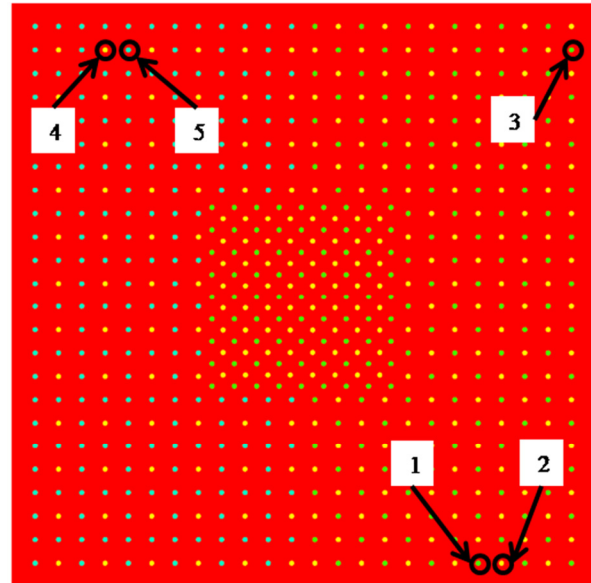
Fig. 6. Location and numbering of the vias between Layers 3 and 4 at which the electric conduction currents are computed.

the lower right corner of the package belonging to the power network is excited, along with a neighboring solder ball to its left belonging to the ground network. Similarly, in Simulation Cases 3, 5, and 6, two neighboring power and ground solder balls are excited as shown in Fig. 4. And in Simulation Cases 4 and 2, two neighboring signal and ground solder balls are excited.

The response of the package to the excitations is based on analyzing the behavior of the electric field throughout the IC, as well as the electric conduction current flowing through the vias. Specifically, the z component of the electric field (Ez) is recorded versus time during each of the six simulation cases at 64 observations points. Figure 5 shows eight key observation points that will be used in this paper to illustrate the variation of the resonances within different zones of the package.

To compute the electric current (Iz), an Ampere's Law contour-line integration of the magnetic field is performed around the vias, of which we have selected five (from 90) to best illustrate the results. Each integration path for these five selected vias lies in the x-y plane at the midpoint between Conducting Layers 3 and 4 as shown in Fig. 6.

The data for both Ez and Iz are normalized relative to the source spectral waveform and then to the maximum value of the response at the

observation point or via having the strongest response to the excitation obtained during time stepping for each corresponding simulation. This second normalization step allows us to compare relative to each other the magnitudes of the observed values within each separate simulation case.

The normalization procedure may be expressed as

$$a_i(f) = \frac{\dfrac{A_i(f)}{S(f)}}{MAX\left[\dfrac{A_{reff}(f)}{S(f)}\right]}, \tag{1}$$

where a_i and A_i refer, respectively, to the normalized and un-normalized values of E_z or I_z for the observation point or via i as a function of frequency f. S refers to the source waveform. The reference A_{reff} is taken to be the corresponding E_z or I_z having maximum peak response to the excitation source relative to the other studied locations for that particular simulation case.

V. RESULTS AND ANALYSIS

The computational results demonstrate that the frequency content of the EM energy observed propagating through the package is determined to be dependent on the spatial location of the source and observation point within the structure and relative to each other. The complex sample package of Fig. 2 therefore cannot be analyzed using the results of a single simulation. Some regions of the package block certain ranges of spectral energy, while the conducting layers naturally block all of the electromagnetic energy within the frequency range of interest. Additionally, mutual coupling shifts the spectral energy and resonances throughout the structure. As a result, different simulation scenarios are performed with the sources spatially varied for each case in order to characterize which zones of the structure lead to specific resonances and behaviors. In this Section, we utilize the results from six simulation cases to demonstrate the resonances, coupling, and shielding produced by different zones within the package.

A. Electric conduction currents

As stated earlier, the package is comprised of a ground network, power network, and signaling vias (functional layers). The computed currents at different vias corresponding to these different functional layers indicate that each functional layer has its own set of resonant frequencies. Because of mutual coupling, these resonances continually shift towards or away from each other as the observation position moves within the package. Simultaneously, we observe in some regions of the structure that some spectral energy is shifted even to spectral ranges not included in the source spectrum (well above 20 GHz). Only while the EM energy propagates through a uniform dielectric region of dimensions on the order of a wavelength do the resulting resonant frequencies remain constant with position.

Simulation Case 1 best illustrates the shifting of the resonances due to mutual coupling. The electric current at Via 1, which is positioned almost directly above the sourced solder balls, shows that the power network resonates at 1.42 and 6.74 GHz. Similarly, the current at Via 2, also positioned almost directly above the sourced solder balls, shows that the ground network resonates at 2.66 GHz. Both Via 1 and Via 2 currents are illustrated in Fig. 7. As we move laterally away from the source location, however, any other vias within the power or ground networks on the right side of the package are found to have resonant frequencies between those of Vias 1 and 2. This is illustrated in Fig. 8 for Via 3, which is on the same right side but opposite end of the structure relative to the sourced solder balls. Via 3 has two resonant frequencies: one at 1.58 which is between the 1.42 and 2.66 GHz resonant frequencies of Vias 1 and 2 and the other at 4.38 GHz which is between the 2.66 and 6.74 GHz resonant frequencies of Vias 1 and 2. Further observations indicate that the higher 4.38 GHz resonance of Via 3 diminishes rapidly as the EM energy propagates through the outer periodic ground and power vias on the right side of the package positioned outside the shadow region of the die. However, the resonance at 1.58 GHz can propagate through these periodic vias.
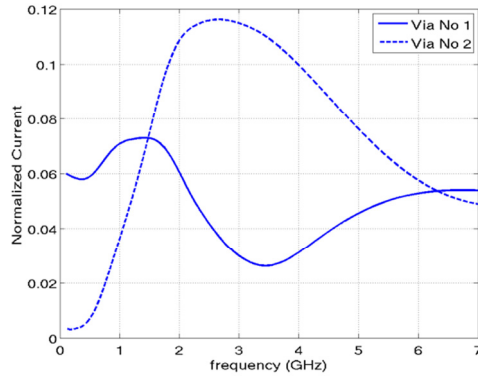
Fig. 7. Spectral response of the electric current at Vias 1 and 2 for Simulation Case 1.
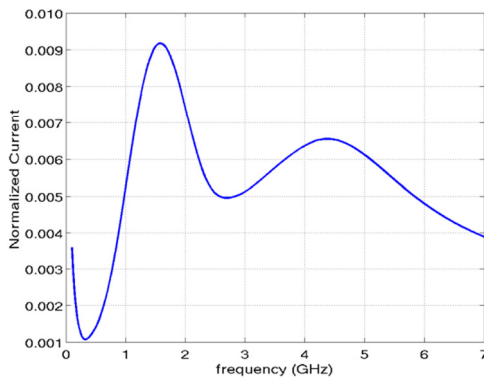
Fig. 8. Spectral response of the electric current at Via 3 for Simulation Case 1.

Regarding the left side of the package, we find from Simulation Case 2 that the ground network weakly resonates at 0.88 GHz on the left side of the package (same side as the sourced solder balls) within the main frequency range of interest (100 MHz to 7 GHz). Figure 9 shows this resonance for Via 4 (ground via), which is positioned on the same left side but opposite end of the structure relative to the sourced solder balls. However, by checking the spectral data of this same via current up to 20 GHz (shown in Fig. 10) instead of 7 GHz, it can be seen that most of the resonance spectral energy of the ground network is above our main frequency range of interest. Within the range of 100 MHz to 7 GHz, the magnitude of the current flowing through each of the signal vias is always an order of magnitude lower than the current flowing through any of its neighboring ground vias. These signal vias thus act to block the EM energy on the left side of the package.

We also find from Simulation Case 2 that the signal vias on the left side of the package do not have any defined resonances between 100 MHz and 7 GHz. Further, most of the signal vias currents on the left side of the package are above 10 GHz, as illustrated for Via 5 (signal via) in Fig. 10.
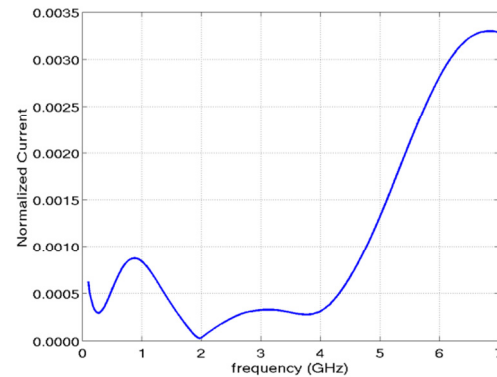
Fig. 9. Spectral response of the electric current at Via 4 for Simulation Case 2.
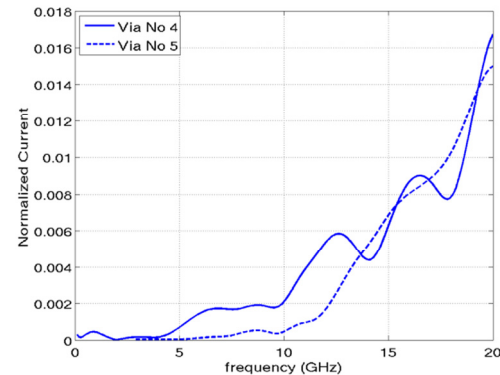
Fig. 10. Spectral response up to 20 GHz of the electric current at Vias 4 and 5 for Simulation Case 2.

B. Electric fields

The build-up between conducting layers 4-5 and 5-6 has two main resonant frequencies on the right side of the package. This is illustrated in Fig. 11 for Simulation Case 1. At observation point 6 (located between conducting layers 4-5 on the same right side of the structure as the sourced solder balls), Ez is observed to have resonances at ~1.80 GHz and ~5.34 GHz, with the higher frequency (~5.34 GHz) resonance being wider band. Note that for Via 3 the Iz resonances were found centered at 1.58 and 4.38 GHz. This further

illustrates the continual shift of resonant frequencies with position. Further, by comparing observation point 6 (positioned on the periphery of the package, just outside the periodic vias) of Fig. 11 with observation point 5 (positioned almost half-way towards the center of the structure) of Fig. 12, it is observed that the higher frequency 5.34 GHz resonance diminishes as the energy propagates from the periphery of the packaging into the periodic structure formed by the vias.
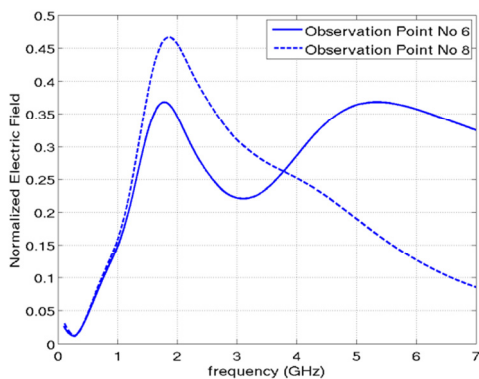
Fig. 11. Spectral response of the electric field at observation points 6 and 8 for Simulation Case 1.
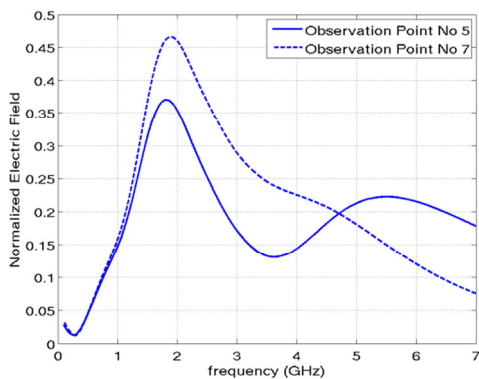
Fig. 12. Spectral response of the electric field at observation points 5 and 7 for Simulation Case 1.

The lower frequency (~1.80 GHz) resonance on the right side of the package is found to be stronger within the build-up between conducting layers 1-2 and 2-3 than in the build-up between conducting layers 4-5 and 5-6. Observation points 7 and 8 (shown in Figs. 11 and 10, respectively) demonstrate these using results from Simulation Case 1. Additionally, the higher frequency resonance (at ~5.34) is no longer present at observation points 7 and 8.

Figure 13 is an example 2-D slice of Ez values that demonstrates the resonances occurring within the core for Simulation Case 1. It is observed that the periphery of the package acts like a transmission line wherein the EM energy propagates at the higher frequencies (5.34 GHz). The reduction of this ~5.34 GHz energy as the EM energy propagates into the periodic vias is also observable in Fig. 13.
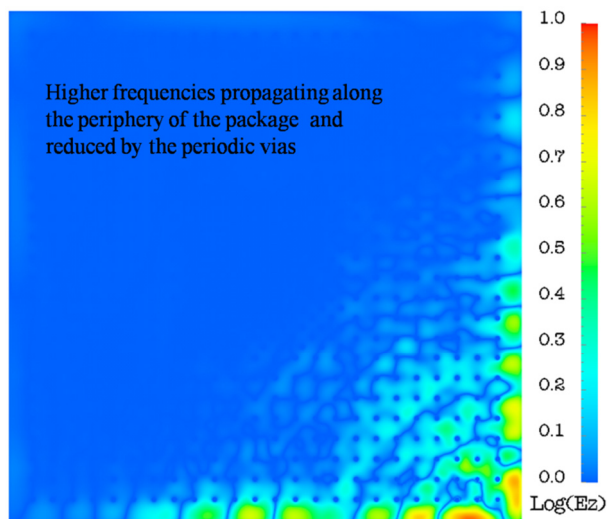
Fig. 13. Electromagnetic energy propagating through the core for Simulation Case 1. A planar cut of Ez values at the midpoint of the gap between conducting layers 3 and 4 is shown.

Simulation Cases 5 and 6 show that the region below the die has two resonances, one at ~500 MHz and the other at ~1.6 GHz (shown in Fig. 14). The strongest amplitudes at these frequencies are located in the build-up between conducting layers 4-5 and 5-6, however these resonances are also significant in the solder balls connecting the silicon layer to the package (underfill layer) as well as in the build-up between conducting layers 1-2 and 2-3. Interestingly, for different Simulation Cases, and thus source locations, these two resonances are also shifted towards each other by varying amounts, resulting for Simulation Cases 1 and 3 in a single but wider bandwidth resonance.

In all of the simulation cases, the strongest response always lies in the build-up layers between conducting layers 1-2, 2-3, 4-5 and 5-6 (numbered according to Fig. 2), but not in the core (between conducting planes 3-4).
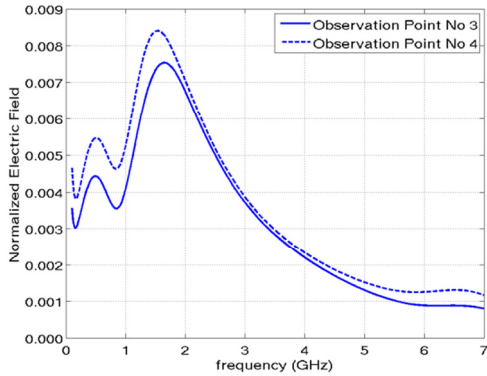
Fig. 14. Spectral response of the electric field at observation points 3 and 4 for Simulation Cases 5 and 6, respectively.

This is because no vias are terminated in conducting layers 3 and 4 bounding the core. That is, at every connection of a via to a conducting plane, EM energy is radiated, and since no vias are terminated on either side of the core, the signal energy is lower within that region. For example, in the snap-shot of Ez shown in Fig. 15, the 1st and 3rd vias (from right to left) are terminated in conducting layer 1. As a result, these vias radiate energy outside (above) the package as well as in the build-up between conducting layers 1 and 2. The 2nd via, however, is terminated in conducting layer 2 and as a result does not radiate energy above the package (above conducting layer 1), but instead radiates energy upwards between conducting layers 1 and 2, and downwards, between conducting layers 2 and 3.
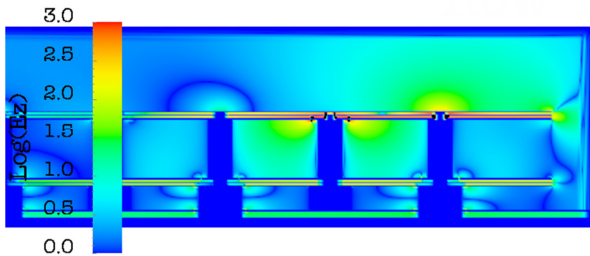
Fig. 15. EM energy propagating through the package for Simulation Case 1. Vertical slice of Ez intersecting the center of Vias 1 and 2. Zoomed-in view to the three right most vias of the entire structure.

Regarding the left side of the package, only the build-up between conducting layers 4-5 and 5-6 resonate weakly at ~680 MHz, as observed at observation point 2 for Simulation Case 2. But as

for the analysis of the currents, this resonance can be neglected compared to all the spectral energy present at frequencies above 7 GHz as shown in Fig. 16.
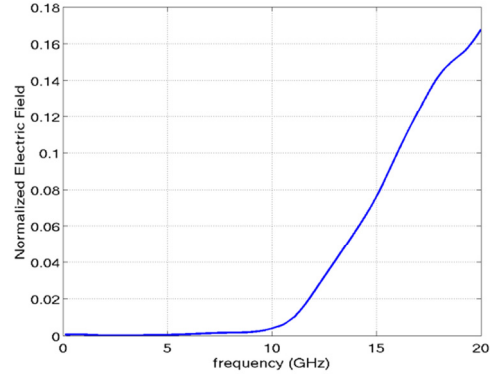
Fig. 16. Spectral response up to 20 GHz for the electric field at observation point 2 for Simulation Case 2.

In Simulation Case 6, which is the only simulation case of the six wherein the source is located on the left side of the package and the excited solder balls correspond to the ground and power networks, most of the signal energy propagates only along the periphery of the left side of the package. This is apparent by comparing observation point 2 with its symmetry observation point 5. A comparison of observation points 1 and 2 for Simulation Case 6 illustrates this effect in Fig. 17.
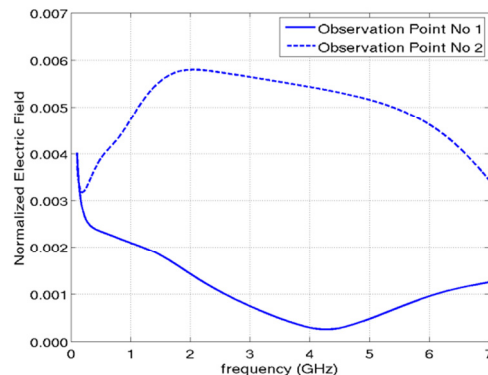
Fig. 17. Spectral response of the electric field at observation points 1 and 2 for Simulation Case 6.

VI. CONCLUSION

We have performed a phenomenological study with the goal of examining resonances and coupling within a sample IC package using a

greater than one-billion cell full-Maxwell's equations FDTD model. Results from six separate simulation cases permitted us to demonstrate the behavior and characteristics of each of the three functional layers of the IC as well as the different regions of the package, such as under-die, left side, right side, core, build-up layers, etc.

Due to the highly complex geometry and interconnections of the IC package along with the effects introduced by the underlying PCB, EMC for IC design is a difficult problem. It is apparent from the results presented in this paper, however, that an external wireless transmitter emitting radiation within the frequency range of 500 MHz to 2 GHz could, depending upon its location and frequency content, present a hazard for specific regions within the IC package. That is, especially if the transmitter's frequency content includes a resonance found in a region of the package and that region of the package lies within a direct propagation path of the transmitter, the radiation from the transmitter may couple into the IC.

ACKNOWLEDGMENT

REFERENCES

[1] "Beyond the Call- Intel and Motorola Explore New Possibilities for the Cell Phone Platform," URL: http://techresearch.intel.com/articles/Exploratory/1431.htm

[2] "Intel's Portable Prototypes," PC Magazine, URL: http://www.pcmag.com/article2/0.2704.1884623,00.aspR. F. Harrington, *Time-Harmonic Electromagnetic Fields*, McGraw-Hill, New York, 1961.

[3] "New Intel Portable PC concept at Computex Paipei 2007," Coolestgadgets.com, URL: http://www.coolest-gadgets.com/20070606/new-intel-portable-pc-concept-atcomputex-taipei-2007

[4] S. R. Sedore, Automated Digital Computer Program for Determining Responses of Electronic Circuits to Transient Nuclear Radiation (SCEPTRE), AFWL TR 66-126, *Air Force Weapons Laboratory*, 1967a.

[5] F. Canavero, S. Grivet-Talocia, I. A. Maio, and I. S. Stievano, "Linear and Nonlinear Macromodels for System-Level Signal Integrity and EMC Assessment," *IEICE Trans. Commun.: Invited Paper, Special section of 2004 International Symposium on EMC*, vol. E88-B, no. 8, pp. 3121-3126, Aug. 2005.

[6] K. Srinivasan, "Multiscale EM and Circuit Simulation using the Laguerre-FDTD Scheme for Package-Aware Integrated-Circuit Design," Ph.D. dissertation, School of ECE, Georgia Institute of Technology, Atlanta, GA, 2008.

[7] K. S. Yee, "Numerical Solution of Initial Boundary Value Problems Involving Maxwell's Equations in Isotropic Media," *IEEE Trans. Antennas Propagat.*, vol. AP-14, issue 8, pp. 302-307, May 1966.

[8] A. Taflove and S. C. Hagness, Computational Electrodynamics: The Finite-Difference Time-Domain Method, 3rd edition. Norwood, MA: Artech House, 2005.

[9] J. J. Simpson, B. Horine, and H. Heck, "Ultra High-Resolution FDTD Modeling of an Integrated Circuit Package for Characterizing and Solving EMC Problems in Compact Portable Electronic Devices," *Proc. IEEE AP-S Intern't Symp. and USNC/URSI Nat '1 Radio Science Meeting*, San Diego, CA, July 2008.

[10] J. J. Simpson, "FDTD Full-Maxwell's Equations Modeling from Near-DC to Light," *Proc. 24th Int'l Review of Progress in Applied Computational Electromagnetics (ACES)*, Niagara Falls, Canada, April 2008.

[11] C. M. Ruiz, J. J. Simpson, B. Horine, and K. Slattery, "Utra High-Resolution FDTD Modeling of a High-Performance VLSI Package," *IEEE AP-S International Symposium and USNC/URSI National Radio Science Meeting*, Charleston, SC, June 2009.

[12] S. Ben Dia, M. Ramdani, and E. Sicard, editors, Electromagnetic Compatibility of Integrated Circuits – Techniques for Low Emission and Susceptibility, Springer, 2006.

[13] F. Xu and K. Wu, "Guided-Wave and Leakage Characteristics of Substrate Integrated Waveguide," *IEEE Trans. Microw. Theory Tech.*, vol. 53, no. 1, pp. 66–73, Jan. 2005.

[14] S. Shahparnia and O. M. Ramahi, "A Simple and Effective Model for Electromagnetic Bandgap Structures Embedded in Printed Circuit Boards," *IEEE Microw. Wireless Compon. Lett.*, vol. 15, no. 10, pp. 621–623, Oct. 2005.

[15] S. Shahparnia and O. M. Ramahi, "Miniaturazed Electromagnetic Bandgap Structures for Ultra-Wide Band Switching Noise Mitigation in High-Speedprinted Circuit Boards and Packages," *in Proc. 13th Topical Meeting Electrical Performance Electronic Packaging.*, pp. 211-214, Portland, OR, Oct. 25-27, 2004.

[16] C. Guiffaut and K. Mahdjoubi, "A Parallel FDTD Algorithm Using the MPI Library," *IEEE Antennas Propag. Mag.*, vol. 43, no. 2, pp. 94–103, Apr. 2001.

[17] M. Piket-May, A. Taflove, and J. Baron, "FD-TD Modeling of Digital Signal Propagation in 3-D Circuits with Passive and Active Loads," *IEEE Trans. Microwave Theory and Tech.*, vol. 42, no. 8, pp. 1514-1523, Aug, 1994.

César Méndez Ruiz was born in México City, México, on June 1, 1980. He received the B.S. diploma in Electromechanical Engineering from the Universidad Panamericana, Zapopan, Jalisco, México, in 2003, and the M.S. degree in Electronic Engineering from the Universidad de Guadalajara, Guadalajara, Jalisco, México, in 2007. He is currently working toward the Ph.D. degree in Applied Electromagnetics at the University of New Mexico, Albuquerque, NM.
From 2002 to 2003, he was a trainee in Hewlett-Packard (HP). He has professional experience in R&D area working as a mechanical design engineer for HP and Best in Development and Technology (BDT).

Jamesina J. Simpson received the B.S. and Ph.D. degrees in Electrical Engineering from Northwestern University, Evanston, IL, in 2003 and 2007, respectively. As a graduate student, Dr. Simpson was a recipient of the National Science Foundation Graduate Research Fellowship, IEEE AP-S Graduate Research Award, and IEEE MTT-S Graduate Fellowship.
In 2007, Dr. Simpson joined the Electrical and Computer Engineering Department at the University of New Mexico – Albuquerque as a tenure-track Assistant Professor. Her research lab encompasses the application of the full-Maxwell's equations finite-difference time-domain (FDTD) method to model a wide variety of scientific and engineering applications. In 2010, Dr. Simpson was awarded an NSF CAREER grant.

Compact Antenna Designs for Wearable and Portable Medical System

Wei Huang and Ahmed A. Kishk

Department of Electrical Engineering
University of Mississippi, University, MS 38677 USA
ahmed@olemiss.edu and whuang1@olemiss.edu

Abstract- A button wearable antenna and an L-shape planar inverted F antenna (PIFA) antenna were designed for medical eHealth system. A spiral top button wearable antenna was implemented into the antenna structure to obtain additional inductance. Both simulated and measured reflection coefficients show it can cover both the 2.4-2.5GHz and 5.15- 5.825 GHz ISM bands. Good omnidirectionality was achieved at x-y plane for all three bands. A compact L-shape PIFA antenna was designed and fabricated for laptop wireless local area network (WLAN) application to communicate with wearable antenna. The antenna was formed to L-shape to minimize the ground plane size, so that it can be fitted into the top corners of a laptop display. The effect of the presence of display panel was discussed.

I. Introduction

New microwave technologies have an ever-growing impact on our lives, and the personalized healthcare sector is no exception. For more than ten years, the European Commission has been trying to extend healthcare beyond hospitals to people's homes through an eHealth system. The system could optimize the communication between patients and doctors and allow early diagnosis and more cost-effective patient monitoring and consulting beyond the ordinary hospital environment [1]. The eHealth system could be in the form of wearable, or portable systems, as well as in-vitro point-of-care diagnostic devices for home use [2]. Wearable systems are able to monitor patients' health-related parameters such as heart rate, temperature, blood oxygen, etc. continuously and process and feed the information to the doctors. The portable system can be in the form of small wireless devices, such as a handset or laptop, which can operate at any location. They can be used to communicate with an implantable or wearable system or temporarily attached to the human body to have the similar function as a wearable system. The antenna is an essential part of wearable, or portable eHealth systems. The design complexity depends on the radio transceiver requirements as well as the propagation characteristics of the surrounding environment.

Wearable antennas have the advantages of low profile, small size and a relatively high gain. The existing wearable antenna designs include the microstrip patch antennas attached to clothing fabric substrate, and the so-called "textile type" wearable antenna. A rectangular patch with probe feed and linear polarization or with microstrip feed and circular polarization were studied in [3-4]. However, the fabric type of substrate has poor electrical properties as well as poor ability for moisture-proofing. To overcome these problems, small size button antennas were introduced [5-7]. Such button-shaped cylindrical structures with a metal disk on top connected to a ground plane were designed from the actual jeans button structure.

They can be considered as top loaded monopoles mounted on a fabric substrate. Due to its small ground plane, fabric substrate has much less effect on the performance of the "button type" wearable antenna as compared with "textile type" ones. Plus, a small ground plane also guarantees the flexibility of the antenna. The proposed wearable antenna is inspired by a conventional denim jeans button and can be used as a standard button for various garments. As shown at Fig.1, different from previous button antenna designs, a spiral top is implemented into the antenna structure as an additional inductor element. The button antenna is residing on a fabric substrate with ground plane at the bottom. A 50 Ohm coaxial probe is used underneath the ground plane to excite the antenna.
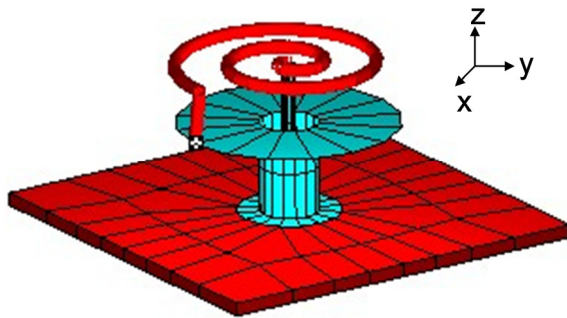
Fig. 1.   WIPL-D [8] model of the multi-band spiral top button antenna.

Nowadays, laptop usually acts as the portable system which is used to communicate with the wearable system. With the fast development of wireless local area networks (WLAN), more and more laptop computer manufacturers desire to integrate WLAN devices into their laptops. An integrated antenna for laptop computers is one of the most important parts in the design of laptop WLAN communication systems (e.g. Bluetooth, Wi-Fi, Wi-Max). In [9], an inverted-F antenna was designed on a PC card and was integrated into laptop computers by inserting the PC card into a laptop PC slot. To avoid the physical breakage and damage associated with external plug-in antennas, however, more and more laptop manufacturers prefer the complete integration of

communication systems into laptops [10]. To avoid the shadowing effect from the laptop system and external environmental influence such as metal desks and user's hands or laps, as mentioned in [11], antennas are suggested to be mounted around the top or close to the top of the laptop display to achieve best coverage. To provide polarization diversity, usually more than one antenna is needed.

Here, a low profile L-shape PIFA antenna is designed and fabricated for laptop WLAN application. The total antenna size including ground plane is small enough to fit in either the left or the right corner of a laptop display, as shown at Fig. 2. The new antenna is an extension of the original PIFA antenna concept by bending its substrate and ground plane to an L-shape, as shown at Fig. 3. Since usually laptop manufactures use extensive conducting shields inside the covers of the laptops to minimize radiation from high-speed processors, one of the major design challenges associated with wireless integration into laptops is to design an antenna which can radiate efficiently under such environment. Since the laptop keyboard base is electrically far from the proposed antenna locations, the lossy conducting LCD is the major factor to affect antenna performance. Therefore, to study the effect of the laptop on the antenna performance, a parasitic lossy PCB panel is used to mimic the laptop LCD panel. Both the cases of antenna alone and with display panel are simulated and measured. A full coverage of 2.4-2.5GHz ISM band is achieved. The effect of the presence of display panel is discussed.

Fig. 2. Proposed antenna locations inside of a laptop computer.

(a)

(b)
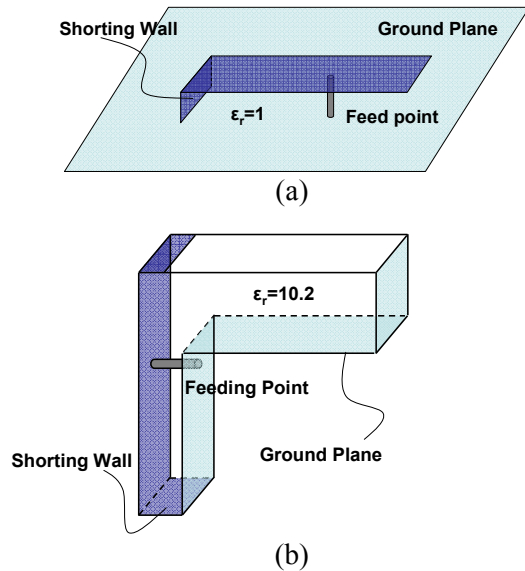
Fig. 3. (a) Original PIFA; (b) Proposed L-shape PIFA.

II. MULTI-BAND BUTTON WEARABLE ANTENNA

In this section, a multi-band spiral top button antenna was designed, fabricated and tested as a wearable electronic device for wireless local area network (WLAN) application. Compared with "textile type" wearable antenna, it has the advantages of compact size, small ground plane, less dependence on the fabric substrate. A spiral top was implemented into the antenna structure to obtain additional inductance. Both simulated and measured reflection coefficients are presented. Three resonance bands are achieved which cover both the 2.4-2.5GHz and 5.15-5.825 GHz industrial, scientific and medical (ISM) bands. Simulated far-field total gain patterns are also illustrated. Good omni-directionality is achieved at the x-y plane for all three bands.

2.1 Antenna design and geometry

Figure 4 shows both side and top views for the proposed multi-band spiral top button antenna mounted on a grounded fabric substrate. The whole antenna can be considered as a piece of air-filled coaxial line with inner conductor bent into a spiral shape and outer conductor folded into a circular disk as the cap of the button. The tail of the spiral is connected to the

edge of the disk at point (J). The inner conductor also connects to another small base circular disk. The fabric substrate is modeled with dielectric constant of (ε_r) 1.3. The radius of the spiral top (A) is 8.5 mm and the number of turns is 3. The total length of meandered wire is around 54 mm. The radii of the inner and the outer conductors are 0.5 mm and 2.25 mm, respectively. The lower disk has a radius B of 8.5 mm. The radius of the base disk D is as small as 4 mm, which guarantees the flexibility of the antenna. The gap between spiral upper and lower disk is 4.5 mm while the distance between the lower disk and base disk is 7 mm. A 50 Ω coaxial probe is used to excite the button antenna. The antenna is designed with the help of WIPL-D.

(a) Side view

(b) Top view
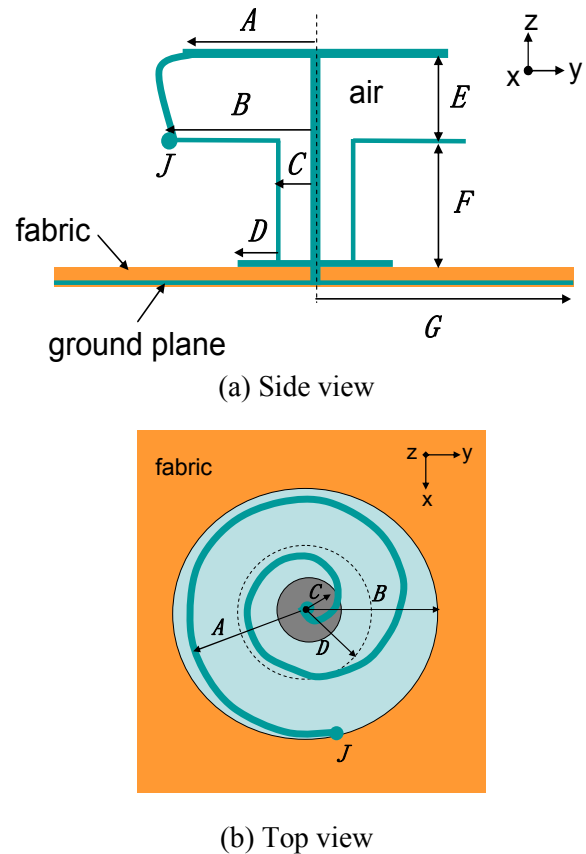
Fig. 4.   Geometry of spiral top button antenna.

In the experimental model, the button antenna is made of copper. A 50 Ohms coaxial

cable with a SMA connector is used to excite the antenna. The spiral top is made by meandering the inner conductor of the coaxial cable. The fabric material is canvas which is commercially available, flexible and resistant to compression of its height. The bottom ground plane is made of adhesive copper tape which is also able to ensure the flexibility. Figure 5 shows photographs of the fabricated multi-band spiral top button antenna.

(a) Side view
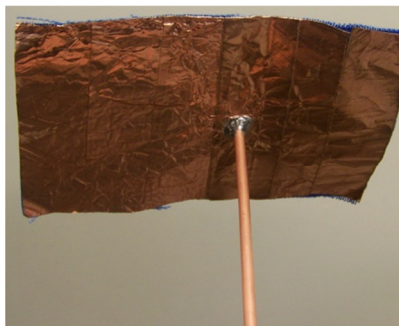
(b) Bottom view

Fig. 5. Photo of fabricated spiral top button antenna.

2.2 Simulation and measurement results

Figure 6 shows both simulated and measured reflection coefficients curves of the proposed multi-band spiral top button antenna in free space. The dashed horizontal line marks the criterion for VSWR=2.5. The matching frequency band of the simulated results for this criterion is from 2.45 GHz to 2.6 GHz, 3.3 GHz to 3.4 GHz, and 4.1 GHz to 6.3 GHz. The

frequency band of the measured result for this criterion is from 2.3 GHz to 2.7 GHz, 3.3 GHz to 3.4 GHz, and 3.9 GHz to 6.5 GHz. The calculated and measured values are in agreement. It can be noticed that the antenna bandwidth is wide enough to cover the 2.4-2.5GHz and 5.15-5.825 GHz ISM bands. It is assumed that a better impedance matching is attained in the measured results due to the loss copper material used and some fabrication tolerances, such as the bending of spiral wires, etc. The parametric studies for different lengths of the meandered wire, sizes of upper disk and lower disk, and different gaps and heights are also performed. But for the sake of the brevity, these results will not be presented here.
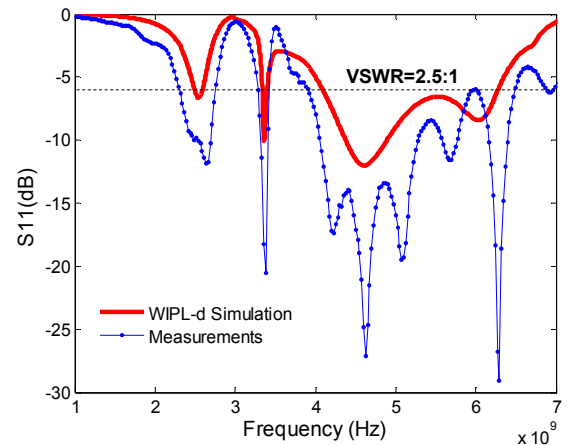
Fig. 6. Simulated and measured reflection coefficients of spiral top button antenna.

Figures 7 (a), (b), and (c) provide the simulated co-polarization and cross-polarization of the far-field gain patterns for the proposed multi-band spiral top button antenna at 2.5 GHz, 3.35 GHz and 5.2 GHz in the horizontal plane (x-y plane). It is shown that the total gain pattern has good omnidirectionality in the horizontal plane at both 2.5 GHz and 5.2 GHz. Since the z-axis is normal to wearer's body, as mentioned in [7], the shown far-field gain patterns indicate that some radiation is tangential to the body of wearer which may be beneficial for connecting to other wearable devices.
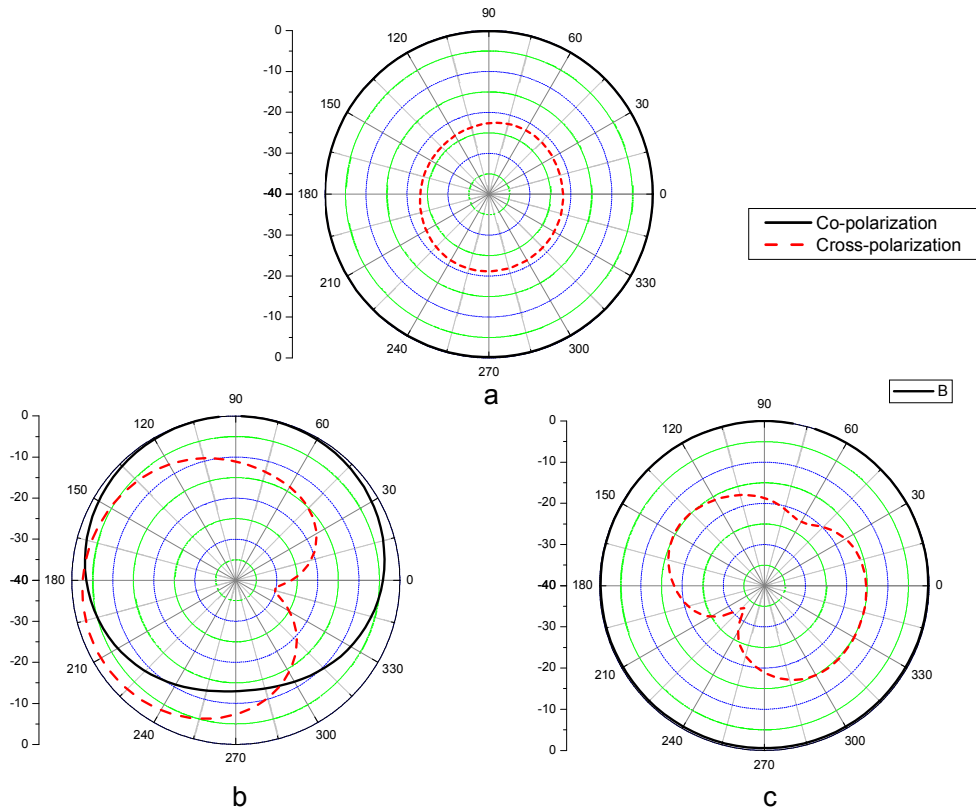
Fig. 7. Simulated x-y plane radiation patterns of spiral top button antenna: (a) 2.5 GHz; (b) 3.35 GHz; (c) 5.2 GHz.

III. L-SHAPE PIFA DESIGN FOR LAPTOP WIRELESS COMMUNICATION

3.1 Antenna design and geometry

Figure 8 shows the geometry of the proposed L-shape PIFA. The new PIFA can be regarded as the original PIFA bent into a L-shape. The ground plane has the same width (W=5 mm) as the antenna top surface. Instead of free space, the dielectric material Rogers RT/Duroid 6010 with dielectric constant (ε_r) of 10.2 is used as the substrate. The heights of the L-shape PIFA in x-dimension and z-dimension are A (24.5 mm) and B (23 mm), respectively. The distance between the antenna top surface and ground plane or the shorting wall height C is 3.85mm. The height D is 13.9 mm and the width E is 22.65 mm. A 50 Ω coaxial probe excites the antenna. The height of the probe inside of the antenna is the same as C and the probe location G is 12.73 mm high at the center of W. The top

horizontal part of the L-shape antenna has the height F of 9.1 mm. The antenna is designed using the frequency domain commercial software, WIPL-D. WIPL-D is based on the surface integral equations and method of moments. It should be mentioned that in the fabrication model the electric conducting tape is used to model both the antenna top surface and ground plane. Fig. 5.9 (a) shows the photograph of a fabricated L-shape PIFA. A lossy PCB panel with size of 30 mm x 25 mm is used to mimic the lossy conducting laptop LCD, as shown at Fig. 5.9 (b).

3.2 Simulation and measurement results

Figure 10 (a) shows simulated and measured reflection coefficients curves of the L-shape PIFA alone in free space. The dashed horizontal line marks the criterion for VSWR=2.5. The frequency bandwidth of the simulated results for this criterion is from 2.4 GHz to 2.7 GHz. The bandwidth of the measured result for this criterion is from 2.33 GHz to 2.71 GHz. The calculated and measured values are in good

agreement. The reflection coefficient curves of the L-shape PIFA with the parasitic lossy PCB panel are shown in Fig. 10 (b). The frequency bandwidth of the simulated and measured results for the VSWR=2.5 criteria, is from 2.43 GHz to 2.73 GHz and from 2.3 GHz to 2.82 GHz, respectively. It can be noticed that the antenna bandwidth is wide enough to cover the 2.4-2.5GHz industrial, scientific, and medical (ISM) band. It is also noted that better matching is attained for the antenna with the lossy PCB panel due to the reduced Q factor of the antenna system.
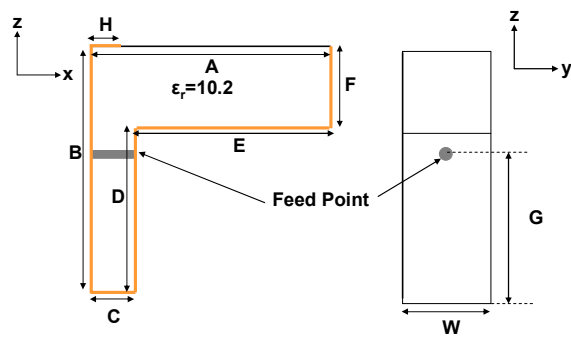
Fig. 8. Geometry of L-shape PIFA.

(a)   (b)
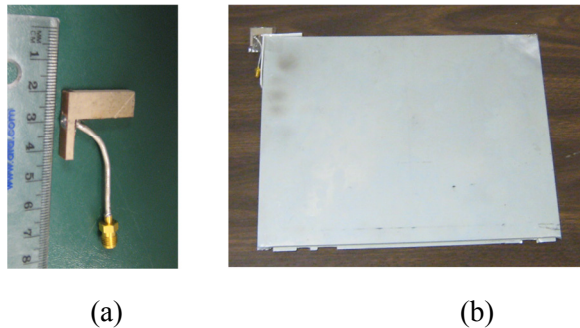
Fig. 9. Photo of fabricated antenna: (a) alone; (b) with lossy PCB panel.
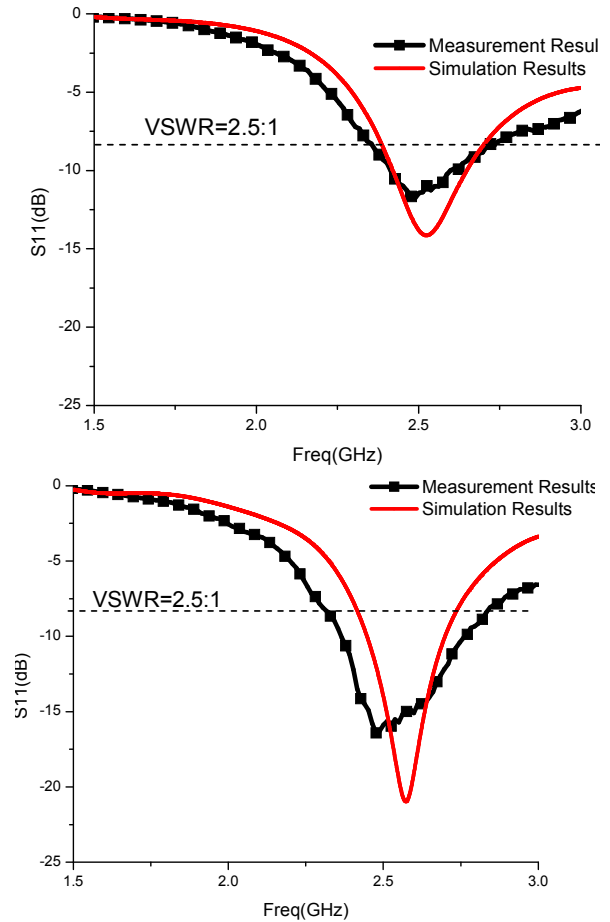
Fig. 10. Simulated and measured S_{11} for antenna (a) alone (b) with lossy PCB panel.

Figure 11 (a) and (b) provide the simulated far-field gain patterns of L-shape PIFA alone and with lossy PCB panel at 2.5 GHz in the horizontal plane (xy-plane) and vertical (yz-plane) plane, separately. It is shown that the total gain pattern is almost omnidirectional in the horizontal plane for antenna alone case. For antenna with lossy PCB panel, as we expected, the deformation of the radiation patterns is occurred. But the antenna radiates most of the energy away from the front, back, and left side of the display. The vertical plane radiation pattern is almost omnidirectional for both cases.
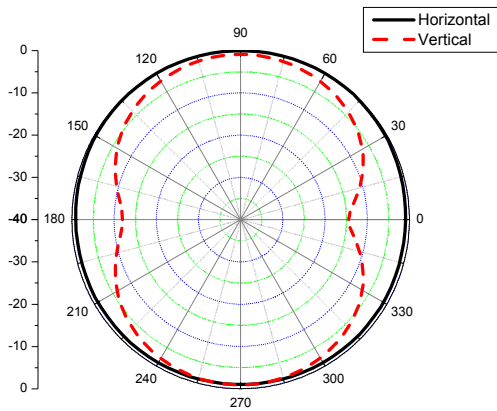
(a)
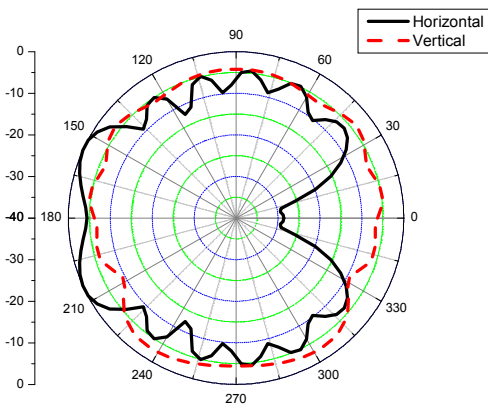
(b)

Fig. 11. Simulated total far-field gain patterns at 2.5GHz: (a) antenna alone; (b) antenna with lossy PCB panel.

IV. CONCLUSIONS

A button wearable antenna and an L-shape PIFA antenna were designed for medical eHealth system. The multi-band spiral top button antenna was designed, fabricated and tested for WLAN application. A spiral top was implemented into the antenna structure to obtain additional inductance. The button antenna was fed by a 50 Ohm coaxial probe with the ground plane underneath. Both simulated and measured reflection coefficients were presented. Three resonance bands were achieved at 2.4-2.6 GHz, 3.3-3.4 GHz, and 4-5.25 GHz, respectively, which cover both the 2.4-2.5GHz and 5.15-5.825 GHz ISM bands. Simulated far-field total gain patterns were also obtained. Good omnidirectionality was achieved at x-y plane for all three bands. A compact L-shape PIFA antenna was designed and fabricated for laptop WLAN application. The antenna was formed to L-shape to minimize the ground plane size, so that it can be fitted into the top corners of a laptop display. A parasitic lossy PCB panel was used to mimic laptop LCD panel. Both the cases of antenna alone and with display panel were simulated and measured. A full coverage of 2.4-2.5GHz ISM band was achieved for both cases. Simulated far-field total gain patterns were also presented. The effect of the presence of display panel was discussed.

REFERENCES

[1] Lymberis and S. Olsson, "Intelligent Biomedical Clothing for Personal Health and Disease Management: State of the Art and Future Vision," *Telemed. J. e-Health*, vol. 9, pp. 379-386, 2003.

[2] L. Gatzoulis and I. Iakovidis, "Wearable and Portable eHealth Systems," *IEEE Medicine and Biology Magazine*, vol. 26, pp. 51-56, 2007.

[3] W. Huang and A. Kishk, "The Effect Study of Microstrip Patch Antenna Bending for Wearable Applications," *MAESC 2005 Conference*, Memphis, TN, 2005.

[4] M. Klemm, I. Locher and G. Tröster, "A Novel Circularly Polarized Textile Antenna for Wearable Applications," *Proceedings of 7th European Microwave Week*pp., 137-140, Amsterdam, Nederlands, 2004.

[5] B. Sanz-Izquierdo, F. Huang, and J. C. Batchelor, "Small Size Wearable Button Antenna," *Proceedings of EuCAP*, Nice, France, 2006.

[6] B. Sanz-Izquierdo, J. C. Batchelor, and M. Sobhy, "UWB Wearable Button Antenna," *Proceedings of EuCAP*, Nice, France, 2006.

[7] B. Sanz-Izquierdo, F. Huang, and J. C. Batchelor, "Covert Dual-Band Wearable Button Antenna," *Electron. Lett.*, vol. 42, pp. 668 – 670, 2006.

[8] B. Kolundzija and A. Djordjevic, "WIPL-D Professional v5.1 Electromagnetic Modeling of Composite Metallic and Dielectric Structures: Software and Users Manual," *WIPL-D Ltd.*, 2004.

[9] J. Guterman, Y. Rahmat-Samii, A. A. Moreira, and C. Peixeiro, "Radiation from Commercially Viable Antennas for PCMCIA Cards Housed in Laptops," 2007 16th IST Mobile and Wireless Communications Summit, vol. 1, pp. 1-4.

[10] D. Liu, B. P. Gaucher, E. B. Flint, T. W. Studwell, H. Usui, and T. J. Beukema, "Developing Integrated Antenna Subsystems for Laptop Computers," *IBM J. RES. & DEV.*, vol. 47, pp. 355-367, 2003.

[11] E. C. Fear and M. Okoniewski, "Confocal Microwave Imaging for Breast Tumor Detection: Application to a Hemispherical Breast Model," *IEEE MTT Symp.*, vol. 3, pp. 1759 – 1762, 2002.

Coupled Mode Analysis of Two-Dimensional Chiral Grating

Ahmed M. Attiya

Microwave Engineering Department
Electronics Research Institute, El-Tahreer St. Dokki, Giza, Egypt, 12622
aattiya@ksu.edu.sa

Abstract ─ This paper introduces a modal analysis for two-dimensional chiral grating. The grating structure is composed of rectangular chiral rods arranged in rectangular periodic cells and embedded in another chiral base material. Total fields are presented in terms of transverse electric and magnetic field components which are expanded as two sets of TE and TM Floquet modes. This representation is used in Maxwell's curl equations to formulate the problem as an eigenvalue problem. The resulting eigenvalues correspond to the forward and backward propagation coefficients. On the other hand, the eigenvectors correspond to the amplitudes of the TE and TM Floquet modes in the forward and backward propagating modes. Reflection and transmission coefficients of two semi-infinite chiral gratings are obtained by combining this modal analysis and mode matching method. This analysis is extended to obtain the reflection and transmission coefficients of a finite thickness two-dimensional chiral grating slab by using the generalized scattering matrix method.

Index Terms ─ Chiral medium, grating, modal analysis, mode matching.

I. INTRODUCTION

Electromagnetic interaction with periodic structures has significant importance in many applications like filters, frequency selective surfaces, artificial media, etc. This problem can be viewed from different points of view like the amplitude of the reflection and transmission coefficients as in the case of frequency selective surfaces and the phase of the transmitted wave as in the case of artificial metamaterials. Chiral medium introduces an additional point which is the polarization conversion and electro-magnetic coupling. This is the motivation in the present paper and other previously published papers to study electromagnetic wave interaction with periodic chiral structures [1-4]. Guiding properties of infinite multi-layers chiral slab was discussed by using modal analysis. This modal analysis of periodic layered chiral slabs is extended to study the reflection and transmission of a one-dimensional chiral grating slab by using the mode matching method [4].

The present paper extends this modal analysis to study the reflection and transmission of an obliquely incident TE or TM plane wave due to a two-dimensional chiral grating slab as shown in Fig. (1). The slab is composed of rectangular rods implanted inside a base substrate in a rectangular periodic scheme. Similar analysis is discussed by the author with others for both two-dimensional dielectric and two-dimensional magneto-dielectric grating slabs [5-6]. However, the key difference in the present case is the coupling between the electric and magnetic fields due to the chirality coefficient. In dielectric grating and magneto-dielectric grating the formulation begins with the wave equation in the corresponding medium. For these cases, the wave equation is simply a second order differential equation and both electric and magnetic field components are separated. However, in the present case the wave equation in the chiral medium is a fourth order differential equation [7]. Thus, it would be much more complicated to start the present formulation with wave equation as in the cases of dielectric and magneto-dielectric gratings. This is the motivation here to formulate the problem starting from Maxwell's curl equations. Similar analysis is

discussed for the problems of chirowaveguides and chirowaveguide discontinuities by using the coupled mode analysis. [8-13]. Method of moments has also been used to simulate transmission of plane waves through an aperture in a conducting plane in the presence of a chiral medium [14]. This method can be extended to simulate the periodic patch or slots on a chiral slab. However, it would be quite complicated to simulate a 2-D grating slab since the problem would be the volume integral equation instead of the simple surface integral equation.
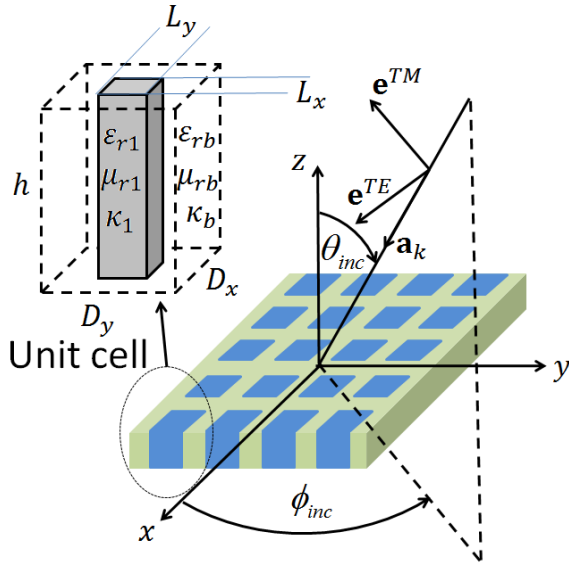
Fig. 1. A two-dimensional chiral grating slab excited by an obliquely incident TE and TM plane waves.

In the following section, the modal analysis of an infinite chiral grating is presented as an eigenvalue problem where the eigenvalues correspond to the complex propagation wave numbers in the longitudinal direction and the eigenvectors represent the transverse field distributions of the different modes in this infinite periodic structure. This modal analysis is combined with the mode matching method to obtain the scattering matrix of a semi-infinite grating. Then the generalized matrix approach combined with complex propagation wave numbers of the different modes in the infinite grating structure are used to obtain the reflection and transmission coefficients of the finite-thickness chiral grating slab. The present analysis

represents a generalization to the previously published analysis for one-dimensional chiral grating [4] where the same results of the one-dimensional case can be obtained by extending the length of the implanted rod in y direction L_y to be the same as the cell size in the same direction D_y.

These points are discussed in detail in Sec. III in addition to other results and discussions related to the two-dimensional chiral grating slab.

II. THEORY

A. Modal analysis of infinite two-dimensional chiral grating

Total fields inside the chiral grating are divided into transverse and longitudinal components as follows:

$$\mathbf{E}(x,y,z) = \mathbf{E}_t(x,y,z) + E_z(x,y,z)\mathbf{a}_z , \quad (1\text{-}a)$$

$$\mathbf{H}(x,y,z) = \mathbf{H}_t(x,y,z) + H_z(x,y,z)\mathbf{a}_z . \quad (1\text{-}b)$$

The transverse field components are expanded as an infinite series of bi-orthogonal Floquet TE and TM modes propagating along the longitudinal direction:

$$\mathbf{E}_t = \sum_p \Phi_{(p)}^{TE} \widetilde{\mathbf{e}}_{(p)}^{TE}(x,y) e^{-j\beta_{(p)}^{TE}z} + \Phi_{(p)}^{TM} \widetilde{\mathbf{e}}_{(p)}^{TM}(x,y) e^{-j\beta_{(p)}^{TM}z},$$

$$(2\text{-}a)$$

$$\mathbf{H}_t = \sum_p C_{(p)}^{TE} \widetilde{\mathbf{h}}_{(p)}^{TE}(x,y) e^{-j\beta_{(p)}^{TE}z} + C_{(p)}^{TM} \widetilde{\mathbf{h}}_{(p)}^{TM}(x,y) e^{-j\beta_{(p)}^{TM}z},$$

$$(2\text{-}b)$$

where $\Phi_{(p)}^{TE}$, $\Phi_{(p)}^{TM}$, $C_{(p)}^{TE}$, and $C_{(p)}^{TM}$ are four sets of unknown amplitudes to be determined. $\beta_{(p)}^{TE}$ and $\beta_{(p)}^{TM}$ are the longitudinal propagation constants of the $(p)^{th}$ TE and $(p)^{th}$ TM mode, respectively. For computational purpose, these infinite series are truncated at an upper limit $p = P$ assuming that they start from $p = 1$. The transverse expansion functions of the electric and magnetic fields are given by:

$$\widetilde{\mathbf{e}}_{mn}^{TE}(x,y) = T_{mn}\left(k_{yn}\mathbf{a}_x - k_{xm}\mathbf{a}_y\right)/k_{tmn} , \quad (3\text{-}a)$$

$$\widetilde{\mathbf{e}}_{mn}^{TM}(x,y) = T_{mn}\left(k_{xm}\mathbf{a}_x + k_{yn}\mathbf{a}_y\right)/k_{tmn} , \quad (3\text{-}b)$$

$$\widetilde{\mathbf{h}}_{mn}^{TE}(x,y) = T_{mn}\left(k_{xm}\mathbf{a}_x + k_{yn}\mathbf{a}_y\right)/k_{tmn} , \quad (3\text{-}c)$$

$$\widetilde{\mathbf{h}}_{mn}^{TM}(x,y) = T_{mn}\left(-k_{yn}\mathbf{a}_x + k_{xm}\mathbf{a}_y\right)/k_{tmn} , \quad (3\text{-}d)$$

where

$$k_{xm} = k_0 \sin\theta_{inc}\cos\phi_{inc} + 2\pi m / D_x , \quad (4\text{-}a)$$

$$k_{yn} = k_0 \sin\theta_{inc} \sin\phi_{inc} + 2\pi n / D_y, \quad \text{(4-b)}$$

$$T_{mn} = \left(1/\sqrt{D_x D_y}\right)\exp(-jk_{xm}x - jk_{yn}y) , \quad \text{(4-c)}$$

$$k_{tmn} = \sqrt{k_{xm}^2 + k_{yn}^2} . \quad \text{(4-d)}$$

It should be noted that each value of the suffix (p) in (2) corresponds to a unique combination of m and n. The specular mode has the value of $p = p_{00}$ that corresponds to $m=0$ and $n=0$. By using these modal expansion functions of (3) in (2), one can obtain the transverse field components as follows:

$$E_x = \sum_p \frac{\left(\Phi_{(p)}^{TE} k_{y(p)} e^{-j\beta_{(p)}^{TE}z} + \Phi_{(p)}^{TM} k_{x(p)} e^{-j\beta_{(p)}^{TM}z}\right) T_{(p)}}{k_{t(p)}} , \quad \text{(5-a)}$$

$$E_y = \sum_p \frac{\left(-\Phi_{(p)}^{TE} k_{x(p)} e^{-j\beta_{(p)}^{TE}z} + \Phi_{(p)}^{TM} k_{y(p)} e^{-j\beta_{(p)}^{TM}z}\right) T_{(p)}}{k_{t(p)}} , \quad \text{(5-b)}$$

$$H_x = \sum_p \frac{\left(C_{(p)}^{TE} k_{x(p)} e^{-j\beta_{(p)}^{TE}z} - C_{(p)}^{TM} k_{y(p)} e^{-j\beta_{(p)}^{TM}z}\right) T_{(p)}}{k_{t(p)}} , \quad \text{(5-c)}$$

$$H_y = \sum_p \frac{\left(C_{(p)}^{TE} k_{y(p)} e^{-j\beta_{(p)}^{TE}z} + C_{(p)}^{TM} k_{x(p)} e^{-j\beta_{(p)}^{TM}z}\right) T_{(p)}}{k_{t(p)}} , \quad \text{(5-d)}$$

where

$$T_{(p)} = \left(1/\sqrt{D_x D_y}\right)\exp(-jk_{x(p)}x - jk_{y(p)}y), \quad \text{(6-a)}$$

$$k_{t(p)} = \sqrt{k_{x(p)}^2 + k_{y(p)}^2} . \quad \text{(6-b)}$$

The constitutive relations in a chiral medium can be presented as:

$$\mathbf{D} = \varepsilon_0 \varepsilon_r \mathbf{E} - j\kappa\sqrt{\mu_0\varepsilon_0}\mathbf{H} , \quad \text{(7-a)}$$

$$\mathbf{B} = \mu_0 \mu_r \mathbf{H} + j\kappa\sqrt{\mu_0\varepsilon_0}\mathbf{E} , \quad \text{(7-b)}$$

where κ is the chirality coefficient. Based on these constitutive relations, one can obtain the longitudinal field components in terms of the longitudinal electric and magnetic flux densities as follows:

$$E_z = \left[\left(\mu_r / \varepsilon_0\right)D_z + \left(j\kappa/\sqrt{\mu_0\varepsilon_0}\right)B_z\right]/\xi , \quad \text{(8-a)}$$

$$H_z = -\left[\left(j\kappa/\sqrt{\mu_0\varepsilon_0}\right)D_z - \left(\varepsilon_r / \mu_0\right)B_z\right]/\xi , \quad \text{(8-b)}$$

where $\xi = \mu_r\varepsilon_r - \kappa^2$. By applying Maxwell's curl equations, one can obtain these longitudinal electric and magnetic flux densities as functions of the derivatives of the transverse electric and magnetic field components as follows:

$$E_z = \frac{1}{j\omega\xi}\left[\frac{\mu_r}{\varepsilon_0}\left(\frac{\partial H_y}{\partial x} - \frac{\partial H_x}{\partial y}\right) - \frac{j\kappa}{\sqrt{\mu_0\varepsilon_0}}\left(\frac{\partial E_y}{\partial x} - \frac{\partial E_x}{\partial y}\right)\right],$$
$$\text{(9-a)}$$

$$H_z = \frac{-1}{j\omega\xi}\left[\frac{j\kappa}{\sqrt{\mu_0\varepsilon_0}}\left(\frac{\partial H_y}{\partial x} - \frac{\partial H_x}{\partial y}\right) + \frac{\varepsilon_r}{\mu_0}\left(\frac{\partial E_y}{\partial x} - \frac{\partial E_x}{\partial y}\right)\right],$$
$$\text{(9-b)}$$

Thus, the problem is converted into finding out the transverse field component distribution where it would be required to determine the amplitudes of the transverse modes and the corresponding longitudinal propagation constants which are discussed in Eq. (2). To do this, it is required to formulate the problem as an eigenvalue problem where the amplitudes of the transverse modes correspond to the eigenvectors and the longitudinal propagation constants are the eigenvalues. This can be obtained by inserting the modal expansion of transverse field components in Maxwell's curl equations and weighting the resulting equations with P weighting functions. Based on the Galerkin's method and using the constitutive relations in (7), one can obtain that:

$$\left\langle j\omega D_x, T_{(q)}\right\rangle = \left\langle j\omega\left(\varepsilon_0\varepsilon_r E_x - j\kappa\sqrt{\mu_0\varepsilon_0}H_x\right), T_{(q)}\right\rangle$$
$$= \left\langle\frac{\partial H_z}{\partial y} + \frac{\partial H_y}{\partial z}, T_{(q)}\right\rangle , \quad \text{(10-a)}$$

which can be represented in terms of the modal functions at $z = 0$ as follows:

$$\left\langle j\omega\left(\begin{array}{c}\varepsilon_0\varepsilon_r\sum_p\left[\left(\Phi_{(p)}^{TE} k_{y(p)} + \Phi_{(p)}^{TM} k_{x(p)}\right)T_{(p)}\right]/k_{t(p)} \\ -j\kappa\sqrt{\mu_0\varepsilon_0}\sum_p\left[\left(C_{(p)}^{TE} k_{x(p)} - C_{(p)}^{TM} k_{y(p)}\right)T_{(p)}\right]/k_{t(p)}\end{array}\right), T_{(q)}\right\rangle$$

$$-\left\langle\frac{\partial}{\partial y}\left[\begin{array}{c}-\frac{\varepsilon_r}{\omega\xi\mu_0}\sum_p\Phi_{(p)}^{TE} k_{t(p)} T_{(p)} \\ +j\frac{\kappa}{\omega\xi\sqrt{\mu_0\varepsilon_0}}\sum_p C_{(p)}^{TM} k_{t(p)} T_{(p)}\end{array}\right], T_{(q)}\right\rangle$$

$$= j\beta_{(q)}^{TE} C_{(q)}^{TE} k_{y(q)} / k_{t(q)} + j\beta_{(q)}^{TM} C_{(q)}^{TM} k_{x(q)} / k_{t(q)} , \quad \text{(10-b)}$$

where the inner product is defined as:

$$\left\langle f, g\right\rangle = \int_{-D_y/2}^{D_y/2}\int_{-D_x/2}^{D_x/2} f(x,y)g^*(x,y)dxdy. \quad \text{(10-c)}$$

By following similar steps, one can obtain equations for D_y, B_x, and B_y. By arranging these equations, one can obtain the following eigenvalue problem:

$$\begin{bmatrix} \left[L_{HH}^{TE/TE}\right]_{P\times P} & \left[L_{HH}^{TE/TM}\right]_{P\times P} & \left[L_{HE}^{TE/TE}\right]_{P\times P} & \left[L_{HE}^{TE/TM}\right]_{P\times P} \\ \left[L_{HH}^{TM/TE}\right]_{P\times P} & \left[L_{HH}^{TM/TM}\right]_{P\times P} & \left[L_{HE}^{TM/TE}\right]_{P\times P} & \left[L_{HE}^{TM/TM}\right]_{P\times P} \\ \left[L_{EH}^{TE/TE}\right]_{P\times P} & \left[L_{EH}^{TE/TM}\right]_{P\times P} & \left[L_{EE}^{TE/TE}\right]_{P\times P} & \left[L_{EE}^{TE/TM}\right]_{P\times P} \\ \left[L_{EH}^{TM/TE}\right]_{P\times P} & \left[L_{EH}^{TM/TM}\right]_{P\times P} & \left[L_{EE}^{TM/TE}\right]_{P\times P} & \left[L_{EE}^{TM/TM}\right]_{P\times P} \end{bmatrix} \begin{bmatrix} C^{TE} \\ C^{TM} \\ \Phi^{TE} \\ \Phi^{TM} \end{bmatrix}$$

$$= \begin{bmatrix} \left[j\beta^{TE}\right] & 0 & 0 & 0 \\ 0 & \left[j\beta^{TM}\right] & 0 & 0 \\ 0 & 0 & \left[j\beta^{TE}\right] & 0 \\ 0 & 0 & 0 & \left[j\beta^{TM}\right] \end{bmatrix} \begin{bmatrix} C^{TE} \\ C^{TM} \\ \Phi^{TE} \\ \Phi^{TM} \end{bmatrix}, \qquad (11)$$

where the elements of this eigenvalue problem are presented in Appendix (I). It should be noted that the dimension of this eigenvalue problem is $4P \times 4P$ which introduces $2P$ forward modes and $2P$ backward modes.

B. Mode matching analysis of chiral grating structures

By using the mode matching technique and following the same steps in [15], one can obtain the general scattering matrix between two semi-infinite chiral gratings of the same periodicity and coincide at the plane z=0 as follows:

$$\mathbf{S} = \left(\mathbf{B}^T\right)^{-1}\mathbf{A}$$

$$= \begin{bmatrix} \begin{bmatrix} \left[S_{11}^{TE/TE}\right] & \left[S_{11}^{TE/TM}\right] \\ \left[S_{11}^{TM/TE}\right] & \left[S_{11}^{TM/TM}\right] \end{bmatrix} & \begin{bmatrix} \left[S_{12}^{TE/TE}\right] & \left[S_{12}^{TE/TM}\right] \\ \left[S_{12}^{TM/TE}\right] & \left[S_{12}^{TM/TM}\right] \end{bmatrix} \\ \begin{bmatrix} \left[S_{21}^{TE/TE}\right] & \left[S_{21}^{TE/TM}\right] \\ \left[S_{21}^{TM/TE}\right] & \left[S_{21}^{TM/TM}\right] \end{bmatrix} & \begin{bmatrix} \left[S_{22}^{TE/TE}\right] & \left[S_{22}^{TE/TM}\right] \\ \left[S_{11}^{TM/TE}\right] & \left[S_{22}^{TM/TM}\right] \end{bmatrix} \end{bmatrix}, \quad (12)$$

where

$$\mathbf{A} = \begin{bmatrix} \left[\Phi_a^{TE}\right]^T & \left[\Phi_a^{TM}\right]^T & \left[C_a^{TE}\right]^T & \left[C_a^{TM}\right]^T \\ \left[-\Phi_a'^{TE}\right]^T & \left[-\Phi_a'^{TM}\right]^T & \left[-C_a'^{TE}\right]^T & \left[-C_a'^{TM}\right]^T \end{bmatrix},$$

(13-a)

$$\mathbf{B} = \begin{bmatrix} \left[-\Phi_b'^{TE}\right]^T & \left[-\Phi_b'^{TM}\right]^T & \left[-C_b^{TE}\right]^T & \left[-C_b'^{TM}\right]^T \\ \left[\Phi_b^{TE}\right]^T & \left[\Phi_b^{TM}\right]^T & \left[C_b^{TE}\right]^T & \left[C_b^{TM}\right]^T \end{bmatrix}.$$

(13-b)

The suffixes a and b in (13) correspond to the upper and the lower grating, respectively. The primed terms correspond to the backward propagating modes while the terms without a prime correspond to forward propagating modes. For a special case where the upper limit is free space, the parameters of the upper grating structure are $\varepsilon_{rb}=\varepsilon_{ri}=1$, $\mu_{rb}=\mu_{ri}=1$ and $\kappa_{rb}=\kappa_{ri}=1$.

For the case of a finite-thickness chiral grating slab of thickness h, the total reflection and transmission coefficients can be obtained in terms of generalized scattering matrices as follows [5]:

$$\left[\widetilde{R}_{11}\right] = \left[S_{11}\right]$$
$$+ \left[S_{12}\right]\left(I - \left[\Lambda\right]\left[S_{22}\right]\left[\Lambda'\right]\left[S_{22}\right]\right)^{-1}\left[\Lambda'\right]\left[S_{22}\right]\left[\Lambda\right]\left[S_{21}\right], \quad (14\text{-a})$$

$$\left[\widetilde{T}_{12}\right] = \left[S_{12}\right]\left(I - \left[\Lambda\right]\left[S_{22}\right]\left[\Lambda'\right]\left[S_{22}\right]\right)^{-1}\left[\Lambda\right]\left[S_{21}\right], \quad (14\text{-b})$$

where

$$\left[S_{ij}\right] = \begin{bmatrix} \left[S_{ij}^{TE/TE}\right] & \left[S_{ij}^{TE/TM}\right] \\ \left[S_{ij}^{TM/TE}\right] & \left[S_{ij}^{TM/TM}\right] \end{bmatrix}, \qquad (15\text{-a})$$

which corresponds to the generalized scattering matrices of the semi-infinite chiral grating in (11) where the upper medium is free space. On the other hand $\left[\Lambda\right]$ and $\left[\Lambda'\right]$ correspond to the forward and backward phase delay matrices as follows:

$$\left[\Lambda\right] = \begin{bmatrix} \left[\exp\left(-j\beta^{TE}h\right)\right] & 0 \\ 0 & \left[\exp\left(-j\beta^{TM}h\right)\right] \end{bmatrix}, \quad (15\text{-b})$$

$$\left[\Lambda'\right] = \begin{bmatrix} \left[\exp\left(-j\beta'^{TE}h\right)\right] & 0 \\ 0 & \left[\exp\left(-j\beta'^{TM}h\right)\right] \end{bmatrix}. \quad (15\text{-c})$$

Finally, I in (14) corresponds to a unit matrix of dimension $2P \times 2P$.

The reflection and transmission matrices of Eq. (14) represent the reflection and transmission of P TE and P TM modes and the interaction between them. Specular reflection and transmission coefficients can be obtained by selecting the corresponding terms in the generalized reflection and transmission matrices of (14). Thus the specular TE reflection coefficient due to the TE incident wave is obtained as $R_{11}^{TE/TE} = \widetilde{R}_{11}[p_{00}][p_{00}]$ where $p=p_{00}$ corresponds to the Floquet mode $m=0$ and $n=0$ as discussed earlier. On the other hand the specular TE reflection coefficient due to the TM incident wave is obtained as $R_{11}^{TE/TM} = \widetilde{R}_{11}[p_{00}][p_{00}+P]$. Similarly, the specular TM reflection coefficients due to TE and TM incident waves are obtained as $R_{11}^{TM/TE} = \widetilde{R}_{11}[p_{00}+P][p_{00}]$ and $R_{11}^{TM/TM} = \widetilde{R}_{11}[p_{00}+P][p_{00}+P]$, respectively. In a similar way, one can obtain the sepcular transmission coefficients as $T_{12}^{TE/TE} = \widetilde{T}_{12}[p_{00}][p_{00}]$, $T_{12}^{TE/TM} = \widetilde{T}_{12}[p_{00}][p_{00}+P]$, $T_{12}^{TM/TE} = \widetilde{T}_{12}[p_{00}+P][p_{00}]$, and $T_{12}^{TM/TM} = \widetilde{T}_{12}[p_{00}+P][p_{00}+P]$. It should be noted that these coefficients correspond to the complex reflection and transmission coefficients of the electric field components. The corresponding power reflection and transmission coefficients are

obtained as the square value of the amplitudes of these electric field coefficients. For the sake of comparison with the available previously published results, we present the results of power reflection and transmission coefficients as it is discussed in the following section.

III. RESULTS AND DISCUSSIONS

In this section, we present sample results to verify the present analysis. It should be noted that the present method represents a general form for the cases of dielectric and magneto-dielectric grating slabs by setting the chirality coefficients in both the base substrate and the implanted rods to be zero. This method can also be used for both one-dimensional and two-dimensional grating. For the case of one-dimensional grating, the length of the implanted rod in one direction is extended to be the same as the periodic distance in this direction. For the space limit, we did not show comparisons with previously published results of dielectric grating and magneto-dielectric grating. However, we obtained excellent agreement with these results.

It should be noted that the presented results are based on normalized dimensions with respect to the operating wavelength. Thus, these results are not limited for a certain frequency. The present analysis has no lower limit on the normalized dimensions. However, for the case of a chiral grating slab with a quite small periodic cell compared with the operating wavelength, we obtained reflection and transmission coefficients which are nearly the same as the corresponding ones of a homogenous chiral slab having electrical properties equivalent to the average properties of the host and inclusion as discussed in [4]. This average in the present case is obtained based on the ratio of the dimensions of both the inclusion and the host in the unit cell. This property has been quite clarified in [4], thus these results are not repeated here. On the other hand, the upper limit of the normalized dimensions of the cells is kept below unity to avoid the presence of higher order propagating Floquet modes in air-side as discussed in [4].

For the case of a one-dimensional chiral grating slab, we present a sample result for comparison with the published results of Wu and Jaggard [4]. In this case, the parameters of the

base and inclusion are $\varepsilon_{rb} = 2.5, \mu_{rb} = 1, \kappa_b = 0.1$ and $\varepsilon_{r1} = 1.5, \mu_{r1} = 1, \kappa_1 = 0.1$, respectively. The periodic cell is square and is related to the grating thickness as $D_x = D_y = h/1.713$. The dimensions of the implanted rod inside the cell are $L_x = D_x/2$ and $L_y = D_y$. The incident plane wave is assumed to be the TE wave of incidence angle $\theta_{inc} = 45°$, $\phi_{inc} = 0°$. Figure 2 shows the specular reflection and transmission coefficients in this case for both the co-polarized and cross-polarized components as functions of normalized grating thickness where $k_0 = 2\pi/\lambda_0$ corresponds to the free space wave number. By comparing this figure with the corresponding results in [4], one obtains an excellent agreement.

In this paper, we extend the previous case to be a two-dimensional chiral grating by setting $L_y = D_y/2$. We also changed the permeability of the base to be $\mu_{rb} = 1.4$. The remaining parameters are the same as in Fig. 2. We studied both TE and TM cases as shown in Figure 3 and 4. It can be noted that the polarization conversion in the reflected field is greater at resonance frequencies in the case of TE incident wave than the case of TM incident wave.
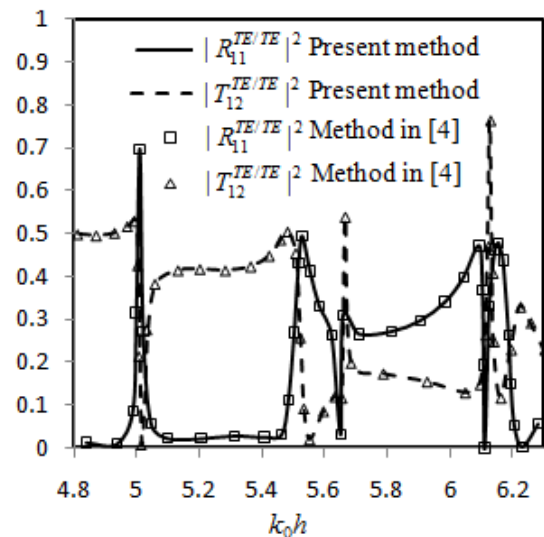
(a) TE reflection and transmission coefficients due to TE incident wave.
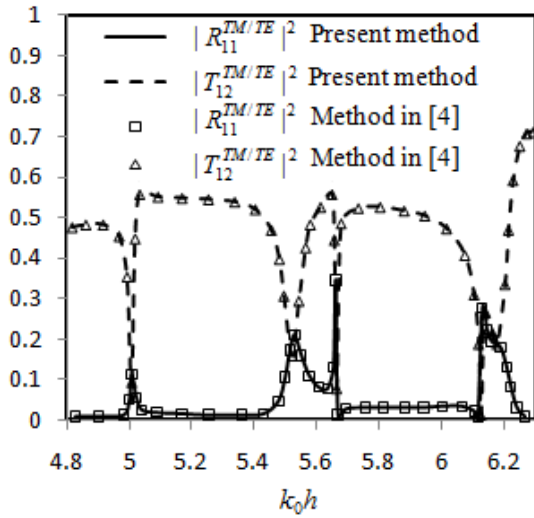
(b) TM reflection and transmission coefficients due to TE incident wave.

Fig. 2. Specular power reflection and transmission coefficients due to an obliquely incident TE plane wave on a chiral grating slab. $\theta_{inc} = 45°$, $\phi_{inc} = 0°$, $\varepsilon_{rb} = 2.5$, $\mu_{rb} = 1$, $\kappa_b = 0.1$, $\varepsilon_{r1} = 1.5$, $\mu_{r1} = 1$, $\kappa_1 = 0.1$, $D_x = D_y = h/1.713$, $L_x = D_x/2$ and $L_y = D_y$.
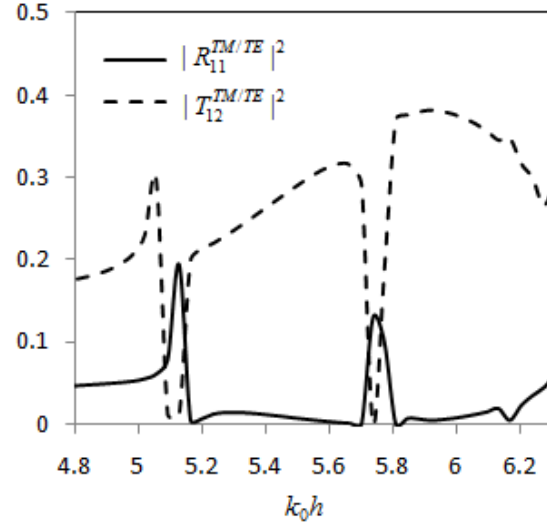
(b) TM reflection and transmission coefficients due to TE incident wave.

Fig. 3. Specular power reflection and transmission coefficients due to an obliquely incident TE plane wave on a chiral grating slab. $\theta_{inc} = 45°$, $\phi_{inc} = 0°$, $\varepsilon_{rb} = 2.5$, $\mu_{rb} = 1.4$, $\kappa_b = 0.1$, $\varepsilon_{r1} = 1.5$, $\mu_{r1} = 1$, $\kappa_1 = 0.1$, $D_x = D_y = h/1.713$, $L_x = D_x/2$ and $L_y = D_y/2$.
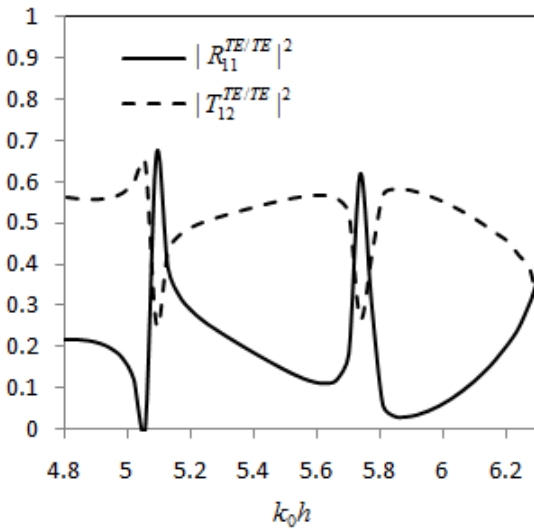
(a) TE reflection and transmission coefficients due to TE incident wave.
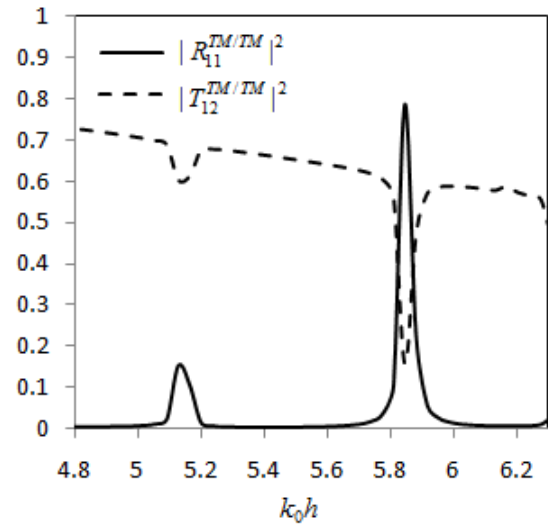
(a) TM reflection and transmission coefficients due to TM incident wave.
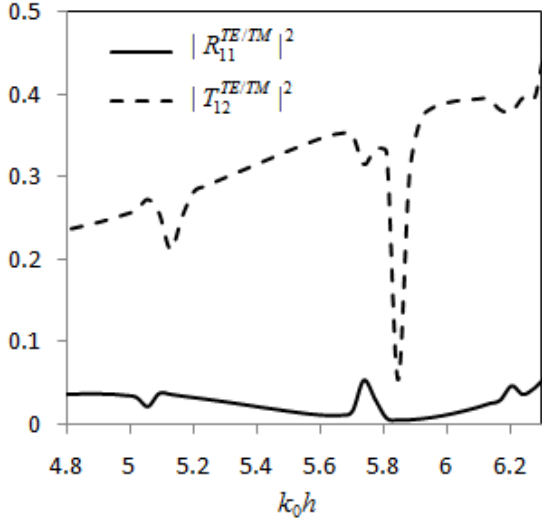
(b) TE reflection and transmission coefficients due to TM incident wave.
Fig. 4. Specular power reflection and transmission coefficients due to an obliquely incident TM plane wave on a chiral grating slab for the same parameters of Fig. 3.

IV. CONCLUSION

Chiral grating can be used to control both the magnitude and polarization of the reflected and transmitted fields. In this paper, we presented detailed modal analysis of two-dimensional chiral grating. This modal analysis is combined with mode matching technique and generalized matrix method to study the reflection and transmission due to a finite thickness two-dimensional chiral grating slab. The present analysis represents a generalization for previously studied cases including dielectric grating, magneto-dielectric grating and one-dimensional chiral grating.

APPENDIX (I)

The details of the elements of the eigenvalue problem in Eq. (11) are presented in this Appendix. These elements are obtained as:

$$l_{HH(q)(p)}^{TE/TE} = l_{EE(q)(p)}^{TM/TM} =$$
$$= \frac{k_0\left(k_{x(p)}k_{y(q)} - k_{y(p)}k_{x(q)}\right)}{k_{t(p)}k_{t(q)}}\left\langle \kappa T_{(p)}, T_{(q)} \right\rangle. \quad (A-1)$$

$$l_{HH(q)(p)}^{TE/TM} = -l_{EE(q)(p)}^{TM/TE} =$$
$$= -\frac{k_0\left(k_{x(p)}k_{x(q)} + k_{y(p)}k_{y(q)}\right)}{k_{t(p)}k_{t(q)}}\left\langle \kappa T_{(p)}, T_{(q)} \right\rangle$$

$$- j\frac{k_{y(q)}k_{t(p)}}{k_0 k_{t(q)}}\left\langle \frac{\partial}{\partial y}\left(\frac{\kappa}{\xi}T_{(p)}\right), T_{(q)} \right\rangle$$
$$- j\frac{k_{x(q)}k_{t(p)}}{k_0 k_{t(q)}}\left\langle \frac{\partial}{\partial x}\left(\frac{\kappa}{\xi}T_{(p)}\right), T_{(q)} \right\rangle. \quad (A-2)$$

$$l_{HE(q)(p)}^{TE/TE} = \frac{jk_0\left(k_{x(p)}k_{x(q)} + k_{y(p)}k_{y(q)}\right)}{Z_0 k_{t(p)}k_{t(q)}}\left\langle \varepsilon_r T_{(p)}, T_{(q)} \right\rangle$$

$$+ \frac{k_{x(q)}k_{t(p)}}{k_0 Z_0 k_{t(q)}}\left\langle \frac{\partial}{\partial x}\left(\frac{\varepsilon_r}{\xi}T_{(p)}\right), T_{(q)} \right\rangle$$

$$+ \frac{k_{y(q)}k_{t(p)}}{k_0 Z_0 k_{t(q)}}\left\langle \frac{\partial}{\partial y}\left(\frac{\varepsilon_r}{\xi}T_{(p)}\right), T_{(q)} \right\rangle. \quad (A-3)$$

$$l_{HE(q)(p)}^{TE/TM} = \frac{jk_0\left(k_{x(p)}k_{y(q)} - k_{y(p)}k_{x(q)}\right)}{Z_0 k_{t(p)}k_{t(q)}}\left\langle \varepsilon_r T_{(p)}, T_{(q)} \right\rangle. (A-4)$$

$$l_{HH(q)(p)}^{TM/TE} = -l_{EE(q)(p)}^{TE/TM}$$
$$= \frac{k_0\left(k_{x(p)}k_{x(q)} + k_{y(p)}k_{y(q)}\right)}{k_{t(p)}k_{t(q)}}\left\langle \kappa T_{(p)}, T_{(q)} \right\rangle. \quad (A-5)$$

$$l_{HH(q)(p)}^{TM/TM} = l_{EE(q)(p)}^{TE/TE}$$
$$= -\frac{k_0\left(k_{y(p)}k_{x(q)} - k_{x(p)}k_{y(q)}\right)}{k_{t(p)}k_{t(q)}}\left\langle \kappa T_{(p)}, T_{(q)} \right\rangle$$

$$- j\frac{k_{x(q)}k_{t(p)}}{k_0 k_{t(q)}}\left\langle \frac{\partial}{\partial y}\left(\frac{\kappa}{\xi}T_{(p)}\right), T_{(q)} \right\rangle$$
$$+ j\frac{k_{y(q)}k_{t(p)}}{k_0 k_{t(q)}}\left\langle \frac{\partial}{\partial x}\left(\frac{\kappa}{\xi}T_{(p)}\right), T_{(q)} \right\rangle. \quad (A-6)$$

$$l_{HE(q)(p)}^{TM/TE} = \frac{jk_0\left(k_{y(p)}k_{x(q)} - k_{x(p)}k_{y(q)}\right)}{Z_0 k_{t(p)}k_{t(q)}}\left\langle \varepsilon_r T_{(p)}, T_{(q)} \right\rangle$$

$$+ \frac{k_{x(q)}k_{t(p)}}{k_0 Z_0 k_{t(q)}}\left\langle \frac{\partial}{\partial y}\left(\frac{\varepsilon_r}{\xi}T_{(p)}\right), T_{(q)} \right\rangle$$

$$- \frac{k_{y(q)}k_{t(p)}}{k_0 Z_0 k_{t(q)}}\left\langle \frac{\partial}{\partial x}\left(\frac{\varepsilon_r}{\xi}T_{(p)}\right), T_{(q)} \right\rangle. \quad (A-7)$$

$$l_{HE(q)(p)}^{TM/TM} = \frac{jk_0\left(k_{x(p)}k_{x(q)} + k_{y(p)}k_{y(q)}\right)}{Z_0 k_{t(p)}k_{t(q)}}\left\langle \varepsilon_r T_{(p)}, T_{(q)} \right\rangle. \quad (A-8)$$

$$l_{EH(q)(p)}^{TE/TE} = \frac{jk_0 Z_0\left(k_{x(p)}k_{x(q)} + k_{y(p)}k_{y(q)}\right)}{k_{t(p)}k_{t(q)}}\left\langle \mu_r T_{(p)}, T_{(q)} \right\rangle. \quad (A-9)$$

$$l_{EH(q)(p)}^{TE/TM} = jk_0 Z_0 \frac{\left(k_{x(p)}k_{y(q)} - k_{y(p)}k_{x(q)}\right)}{k_{t(p)}k_{t(q)}} \left\langle \mu_r T_{(p)}, T_{(q)} \right\rangle$$

$$+ \frac{Z_0 k_{t(p)} k_{y(q)}}{k_0 k_{t(q)}} \left\langle \frac{\partial}{\partial x}\left(\frac{\mu_r}{\xi} T_{(p)}\right), T_{(q)} \right\rangle$$

$$- \frac{Z_0 k_{t(p)} k_{x(q)}}{k_0 k_{t(q)}} \left\langle \frac{\partial}{\partial y}\left(\frac{\mu_r}{\xi} T_{(p)}\right), T_{(q)} \right\rangle . \qquad \text{(A-10)}$$

$$l_{EH(q)(p)}^{TM/TE} = \frac{jk_0 Z_0 \left(k_{y(p)}k_{x(q)} - k_{x(p)}k_{y(q)}\right)}{k_{t(p)}k_{t(q)}} \left\langle \mu_r T_{(p)}, T_{(q)} \right\rangle . \qquad \text{(A-11)}$$

$$l_{EH(q)(p)}^{TM/TM} = jk_0 Z_0 \frac{\left(k_{x(p)}k_{x(q)} + k_{y(p)}k_{y(q)}\right)}{k_{t(p)}k_{t(q)}} \left\langle \mu_r T_{(p)}, T_{(q)} \right\rangle$$

$$+ \frac{Z_0 k_{t(p)} k_{x(q)}}{k_0 k_{t(q)}} \left\langle \frac{\partial}{\partial x}\left(\frac{\mu_r}{\xi} T_{(p)}\right), T_{(q)} \right\rangle$$

$$+ \frac{Z_0 k_{t(p)} k_{y(q)}}{k_0 k_{t(q)}} \left\langle \frac{\partial}{\partial y}\left(\frac{\mu_r}{\xi} T_{(p)}\right), T_{(q)} \right\rangle . \qquad \text{(A-12)}$$

For the special case where the unit cell and implanted rod are of rectangular shapes as shown in Fig. 1, the above inner products can be obtained analytically in closed forms as discussed in [6].

REFERENCES

[1] V. R. Tuz and C.W. Qiu, "Semi-Infinite Chiral Nihility Photonics: Parametric Dependence, Wave Tunneling and Rejection," *Progress In Electromagnetics Research,* vol. PIER 103, pp. 139-152, 2010.

[2] D. L. Jaggard, N. Engheta, M. W. Kowarz, P. Pelet, J. C. Liu, and Y. Kim, "Periodic Chiral Structures," *IEEE Trans. Antennas Propagat.*, vol. AP-37, pp. 1447–1452, 1989.

[3] L. G. Zheng and W. X. Zhang, "Analysis of Bi-Anisotropic PBG Structure using Plane Wave Expansion Method," *Progress In Electromagnetics Research,* vol. PIER 42, pp. 233–246, 2003.

[4] T. X. Wu and D. L. Jaggard, "Scattering of Chiral Periodic Structure," *IEEE Trans. Antennas Propagat.*, vol. AP-52, pp. 1859-1870, 2004.

[5] A. M. Attiya and A. A. Kishk, "Modal Analysis of a Two-Dimensional Dielectric Grating Slab Excited by an Obliquely Incident Plane Wave," *Progress In Electromagnetics Research,* vol. PIER 60, pp. 221–243, 2006.

[6] A. M . Attiya, A. A. Kishk, and A. W. Glisson, "Analysis of Two-Dimensional Magneto-Dielectric Grating Slab," *Progress In Electromagnetics Research,* vol. PIER 74, pp.195–216, 2007.

[7] A. Lakhtakia, "On a Fourth-Order Wave Equation for EM Propagation in Chiral Media," *Appl. Phys.* B, vol. 36, pp.163-165, 1985.

[8] A. Gomez, I. Barba, A. C. L. Cabeceira, J. Represa, A. Vegas, and M. A. Solano, "Electromagnetic Propagation in Unbounded Inhomogeneous Chiral Media using the Coupled Mode Method," *Microwave Opt.Technol. Lett.* vol. 49, pp. 2771-2779, 2007.

[9] A. Gomez, A. Vegas, and M. A. Solano, "On Two Different Formulations of the Coupled Mode Method: Application to 3D Rectangular Chirowaveguides," *Int. J. Electron. Commun.* vol. (AEU) 60, pp. 690–704, 2006.

[10] A. Gomez, A. Lakhtakia, A. Vegas, and M. A. Solano, "Hybrid Technique for Analysing Metallic Waveguides Containing Isotropic Chiral Materials," *IET Microw. Antennas Propag.*, vol. 4, pp. 305–315, 2010.

[11] T. X. Wu and D. L. Jaggard, "A Comprehensive Study of Discontinuities in Chirowaveguides," *IEEE Trans. Microw. Theory Tech.*, vol. MTT-50, pp. 2320–2330, 2002.

[12] J. Pitarch, J. M. Catal-Civera, F. L. Pen Aranada-Foix, and M. A. Solano, "Efficient Modal Analysis of Bianisotropic Waveguides by the Coupled Mode Method," *IEEE Trans. Microwave Theory Tech.*, vol. MTT-55, pp. 108–116, 2007.

[13] A. Gomez , A. Lahktakia, and J. Magineda "Full-Wave Hybrid Technique for 3D Isotropic-Chiral-Material Discontinuities in Rectangular Waveguides: Theory and Experiment," *IEEE Trans. Microwave Theory Tech.*, vol. MTT-56, pp. 2815–2825, 2008.

[14] S. T. Imeci, F. Altunkilic, J. R. Mautz, and E. Arvas, "Transmission Through an Arbitrarily Shaped Aperture in a Conducting Plane Separating Air and a Chiral Medium," *Applied Computational Electromagnetic Society (ACES) Journal*, vol.25, pp. 587–599, July 2010.

[15] M. A. Solano, A. Vegas, and A. Prieto, "Numerical Analysis of Discontinuities in a Rectangular Waveguide Loaded with Isotropic or Anisotropic Obstacles by Means of the Coupled-Mode Method and the Mode-Matching Method," *Int. J. Numer. Model.:*

Electron. Netw. Dev. Fields, vol. 7, pp. 433–452, 1994.

Ahmed M. Attiya graduated from Zagazig University of Egypt in 1991 and received the M.Sc. and Ph.D. in Electronics and Electrical Communications from Cairo University in 1996 and 2001, respectively. Attiya is an Associate Prof. in the Microwave Engineering Dept. Electronics Research Institute. In 2002-2004, he was a research fellow in Virginia Polytechnic Inst. and State Univ. In 2004-2005, he was a visiting scholar in University of Mississippi. His research interest includes antennas, electromagnetic wave propagation, scattering and diffraction problems, and numerical techniques in electromagnetics.

A Novel Band-Stop Filter using Octagonal-Shaped Patterned Ground Structures along with Interdigital and Compensated Capacitors

Ahmed Boutejdar [1], Mouloud Challal [2], and Arab Azrar [2]

[1] Chair of Microwave and Communication Engineering
University of Magdeburg, Magdeburg, 39106, Germany
Ahmed.Boutejdar@ovgu.de

[2] Department of Electronic, IGEE
University of Boumerdes, Boumerdes, 35000, Algeria
mchallal@umbb.dz

Abstract — This paper presents a novel compact microstrip band-stop filter (BSF) based on octagonal defected ground structure (DGS) along with interdigital and compensated capacitors. The proposed BSF has lower and higher cut-off frequencies of 3.4 GHz and 5.3 GHz, respectively. A comparison between simulation and measurement results confirms the validity of the BSF configuration and the design procedure. The compact filter occupies an area of ($0.45\lambda g \times 0.35\lambda g$) with $\lambda g = 0.044$ m on an $\varepsilon_r = 3.66$ substrate and shows a 44% bandwidth ($\approx$ 2GHz) and a return loss of 0.1 dB. The experimental results show the excellent agreement with theoretical simulation results.

Index Terms — Band-stop filter (BSF), compensated capacitor defected, ground structure (DGS), interdigital capacitor (IDC).

I. INTRODUCTION

The main design goals of filters are focused on compact and high performance in which they are generally required to reduce the cost and improve system performance. In recent years, defected ground structures (DGS) have been presented in a variety of different versions for filter applications [1, 6] and they are applied widely to design the microwave and millimeter wave circuits. Therefore, various DGSs have been proposed and applied for suppression of spurious harmonics in filters response and also for amplifiers and antennas [6-9].

In this paper, a new microstrip band-stop DGS filter with two slotted octagonal including interdigital capacitors (IDC) ground structure using slow wave effect, electromagnetic coupling is presented. A good sharp cutoff frequency response and a good performance in both the pass and the stop bands have been obtained. The proposed filter is fabricated and measured. The use of the idea of multiple capacitors led to a simple way to control the resonant frequency of the filter, while the distance between the two neighboring DGS resonators is used to improve the filter response. All structures are designed and analyzed using IE3D, a commercial electromagnetic simulator based on an integral equation method and the method of moment.

The measurement results were in good agreement with the simulation results.

II. CHARACTERISTICS OF THE OCTAGONAL SLOT DGS WITH AND WITHOUT INTERDIGITAL CAPACITOR

The configuration of the 0° octagonal-slot DGS without IDC is shown in Fig. 1. It is composed of an open ring on the ground plane and a microstrip line on the top layer. The zero degree

(0°) indicates that the open ring is in parallel with the microstrip line. The substrate with 0.254 mm thickness and a dielectric constant of 3.66 is used for all simulations. The conductor strip of the microstrip line (50 Ω) on the top plane has a calculated width 'W' of 0.55 mm.

Figure 2 shows the resonance and the cut-off frequencies versus the length 'l' of an octagonal slot DGS without IDC. It can be observed that both frequencies decrease with the increase of the length 'l'. The L and C of modelled Parallel LC circuit as shown in Fig. 2 are given by:

$$C = \frac{5 f_c}{\pi Z_0 \left(f_0^2 - f_c^2\right)} \quad \& \quad L = \frac{250}{C_p (\pi f_0)^2}. \quad (1)$$
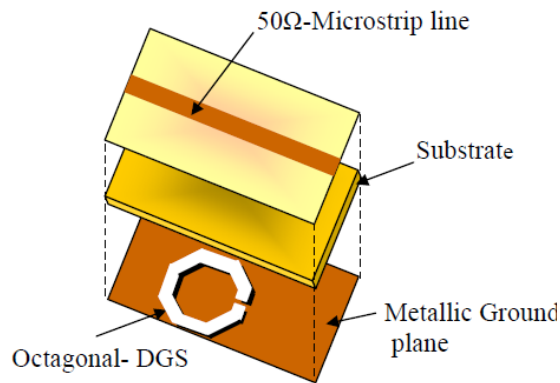
Fig. 1. The 3D view of the 0° octagonal-slot on the ground plane.

The values of the cut-off frequency fc and the resonance frequency fc can be found from the transmission characteristics of the octagonal slot [7, 8] as shown in Fig. 2.
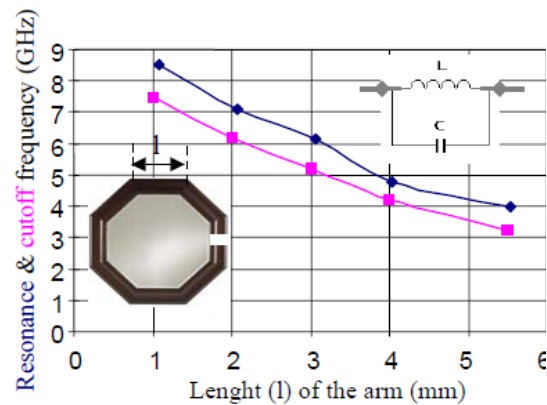
Fig. 2. Resonance and cut-off frequencies versus length 'l' of an octagonal slot DGS without IDC.

III. FIELD DISTRIBUTION ALONG OF THE DGS-UNIT

The objective of this short investigation is to verify the dependence of the equivalent circuit elements (capacitance and inductance) on the surface as the distribution electromagnetic field. The simulation results are shown in Fig. 3(a) and Fig. 3(b). The microstrip structure is divided into two regions. In region I the electric field is highly concentrated in the gap, hence any change in dimensions of the gap affects the effective capacitance of the structure. In region II the electric field nearly vanishes [9-11]. On the other hand, the current is distributed throughout the whole structure. Therefore, any change in the length of the U-arm strongly affects the magnetic field distribution and hence the surface current, which in turn leads to a change in the effective inductance of the structure. Therefore, that region I corresponds to a capacitance and region II corresponds to an inductance. The full structure corresponds then to an LC-resonator.
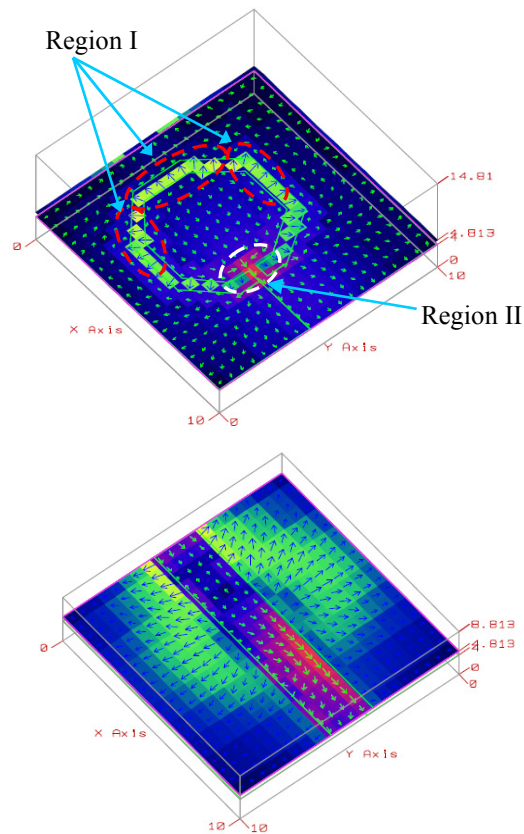
Fig. 3. EM field distribution at the resonance frequency, (a) EM field on bottom layer, (b) EM field on top layer.

IV. BAND STOP FILTER USING AN OCTAGONAL OPEN-RING INCLUDING IDCS

A schematic 3D view of the 90° octagonal DGS-band-stop filter (BSF) is shown in Fig. 4 with only one IDC [7, 8]. It is composed of an open-ring including IDCs in the metallic ground plane and a microstrip line on the top layer. The ninety degrees (90°) indicates that the open ring DGS is perpendicular to the microstrip line. In order to control the stopband, a simple idea is to add two IDCs in both sides as shown in Fig. 4.
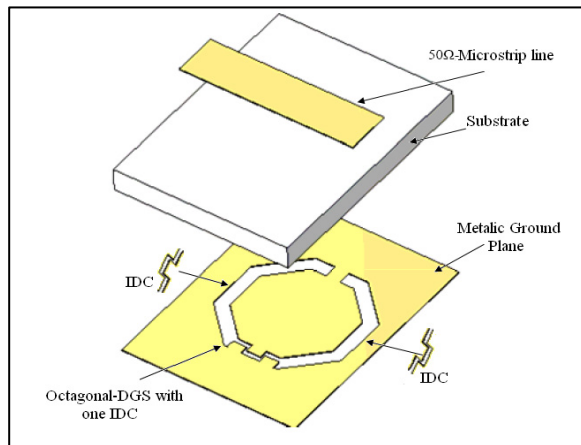
Fig. 4. The 3D view of the 90° octagonal-slot on the ground plane with IDC.

Figure 5 shows EM simulation results for the 90° octagonal slot with and without IDC on the ground plane of the microstrip line. As can be seen, when IDCs are included, the attenuation pole (f_0) of S_{21} response is shifted to low frequencies, i.e, from 5 GHz to 4.3 GHz. Moreover, the cutoff frequency (fc) depends also on the added IDCs, i.e, it decreased from 4.5 GHz to 3.9 GHz.

V. DESIGN OF THE PROPOSED BAND STOP FILTER

As in previous work [6], a DGS-resonator with an octagonal form has been used in order to improve the EM coupling between the neighboring DGS elements, and therefore, the enhancement for both the reject band and the compactness of the structure. The integration of an interdigital capacitor leads to control of the transmission zero of this filter. The using of multi-interdigital

capacitors caused a creasing of the capacitance and this leads to a shifting of the transmission zero in the lower frequencies range, which means more compactness, as demonstrated in our work. Based on this idea, tunable compact band-pass/band-stop filters using varactor devices could be easy to im____.
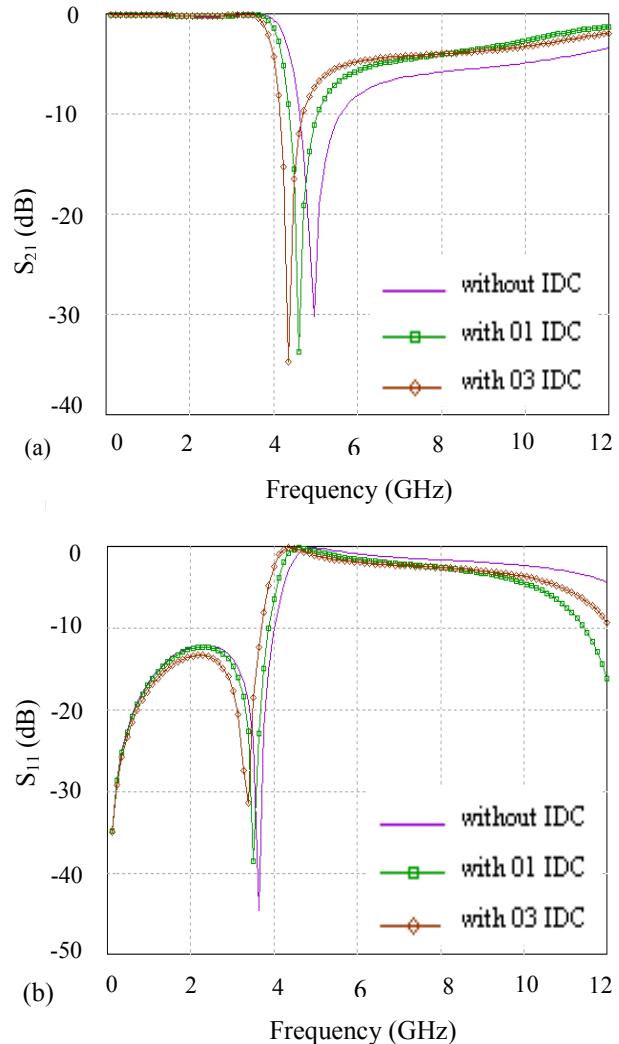
Fig. 5. EM simulation results for the 90° octagonal slot DGS with and without IDC (a) insertion loss (S_{21}) in dB and, (b) return loss (S_{11}) in dB.

A new band-stop filter is proposed and shown in Fig. 6. Different parameters of the proposed BSF are investigated and the best obtained ones are described in this section.

Figure 7 shows the simulation results of the BSF for various values of the parameter 'd' while the others are fixed to w = 0.8 mm, L = 3.5 mm

and w_0 = 1.9 mm. It is observed that the BSF shows a good rejection which is greater than -18 dB in the stop band.

When d equals to 0.2 mm, the second harmonic has a level of around -18 dB which is well rejected [15-17].
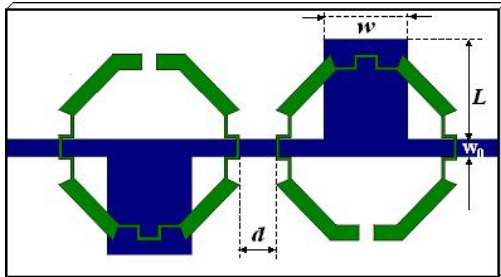
Fig. 6. The layout of the proposed band-stop filter.

(a)

(b)
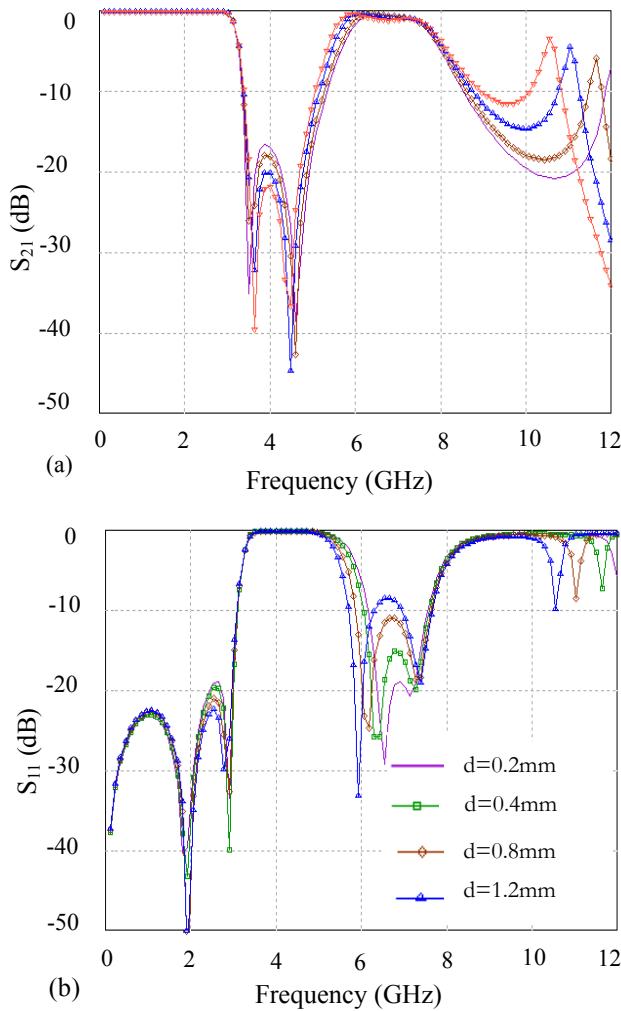
Fig. 7. Simulated S-parameters of the proposed band-stop filter for various d, (a) insertion loss (S_{21}) in dB and, (b) return loss (S_{11}) in dB.

VI. FABRICATION AND MEASUREMENT

Good performances have been obtained when the parameters d, w and L equal, respectively, to 0.2 mm, 0.8 mm, and 3.5 mm. Also, symmetry of the filter response has been achieved as shown in Fig. 7(b).

The proposed BSF with two octagonal DGSs including six IDCs in the metallic ground plane and microstrip capacitances on the top layer has been fabricated as shown in Fig. 8; whereas, the measured and the simulated results are shown in Fig. 9.

From Fig. 9, it can be seen that the fabricated BSF has an insertion loss less than 0.2 dB in the stop-band. The attenuation characteristic shows more than 20 dB in both pass-bands. The use of the IDCs lead to a compact size of this new filter and provides sharp rejection due to the reflection zeros near the stop-band edge. The small deviations between the simulated and measured results were caused by the SMA connectors and manufacturing errors. The performance of this novel BSF is experimentally characterized and compared with its simulation results which show a good agreement.

VII. CONCLUSION

This letter, a new octagonal DGS band-stop filter (BSF) has been introduced and investigated. It has been shown that the proposed filter has a good sharp cutoff frequency response and a good performance in both the pass-band and the stop-band. The use of the interdigital capacitor (IDC) idea improves the pass bands of the filter as compared to the filter without IDC and has also facilitated the control of the resonant frequency without using any extra devices and consequently, the structure has became very compact. A comparison between simulation and measurement results confirms the validity of the BSF configuration and the design procedure. In order to define the ideal coupling distance between the DGS-resonators, an empirical method has been used in this work.
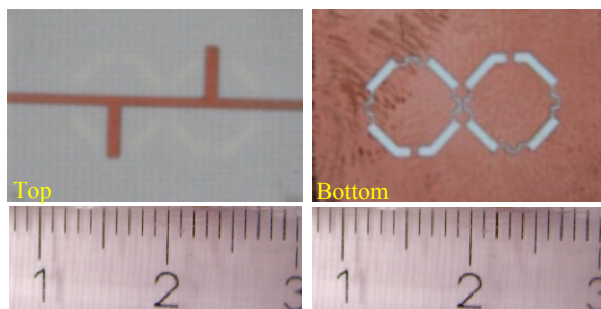
Fig. 8. The photography of the fabricated Band-Stop filter.
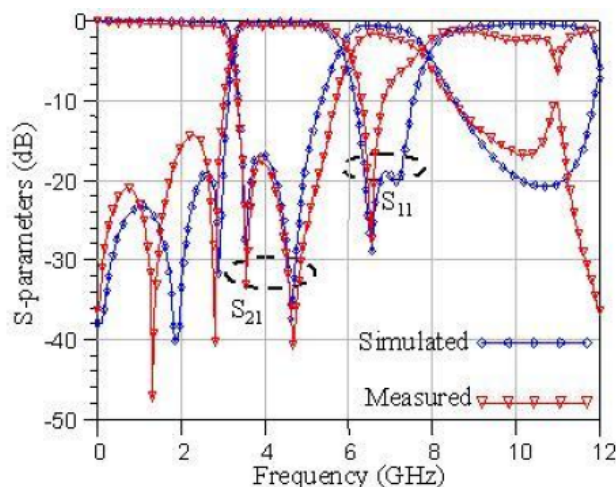
Fig. 9. Measured and simulated S-parameters of the proposed band-stop filter.

ACKNOWLEDGMENT

REFERENCES

[1] R. N. Baral and P. K. Singhal, "Design and Analysis of Microstrip Photonic Band Gap Filter for Suppression of Periodicity," *Applied Computational Electromagnetic Society (ACES) Journal*, vol. 25, no. 2, February 2010.

[2] A. Dal, J. S. Park, C. S. Kim, J. Kim,Y, and T. Itoh, "A Design of the Low-Pass Filter using the Novel Microstrip Defected Ground Structure," *IEEE Trans. Microw. Theory Tech.*, vol. 49, pp. 86–93, May 2001.

[3] A. Boutejdar, M. Makkey, A. Elsherbini, and A. Omar "Design of Compact Stop-Band Extended Microstrip Low-Pass Filters by Employing Mutual Coupled Square Shaped Defected Ground Structures," *Microw. Opt Technol. Lett*, vol 50, iss. 4, pp. 1107-1111, Apr. 2008.

[4] J.-S. Lim, H.-S. Kim, J.-S. Park, and S. Nam, "A Power Amplifier with Efficiency Improved using Defected Ground Structure," *IEEE Microw. Wireless Compon. Lett*., vol. 11, no. 4, pp. 170–172, Apr. 2001.

[5] H. Liu, Z. Li, and J. Mao, "Harmonic Suppression with Photonic Bandgap and DGS for a Microstrip Patch Antenna," *IEEE Microw. Wireless Compon. Lett.*, vol. 15, no. 2, pp. 55–56, Feb. 2005.

[6] A. Boutejdar, A. Rahman, A. Batmanov, A. Omar, and E. Burte, "Miniaturized Band-Stop Filter Based on Multilayer- Technique and New Coupled Octagonal DGS With Interdigital Capacitor," *Microw. Opt Technol. Lett*, vol. 52, iss. 3, pp. 510-514, Mar. 2010.

[7] C. Kim, J. S. Park, A. Dal, and J. Kim, "A Novel 1-D Periodic Defected Ground Structure for Planar Circuits," *IEEE Microwave Guided Wave Lett.*, vol. 10, pp. 131–133, Apr. 2000.

[8] A. Boutejdar, A. Batmanov, and A. S. Omar, "A Compact Band-Stop/Band Pass Filter using a Narrow Gap Capacitive as J-Inverter and New Octagonal Defected Ground Structure," *3rd European Conference on Antennas and Propagation, EuCAP* 2009, Berlin, Germany, Mar. 2009.

[9] Ahmed Boutejdar; Batmanov, Anatoliy; Omar, Abbas; Burte, and Edmund P., (Book Chapter) "A Miniature 3.1 GHz Microstrip Bandpass Filter with Suppression of Spurious Harmonics using Multilayer Technique and Defected Ground Structure Open-Loop Ring," Ultra-wideband, short-pulse electromagnetics 9. New York, NY: Springer, ISBN 978-0-387-77844-0, S. 191-200, 2010.

[10] A. Abdel-Rahman, A. K. Verma, A. Boutejdar, and A. S. Omar, "Compact Stub Type Microstrip Bandpass Filter using Defected Ground Plane," *IEEE Microwave and Wireless Components Letters*, vol. 14, pp. 136-138, 2004.

[11] M. Al-Sharkawy, A. Boutejdar, F. Alhefnawi, and O. Luxor, " Improvement of Compactness of Lowpass/Bandpass Filter

Using A New Electromagnetic Coupled Crescent Defected Ground Structure (DGS) Resonators," *The Applied Computational Electromagnetics Society (ACES) Journal*, vol. 25, no. 9, July 2010.

[12] J. S. Hong and M. J. Lancaster, Microstrip Filters for RF/Microwave Applications, New York: Wiley, 2001.

[13] A. Boutejdar, A. Batmanov, E. Burte, and A. Omar, " Design of a New Bandpass Filter with Sharp Transition Band Using U-Defected Ground Structure (DGS) and Multilayer-Technique*," IET Microwave, Antennas and Propagation*, vol. 4, no. 9, pp.1415-1420, September 2010.

[14] J. -S. Hong and M. J. Lancaster, "Theory and Experiment of Novel Microstrip Slow-Wave Open-Loop Resonator Filters," *IEEE Trans. Microwave Theory Tech.*, vol. 45, no. 12, pp. 2358-2365, Dec. 1997.

[15] A. Boutejdar, A. Omar, and E. Burte, "Miniaturized Lowpass and Bandstop Filters Using Controlled Coupling of Open-Loop-Ring Defected Ground Structure (DGS)," *Microwave and Optical Technology Letters*, vol. 52, no. 11, November 2010.

[16] J. -S. Hong and M. J. Lancaster, "Cross-Coupled Microstrip Hairpin-Resonator Filters," *IEEE Trans. Microwave Theory Tech.*, vol. 46, no. 1, pp. 118-122, Jan. 1998.

[17] A. Boutejdar, A. Elsherbini, A. Balalem, J. Machac, and A. Omar, "Design of New DGS Hairpain Microstrip Bandpass Filter using Coupling Matrix Method," *PIERS Progress in Electromagnetics Research Symposium*, Prague, Czech Republic, pp. 261-265, August 27 - 30, 2007.

Dr. Ahmed Boutejdar was born in Souk El-Arbaa du Gharb, Marocco. He received the Diplom (Licence) in Mathematics, Physics, and Chemistry from Ibn Tofeil University, Kénitra, Morocco in 1994 and in Technische Hochschule Köthen in 1997. From 1995 to 1997, Preparatory Year of german language and Preparatory Year of Engineering high School in köthen, Germany. B.Sc. and Dipl.-Eng. Degree with summa cum laude in Electrical Engineering, Communication, and Microwave Engineering from Otto-von-Guericke University of Magdeburg, Germany in 2002 and 2004, respectively and he received his Ph.D. degree with summa cum laude in 2010 from the Department of Communication and High Frequency-Technique from the University of Magdeburg. He is currently working on a research project on " Entwurf, Optimierung, CMOS-kompatible Herstellung und Charakterisierung von abstimmbaren planaren und koplanaren MEMS DGS-Filtern", which is one part of his Ph.D. thesis. His research interests include the design and analysis of microstrip filters, defected ground structures behaviours, fractal DGS-filters, UWB-DGS-filters and tunable DGS-filters using MEMS-technology.

Dr. Boutejdar has authored over 100 papers in international journals and proceedings of international and national symposia and a book-chapter in "Ultra-Wideband, Short Pulse Electromagnetics 9" Springer 2010. He is reviewer of the IEEE Microwave and Wireless Components Letters (*MWCL*), the Hindawi Publishing Corporation/International Journal of Microwave science and Technology (*IJMST*), the Journal of Microwaves, Optoelectronics and Electromagnetic Applications (*JMOe*), the Progress In Electromagnetics Research Symposium (*PIERS*), the IEEE International Conference on Computer Science and Information Technology (*ICCSIT*), the *IEEE* Transaction on Electromagnetic Compatibility (*IEEE EMC*), the International Journal of Circuit Theory and Applications, Recent Patents on Electrical Engineering-journal (*EENG*), the Journal of Infrared, Millimeter, and Terahertz Waves, Journal of Electromagnetic Analysis and Applications (*JEMAA*), and the Applied Computational Electromagnetics Society Journal (*ACES*).

Mouloud Challal was born on March 6, 1976, in Algiers, Algeria. He received the Electronics and Communication Engineering Degree from the Université des sciences et de la Technologie Houari Boumediene, Algiers, Algeria, in April 1999, and the M.Sc. degree in microwave and communication from the Ecole Nationale

Polytechnique, Algiers, Algeria, in Dec. 2001. From 1998 to 1999, he acted as computer engineer in private company; in charge of maintenance, computer network installation (LAN), Algiers. From 1999 to 2002, he taught computer science in a public institute (Ex- ITEEM), Algiers. Since 2004, he is a lecturer and a researcher in the Institute of Electrical and Electronics Engineering, (IGEE, Ex. INELEC), University of Boumerdes (UMBB), Boumerdes, Algeria. Since 2007/2008 academic year, is registered as Researcher/PhD student at both UMBB and Université catholique de Louvain (UCL), Louvain-a-Neuve, Belgium. His research interests include RF/Microwave circuits, design and analysis of microstrip filters, defected ground structures behaviors, wireless communication systems, microstrip antenna array analysis, synthesis and design. He is an IEEE, EuMA, IAENG and SDIWC Member.

Arab Azrar was born in Takerboust, Bouira, Algeria, on August 2, 1971. He received the B.S. degree in Electrical and Electronic Engineering form National Institute of Electricity and Electronics of Boumerdes Algeria in 1995 and the MS and doctorate degrees from National Polytechnic school of El-Harrach; Algeria respectively in 1998 and 2004. Currently, he is a lecturer in the institute of Electrical and Electronic Engineering of Boumerdes University and his fields of interest include Antennas, Propagation, and Microwaves.

Improvement of Transmission Line Matrix Method Algorithm Frequency Response Based on Modification of Cell Impedance

M. Rajabi and N. Komjani

Department of Electrical Engineering
Iran University of Science and Technology, Tehran, Iran
Mahdi_Rajabi@ee.iust.ac.ir, n_Komjani@IUST.ac.ir

Abstract ─ In this paper, an accurate and numerically robust singularity correction technique for the transmission line matrix method (TLM) algorithm is proposed. The impedance of the adjacent cells to the singularity is corrected by a scalar correction factor, which amounts to a quasi-static correction of the electric and magnetic energy stored in the TLM cells at the singularity. The effectiveness of this method in accurate modeling of structures with metallic strips (sharp edges) and 90 degree edge corners has been clearly validated against published measurement and common TLM simulation data.

Index Terms ─ Dispersion error, singularity, TLM.

I. INTRODUCTION

Like all other numerical techniques the transmission line matrix method (TLM) is subject to various sources of error and must be treated with caution to obtain reliable and accurate results. Regarding the discrete nature of the TLM method, there are two error sources, velocity or dispersion error and coarseness error.

In most of the simulations, the wavelength of the TLM network is large enough compared with the cell size; therefore, it can be assumed that the fields propagate with the same frequency-independent velocity in all directions and the TLM network shows the behavior of a continuous medium. However when the frequency or the cell size is increased, the network velocity becomes dispersive and depends on the frequency and the direction of propagation. Hence, the assumption of the continuous medium for the TLM network is not valid and leads to an error that is referred to as velocity or dispersion error.

The coarseness error occurs when the TLM mesh is too coarse to resolve the highly non-uniform fields at corners and edges. On the other hand, due to the singularity of some components of the electromagnetic field at corners and edges, the coarseness error occurs.

Both of the dispersion and coarseness errors cause a shift in the frequency response of the structures under investigation as the shift is usually towards low frequencies. However, positive shift in some particular combinations of dielectric and magnetic materials is possible too.

Since the effect of field singularities is significant, many approaches have been proposed for dealing with the field singularities in the vicinity of metal edges in FDTD and TLM [1] . A possible solution could be to choose a very fine mesh[2,3,4]. Another approach is to use appropriate boundary conditions [5] . The lower memory requirements and computation time are the advantages of this approach. A better approach is to use basis functions at the discontinuities that resemble the singular fields at metallic edges and corners [5] . The idea used in this approach is that the singular field distribution is quasi-static since the time derivative of the fields is insignificant compared with their space derivative. Therefore, the properties of the quasi-static field sub-region can be modified so that the stored energy is correct even though the field itself is poorly resolved. For example, modifying the update equations in a FDTD algorithm or the scattering matrix of cells in the vicinity of singularity in TLM is one possible correction method [6].

Using an additional modeling element is another approach that is used for the singularity correction [7, 8]. Discontinuity modeling with material properties is another approach used for modeling singularities. The main idea in this approach is based on the quasi-static distribution of the singular field. It means some of the field components become infinite at sharp edges and corners, whereas the stored energy remains finite. Although this technique is used in perfectly matched layer boundary conditions (PML) [9] , the local character of singularity fields implies that they are independent of boundary conditions several mesh cells away.

II. LOCAL MODIFICATION OF TLM CELLS

This method is based on the local modification of the impedance in the TLM cells directly surrounding the discontinuity. It is robust and independent of the type of singularity from the numerical standpoint. Furthermore, it can be easily implemented to function automatically and has a negligible computational cost compared to the other methods. Modification of TLM cell impedance in the vicinity of discontinuities is implemented by changing the dielectric permittivity and magnetic permeability. The constitutive parameters are the only structural parameters presented in the 3D-TLM dispersion equation[10]. In other words, modification of these parameters resulted in modification of the dispersion relation in the 3D-TLM network.

Maxwell's equation for a symmetric anisotropic media are given by

$$\nabla \times E = -\mu \frac{\partial H}{\partial t}$$
$$\nabla \times H = \varepsilon \frac{\partial E}{\partial t}. \tag{1}$$

The permittivity tensor ε and the permeability tensor μ are

$$\mu = \begin{bmatrix} \mu_x & 0 & 0 \\ 0 & \mu_y & 0 \\ 0 & 0 & \mu_z \end{bmatrix}, \varepsilon = \begin{bmatrix} \varepsilon_x & 0 & 0 \\ 0 & \varepsilon_y & 0 \\ 0 & 0 & \varepsilon_z \end{bmatrix}. \tag{2}$$

Following as [10], the dispersion relation is obtained as the combination of wave vector $\vec{k}$ and constitutive parameters μ and ε. A significant simplification of the dispersion relation is obtained for isotropic media leading to

$$\omega^2 \left(k_x^2 + k_y^2 + k_z^2 - \varepsilon\mu\omega^2 \right)^2 = 0. \tag{3}$$
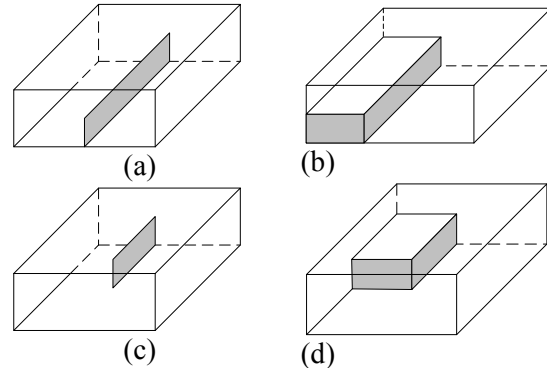
Fig. 1. Four types of singularities (a) knife edge, (b) 90 degree edge, (c) knife edge corner, (d) 90 degree edge corner.

The dispersion analysis for the symmetrical condensed node (SCN) of 3D-TLM yields a direct relationship between the relative permittivity and relative permeability as seen in the equation (3) [10]. In this paper, we used the above relation to compensate the locally structural dispersions created by discontinuities of electromagnetic structures. To further explain the capability of the proposed technique in this paper, some common structural discontinuities such as knife edge, 90 degree edge, knife edge corner, and 90 degree edge corner are investigated.

For modeling these structures, both constitutive parameters of the cells' surrounded by discontinuities are reduced by the same relative amount in order to preserve the local intrinsic wave impedance of the field space. For example in the knife edge structure, the ε and μ of the edge cells are modified such that the resonant frequencies of a resonator that contains the edge singularity become virtually independent of the cell size.

The required change in ε and μ can be computed approximately using the known expressions for the quasi-static fields. This is illustrated in Fig. 2 where the dominant resonant frequency of a cavity with a knife edge singularity

has been drawn as a function of mesh parameter (Δl) used to compute that frequency. Note that the mesh parameter is small enough for the dispersion error to be negligible $(\Delta l/\lambda \ll 1/20)$.

If the structural singularity is not corrected, the frequency varies linearly with the mesh parameter. After the modification, the computed resonant frequency is practically independent of the mesh parameter. The correction region is along the edge but contains only the immediately adjacent cells. Figure 3 shows the location of the modified cells.
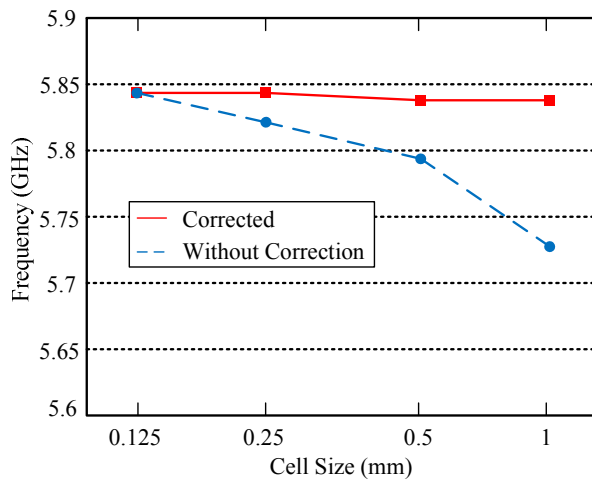
Fig. 2. Resonant frequency of cavity containing a knife edge singularity with a=20 mm, b=15 mm, c=10 mm, and $\varepsilon_r = \mu_r =2$.

As can be seen in Fig. 2, the frequency shift phenomenon is dropped after modification. The frequency shift between simulation with $\Delta l =1$ mm and $\Delta l =0.125$ mm before modification is about 135 MHz and after modification this shift is reduced to 5 MHz which means 90% error correction by the corrected algorithm.

This modification can be repeated for other types of singularities like 90 degree edge. Fig. 4 shows the location of cell correction for this type of singularity. The cavity dimensions are a=14 mm, b=10 mm, c=6 mm, d=5 mm, and s=3 mm with parameters of $\varepsilon_r = \mu_r =2$.
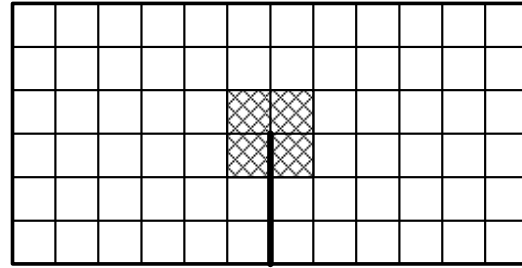
Fig. 3. Location of the cell correction for knife edge singularity.
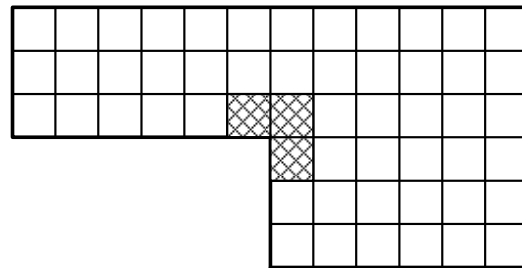
Fig. 4. Location of the cell correction for 90 degree edge singularities.

Figure 5 shows the simulation results of the 90 degree edge singularity. Elimination of the frequency shift is evident which led to independence of the resonant frequency to the mesh parameter. In this type of singularity, the corrected cells are located adjacent to the 90 degree edge singularity. With respect to the above results, it is clear that the physical modeling of discontinuities by changing the cell impedance in the location of singularity is accurate and efficient. In addition, this approach not only increases the accuracy of the applied numerical methods but also decreases the computing cost and the simulation time of modeled structures.
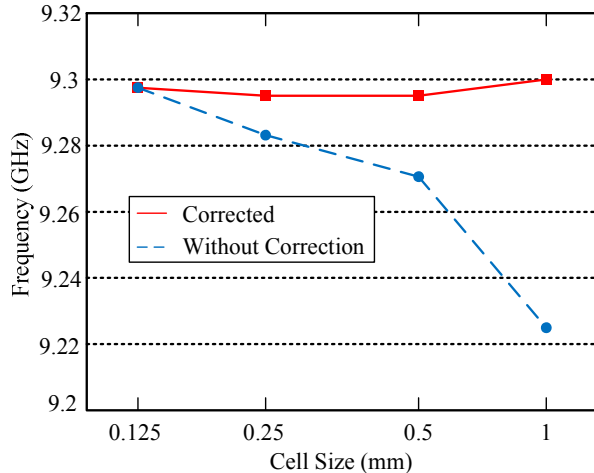
Fig. 5. Resonant frequency of cavity containing 90 degree edge singularities.

Fig. 7. Result of patch antenna simulation.

In order to experimentally validate the accuracy and efficiency of the correction method proposed in this paper, this approach has been used to analyze microstrip structures such as antenna and filter.

III.   SIMULATION

A. Patch antenna

The geometry of the antenna is exactly the same as in [11] so that the results can be compared (Fig. 6). The feed line of the antenna is $50\,\Omega$ microstrip with ε_r =2.2 and h=0.794 mm.

In simulation of this antenna, the computational domain with $120 \times 70 \times 25$ cells is used and the patch is modeled by $40\,\Delta x \times 32\,\Delta y$ where Δx = 0.4 mm, Δy = 0.389 mm, and Δz = 0.265 mm. The width and length of this feed line and the height of substrate are modeled by 6, 50 and 3 nodes, respectively.

Fig. 6. Patch antenna.

The time step is $\Delta t = 0.43$ ps and simulation is performed for 10000 time steps because of the highly resonant behavior of the antenna. Note that this structure has two types of singularities in form of edge and corner and both of them should be corrected.

The results of the simulation by modified algorithm are listed in Table 1. In Fig. 7, the reflection coefficient of the patch antenna is also compared with corrected TLM result.

By considering measurement frequencies, the applied modification is about 80% and the whole of the frequency response is not corrupted by this modification in the frequency range of response.

Table 1: Resonant frequency of the patch antenna

Frequency (GHz)	1st	2nd
TLM Without correction	7.51	18.07
Corrected TLM	7.61	18.29
Measurement [12]	7.60	18.37
Without correction Error(%)	1.31	1.63
Corrected Error(%)	0.13	0.44

B. Low pass filter

Figure 8 shows the geometry of a low pass microstrip filter which fabricated by RT/Duroid 5880 (ε_r = 2.2, h= 0.794 mm) and the substrate is on the y-z plane. Dimension of the simulation cell is Δx = 0.4233 mm, Δy = 0.1985 mm, and Δz = 0.4064 mm and the computational domain with $20 \times 74 \times 86$ cells is used for simulation of this filter.
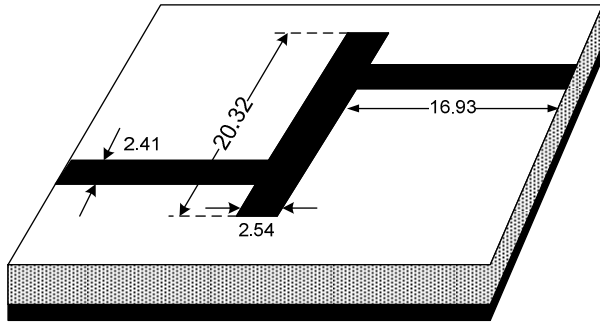
Fig. 8. Geometry of low pass filter.
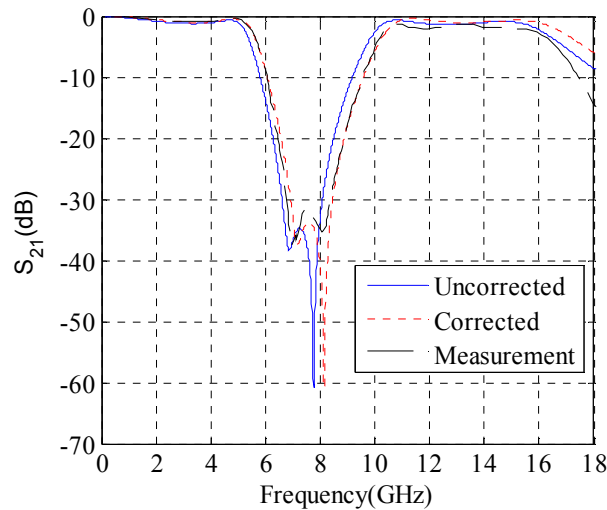
Fig. 9. Insertion loss of low pass filter.
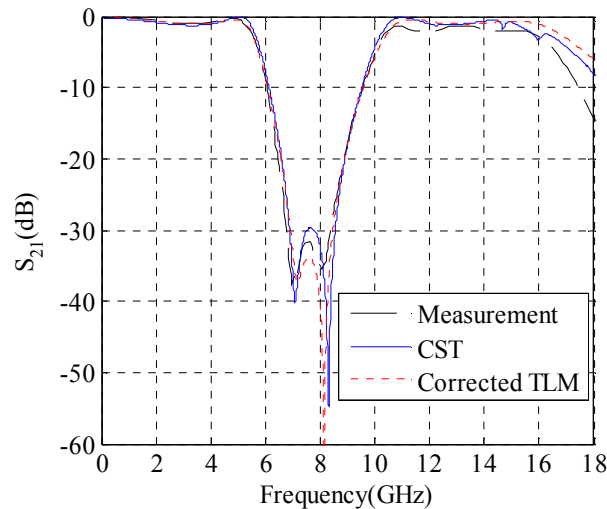
Fig. 10. Corrected TLM filter result compared with CST microwave studio simulation and measurement result.

The distance from the source plane to the edge of the long patch is $30\,\Delta x$ and the reference planes for ports 1 and 2 are $10\,\Delta x$ from the edges of the patch. The time step is $\Delta t = 0.3176$ ps. The simulation is performed for 10000 time steps to allow the response on both ports to become nearly zero.

In Fig. 9, the simulation results of the filter are shown in comparison with measurement results [11] . With respect to the filter geometry, the impedance of the edge discontinuities and adjacent cells has been changed in the corrected algorithm.

In comparison with measurement results, the proposed modification in the TLM algorithm could compensate shift in the frequency response of the filter, as the cut-off frequency of the low pass filter improved approximately 90% in comparison with the common TLM algorithm. In general, a good agreement of the corrected algorithm results and CST Microwave Studio simulation result is seen in Fig. 10.

CONCLUSION

In this paper, an accurate and numerically robust singularity correction technique for the TLM algorithm has been proposed. The impedance of the cell adjacent to the singularities are modified by a scalar correction factor, which amounts to a quasi-static correction of the electric and magnetic energy stored in the TLM cells at the singularities. The correction factor also affected the dispersion equation because of the constitutive parameter dependency of this equation. Numerical validation shows that this correction method reduces the coarseness error due to singularity without any penalty in terms of computational burden.

REFRENCES

[1] J. Hesselbarth and R. Vahldieck, "Resonance Frequencies Calculated Efficiently with the Frequency-Domain TLM Method," *IEEE MWCL*, vol. 13, no. 5, pp. 190-192, May 2003.

[2] J. A. Morente, J. A. Porti, H. Magan, and O. Torres, "Improved Modeling of Sharp Zones in Resonant Problems with the TLM method," *Applied Computational*

Electromagnetic Society (ACES) Journal, vol. 14, no. 2, pp. 67-71, July 1999.

[3] J. L. Herring and C. Christopolous, "Multigrid Transmission-Line Modeling Method for Solving Electromagnetic Field Problems," *Electronics Letters*, vol. 27, no. 20, pp. 1794-1795, Sep. 1991.

[4] R. E. Collin, *Field Theory of Guided Waves*, 2nd edition, IEEE Press., New York, 1991.

[5] U. Pekel and R. Mittra, "A Finite-Element-Method Frequency-Domain Application of the Perfectly Matched Layer (PML) Concept," *Microwave and Opt. Tech. Lett.*, vol. 9, no. 3, 1995.

[6] K. R. Umashankar, and A. Taflove, "A Novel Method to Analyze Electromagnetic Scattering of Complex Objects," *IEEE Trans. Electromagn. Compat.*, vol. 24, pp. 392-405, Nov. 1982.

[7] C. J. Railton, "The Inclusion of Fringing Capacitance and Inductance in FDTD for the Robust Accurate Treatment of Material Discontinuities," *IEEE MTT-S International Microwave Symposium Digest*, pp. 391-394, 2000.

[8] P. Sewell, J. Wykes, A. Vukovic, D. W. P. Thomas, T. M. Benson, and C. Christopolous, "Multi-Grid Interface in Computational Electromagnetics," *Electronics Letters*, vol. 40, pp. 162-163, Feb. 2004.

[9] J. P. Berenger, "A Perfectly Matched Layer for the Absorption of Electromagnetic Waves," *Journal of Computational Physics*, vol. 114, no. 185, 1994.

[10] C. Huber, M. Krumpholz, and P. Russer, "Dispersion in Anisotropic Media Modeled by Three-Dimensional TLM," *IEEE Transactions on Microwave Theory and Techniques*, vol. 43, no. 8, pp.1923-1934, August 1995.

[11] D. M. Sheen, S. M. Ali, and J. A. Kong, "Application of the Three-Dimensional Finite-Difference Time-Domain Method to the Analysis of Planar Microstrip Circuits," *IEEE Transactions on Microwave Theory and Techniques*, vol. MTT-38, no. 7, pp. 849-857, July 1990.

[12] T. Shibata, T. Hayashi, and T. Kimura, "Analysis of Microstrip Circuits using Three Dimensional Full Wave Electromagnetic Field Analysis in the Time Domain," *IEEE Transactions on Microwave Theory and Techniques*, vol. MTT-36, no. 6, pp. 1064-1070, June 1998.

Mahdi Rajabi has studied Electrical Engineering since 1997 at Iran University of Science and Technology where he is currently working toward the Ph.D. degree. He received his B.Sc. and M.Sc. from Iran University of Science and Technology, Iran, in 2002 and 2005, respectively. His research interests include numerical methods in electromagnetic, microstrip antennas, and UWB antenna.

Nader Komjani received his B.Sc., M.Sc., and Ph.D. degree all in Electrical Engineering from Iran University of Science and Technology, Iran, in 1988 and 1991, and 2000, respectively. He is currently the Associate Professor with Iran University of Science and Technology. He has taught microstrip antenna, communication systems, advanced engineering mathematics, and electromagnetic courses since 1998.

His research interests are in the areas of UWB and multiband microstrip antennas, numerical methods in electromagnetic, phased array antennas and passive and active microwave systems.

Using Adaptive Cross Approximation for Efficient Calculation of Monostatic Scattering with Multiple Incident Angles

Zhiwei Liu[1], Rushan Chen[1,2], Jiaqi Chen[1], and Zhenhong Fan[1]

[1] Department of Communication Engineering
Nanjing University of Science and Technology, Nanjing, 210094, China
zwliu1982@hotmail.com, eechenrs@mail.njust.edu.cn, cjq19840130@163.com,
zhfan@mail.njust.edu.cn

[2] Science and Technology on Space Microwave Technology, Xi'an, 710000, China
eechenrs@mail.njust.edu.cn

Abstract ─ An adaptive cross approximation (ACA) based method is proposed for the fast analysis of the monostatic radar cross-section (RCS). Using the low-rank property, several largest eigenvalues and corresponding eigenvectors of the multiple right hand sides can be computed and saved efficiently by the ACA algorithm. The iterative solution of linear equations is required at these principle eigenvectors. Compared with solving linear equations at each angle repeatedly, the proposed method is able to greatly reduce the computation time. In order to efficiently solve the linear equations, the flexible general minimal residual (FGMRES) iterative solver is applied to compute the coefficients of Rao-Wilton-Glisson (RWG) basis functions. Numerical results demonstrate that the proposed method is efficient for monostatic RCS calculation with high accuracy.

Index Terms ─ Adaptive cross approximation (ACA), low-rank property, monostatic RCS, and surface integral equation (SIE).

I. INTRODUCTION

Electromagnetic wave scattering problems address the physical issue of detecting the diffraction pattern of the electromagnetic radiation scattered from a large and complex body when illuminated by an incident incoming wave. A good understanding of these phenomena is crucial to radar cross section (RCS) calculation, antenna design, electromagnetic compatibility, and so on. All these simulations are very demanding in terms of computer resources, and require efficient numerical methods to compute an approximate solution of Maxwell's equations. Using the equivalence principle, Maxwell's equations can be recast in the form of integral equations that relate the electric and magnetic fields to the equivalent electric and magnetic currents on the surface of the object. Amongst integral formulations, the surface field integral equation (SIE) is widely used for electromagnetic wave scattering problems as it can handle the most general geometries. The matrix associated with the resulting linear systems is large, dense, complex, and non-Hermitian [1, 21]. It is basically impractical to solve matrix equations using direct methods because they have a memory requirement of $O(N^2)$, where N refers to the number of unknowns. This difficulty can be circumvented by use of iterative methods, and the required matrix-vector product operation can be efficiently evaluated by the multilevel fast multipole algorithm (MLFMA) [2, 3]. The use of MLFMA reduces the memory requirement to $O(N\log N)$ and the computational complexity of per-iteration to $O(N\log N)$. However, it is still time- and memory- consuming for calculation of monostatic RCS since it requires repeated solution of SIE at each incident direction.

Conventional interpolation methods, such as AWE and the cubic-spline (CS) interpolation method, can easily approximate the monostatic RCS. AWE [4, 5] is a kind of classical method

which is widely used in computational electromagnetics. It utilizes the high-order derivatives of the incident current vector at the interval center to extrapolate the value of nearby points, and is considered to be the AWE extrapolation method in this paper. AWE interpolation method [6] has been introduced by Wei. Piecewise interpolation technique is used and the first-order derivative of samples is required. The cubic spline interpolation method [7, 8] is another popular numerical approximate method. It utilizes the information of C^1-continuous to evaluate the first derivative of the incident current vector instead of solving the large linear equations.

How to select the sampling points is a difficult problem for interpolation and extrapolation methods. The active learning method is proposed by Zhao to obtain the optimal samples over wide frequency band [9, 10]. In [7, 8], Liu proposed an adaptive sampling method to obtain the optimal samples for monostatic RCS calculation with wide angular band. However, the performance of adaptive sampling is very sensitive with the initial samples. Furthermore, the sampling nodes are not the exact optimal samples but the approximately optimal samples.

In monostatic RCS computation [18], the main computation cost is the solution of the linear system with multiple right hand sides. Inspired by [11, 20, 22], the multiple right hand sides can be approximately described by a low-rank form. SVD can evaluate several large eigenvalues and corresponding eigenvectors of the multiple right hand sides. Moreover, the SVD process can be efficiently performed by the adaptive cross approximation (ACA) algorithm [17]. The process of solving linear equations is only required at these principle eigenvectors. Compared with the repeated solution at each angle, the proposed method is able to greatly reduce the times of linear equations solution. Furthermore, this non-adaptive method leads to a more robust algorithm than the adaptive sampling method. Accordingly, the ACA-based method is used for fast computation of monostatic RCS in this paper.

The remainder of this paper is organized as follows. Section II demonstrates the basic theory and formulations of surface integral equations. Section III describes the low-rank decomposition of multiple right hand sides in monostatic RCS computation. The application of the ACA

algorithm is also discussed in this section. Numerical experiments of several geometries are presented to demonstrate the efficiency of this proposed method in Section IV. The conclusion is provided in Section V.

II. CFIE FORMULATINONS

For electromagnetic scattering from the perfect electrical conductor (PEC), the combined field integral equation (CFIE) is widely used for closed structure [12]. The CFIE formulation of electromagnetic wave scattering problems using planar RWG basis functions for surface modeling is presented in [13]. The resulting linear systems from CFIE formulation after Galerkin's testing are briefly outlined as follows:

$$\sum_{n=1}^{N} Z_{mn} a_n = V_m \,, m = 1,2, \dots, N \qquad (1)$$

where $Z_{mn} = \dfrac{\alpha}{\eta} Z_{mn}^{EFIE} + \left(1-\alpha\right) Z_{mn}^{MFIE}$ and

$$Z_{mn}^{EFIE} = jk\eta \int_{S_m} \mathbf{\Lambda}_m \int_{S_n} \left(\bar{\bar{\mathbf{I}}} + \frac{\nabla\nabla}{k^2} \right) G\left(\mathbf{r},\mathbf{r}'\right) \mathbf{\Lambda}_n d\mathbf{r}' d\mathbf{r}$$

$$Z_{mn}^{MFIE} = \frac{1}{2}\int_{S_m} \mathbf{\Lambda}_m \mathbf{\Lambda}_n d\mathbf{r} - \int_{S_m} \mathbf{\Lambda}_m \cdot \hat{\mathbf{n}} \times \nabla \times \int_{S_n} G\left(\mathbf{r},\mathbf{r}'\right) \mathbf{\Lambda}_n d\mathbf{r}' d\mathbf{r}$$

$$V_m = \int_{S_m} \mathbf{\Lambda}_m \cdot \left[\alpha \frac{\mathbf{E}^{inc}}{\eta} + \left(1-\alpha\right) \hat{\mathbf{n}} \times \mathbf{H}^{inc} \right] d\mathbf{r}.$$

Here, G($\mathbf{r}$, $\mathbf{r}'$) refers to the Green's function in free space and $\{a_n\}$ is the column vector containing the unknown coefficients of the surface current expansion with RWG basis functions. Also, $\mathbf{r}$ and $\mathbf{r}'$ denote the observation and source point locations. η and k denote the free space impendence and wave number, respectively. Once the matrix equation (1) is solved by numerical matrix equation solvers, the expansion coefficients $\{a_n\}$ can be used to calculate the scattered field and RCS. In the following, we use A to denote the coefficient matrix in equation (1), $\mathbf{x} = \{a_n\}$, and $\mathbf{b} = \{V_m\}$ for simplicity. Then, the CFIE matrix equation (1) can be symbolically rewritten as:

$$\mathbf{Ax} = \mathbf{b}. \qquad (2)$$

To solve the above matrix equation by an iterative method, the matrix-vector products are needed at each iteration step. Physically, a matrix-vector product corresponds to one cycle of iterations between the basis functions. The basic idea of the fast multipole method (FMM) is to

convert the interaction of element-to-element to the interaction of group-to-group. Here, a group includes the elements residing in a spatial box. The mathematical foundation of the FMM is the addition theorem for the scalar Green's function in free space. Using the FMM, the matrix-vector product Ax can be written as:

$$\mathbf{Ax} = \mathbf{A}_N\mathbf{x} + \mathbf{A}_F\mathbf{x}. \qquad (3)$$

Here, $\mathbf{A}_N$ is the near part of A and $\mathbf{A}_F$ is the far part of A. In the FMM, the calculation of matrix elements in $\mathbf{A}_N$ remains the same as in the MoM procedure. However, those elements in $\mathbf{A}_F$ are not explicitly computed and stored. Hence, they are not numerically available in the FMM. It has been shown that the operation complexity of FMM to perform Ax is $0(N^{1.5})$. If the FMM is implemented in multilevel, the total cost can be reduced further to $0(NlogN)$ [2, 3].

III. LOW-RANK DECOMPOSITION OF MULTIPLE RIGHT HAND SIDES

The monostatic RCS requires repeated calculations at each angle over the band of interest. This process can be computationally prohibitive for computation of monostatic RCS of an electrically large object. In order to accelerate the computation of monostatic RCS, an ACA based method is proposed and the methodology on how the efficient calculation of monostatic scattering is discussed in this section.

The computation of monostatic RCS can be considered as linear equations with multiple right hand sides

$$\mathbf{A}\cdot\mathbf{X} = \mathbf{B}, \qquad (4)$$

where A is the impedance matrix, X is the multiple complex coefficient vector of RWG basis, and B is the multiple right hand side generated by the incident wave. And

$$\mathbf{X} = [\mathbf{x}(\theta_1), \ldots, \mathbf{x}(\theta_n)], \quad \mathbf{B} = [\mathbf{b}(\theta_1), \ldots, \mathbf{b}(\theta_n)], (5)$$

where θ_i is the ith incident angle. Using the traditional singular value decomposition (SVD), the matrix B can be described as the form of eigenvalue and eigenvector.

$$\mathbf{B} = \mathbf{U}\cdot\mathbf{\Sigma}\cdot\mathbf{V}^{H}. \qquad (6)$$

If the dimension of B is $N \times M$, the dimension of matrices U, $\mathbf{\Sigma}$, and V are $N \times M$, $M \times M$, $M \times M$, respectively. N is the number of unknowns. $\mathbf{\Sigma}$ is a diagonal matrix including all the eigenvalues of B

while U and V contain all the eigenvectors of B. When B is the multiple right hand sides in the linear system connecting with the SIE used for monostatic RCS, matrix B is low-rank and can be approximately described as a low-rank SVD form.

$$\mathbf{B} \approx \mathbf{U}_k\cdot\mathbf{\Sigma}_k\cdot\mathbf{V}_k^{H,} \qquad (7)$$

where the dimension of matrices $\mathbf{U}_k$、 $\mathbf{\Sigma}_k$ and $\mathbf{V}_k$ are $N \times k$, $k \times k$, $M \times k$, respectively. Only k largest eigenvalues and corresponding eigenvectors are reserved in (7). Substitude (7) to (4), the linear equations can be rewritten as

$$\mathbf{X} \approx (\mathbf{A}^{-1}\cdot\mathbf{U}_k)\cdot\mathbf{\Sigma}_k\cdot\mathbf{V}_k^{H.} \qquad (8)$$

Here, $\mathbf{A}^{-1}\cdot\mathbf{U}_k$ can be computed by any iterative solver. If using direct solver to compute the inversion of matrix A [19], the proposed method will become useless. Therefore, the times for solution of equation (2) is only k when using the SVD method while that of traditional direct solution is M for monostatic RCS, where M is the number of multiple right hand sides. Generally, k is much smaller than M which leads to an efficient method for computation of monostatic RCS over a wide angular band.

The key problem for this proposed method is how to obtain the decomposition form of multiple right hand sides. As well known, the traditional SVD method is a good analytical solution for this problem. However, SVD requires the computation of the matrix including all right hand sides and the complexity of the computation time of SVD is $O(nm^2 + mn^2)$, where m and n respect to the number of rows and columns. When the number of unknowns or right hand vectors is large, this analytical solution is not practical. In order to alleviate this difficulty, an adaptive cross approximation (ACA) algorithm is applied and performs a more efficient property than the traditional SVD method.

Using the adaptive cross approximation approach, a low-rank matrix can be decomposed into two matrices $\mathbf{U}_{ACA}$ and $\mathbf{V}_{ACA}$. The RHS matrix B, which is low-rank, can also be decomposed into $\mathbf{U}_{ACA}$ and $\mathbf{V}_{ACA}$ matrices. The formula of the decomposition is listed below

$$\mathbf{B} \approx \mathbf{U}_{ACA}\cdot\mathbf{V}_{ACA}^{H,} \qquad (9)$$

where the dimension of matrices $\mathbf{U}_{ACA}$ and $\mathbf{V}_{ACA}$ are $N \times k$, $M \times k$, respectively. Substitute (9) to (4), the linear equations can be rewritten as

$$\mathbf{X} \approx (\mathbf{A}^{-1}\mathbf{U}_{ACA})\cdot\mathbf{V}_{ACA}^{H.} \qquad (10)$$

k is much smaller than M which leads to an efficient method for computation of monostatic

RCS over a wide angular band. Here, $\mathbf{A}^{-1}\cdot\mathbf{U}_{ACA}$ is computed by an iterative solver.

The algorithm of ACA is presented as follows, which allows it to generate only a few rows and columns of the matrix and approximates the rest of the matrix using only this information.

Adaptive Cross Approximation Algorithm

Let $\mathbf{U}_{ACA}$ = NULL which is used to save the selected columns and $\mathbf{V}_{ACA}$ = NULL which is used to save the selected rows.

Step1: Choose the first column $\mathbf{u}_1$ randomly and let $\mathbf{U}_{ACA} = \mathbf{U}_{ACA} \cup \{\mathbf{u}_1\}$. Find the max value $\mathbf{u}_{1k}$ in $\mathbf{u}_1$. Then choose the first row $\mathbf{v}_1$ which located at kth row in the matrix. Let $\mathbf{V}_{ACA} = \mathbf{V}_{ACA} \cup \{\mathbf{v}_1\}$.

Step 2: Find the max value $\mathbf{v}_{ik}$ in $\mathbf{v}_i$. Then choose the $(i + 1)$th column $\mathbf{u}_{i+1}$ which located at kth column in the matrix.

Step 3: $\mathbf{u}_{i+1} = \mathbf{u}_{i+1} - \sum_{j=1}^{i} v_{j,i}\mathbf{u}_j$, and let $\mathbf{U}_{ACA} = \mathbf{U}_{ACA} \cup \{\mathbf{u}_{i+1}\}$.

Step 4: Find the max value $\mathbf{u}_{i+1,k}$ in $\mathbf{u}_{i+1}$. Then choose the $(i + 1)$th row $\mathbf{v}_{i+1}$ which located at kth row in the matrix.

Step 5: $\mathbf{v}_{i+1} = \mathbf{v}_{i+1} - \sum_{j=1}^{i} u_{j,i}\mathbf{v}_j$, and let $\mathbf{V}_{ACA} = \mathbf{V}_{ACA} \cup \{\mathbf{v}_{i+1}\}$.

Step 6: If $\dfrac{\langle \mathbf{u}_{i+1}, \mathbf{u}_{i+1} \rangle \langle \mathbf{v}_{i+1}, \mathbf{v}_{i+1} \rangle}{\langle \mathbf{u}_1, \mathbf{u}_1 \rangle \langle \mathbf{v}_1, \mathbf{v}_1 \rangle} < \varepsilon$, the algorithm will stop, otherwise, go to Step 2. The low-rank decomposition form of RHS matrix is $\mathbf{B} \approx \mathbf{U}_{ACA}\cdot\mathbf{V}_{ACA}{}^{\mathrm{H}}$.

This algorithm produces a sequence of decompositions of a matrix into a sum of low-rank matrix and error matrix. Neither the original matrix nor the error matrix will be computed completely. How to decide the tolerance error ε is the most important thing in ACA. In order to avoid the numerical error, the ε is required to be small enough. In this paper, the ε satisfies $\varepsilon = 10^{-3}$.

IV. NUMERICAL RESULTS

In this section, a number of numerical results are presented to demonstrate the accuracy and efficiency of the ACA based method for fast calculation of monostatic RCS over wide angular band. The flexible general minimal residual (FGMRES) [14, 15] algorithm is applied to solve linear systems. The dimension size of the Krylov subspace is set to be 30 for the outer iteration and the dimension is set to be 10 for the inner iteration. The tolerance of the inner iteration is 0.1 in this paper. All experiments are conducted on an Intel Core(TM) II Duo with 3.45 GB local memory and run at 2.40 GHz in single precision. The iteration process is terminated when the 2-norm residual error is reduced by 10^{-3}, and the limit of the maximum number of iterations is set as 1000.

Three geometries are applied to illustrate the performance of our proposed method. They consist of a NASA almond with 1815 unknowns [16], a PEC double-ogive with 4635 unknowns, and the VFY-218 model with 40725 unknowns. Since the number of right hand vectors is small for 1-D angular sweep in this paper, it is feasible to apply the traditional SVD for computing the eigenspace of multiple right hand sides. As shown in Figs.1-3, the monostatic RCS curve of NASA almond, double-ogive, and VFY-218 which computed by ACA method is compared with the curve computed by direct solution repeatedly. It is obvious that the ACA method is accurate since there is no significant difference between the RCS result obtained by the direct solution and the ACA method. As shown in Tab.1, when compared with the traditional SVD method, the ACA based method provides little advantage on total computation time since the number of right hand side is small.

For monostatic RCS simultaneous theta and phi sweep, the number of right hand sides is 32761 (181×181) for almond and double-ogive in this paper. Due to the time complexity of traditional SVD is $O(nm^2 + mn^2)$, it is not suitable to obtain the eigenvalue of the multiple right hand sides directly. Thus, the ACA is applied in the last two examples. From these results, the same conclusion as that in 1-D monostatic RCS examples can be obtained, which shows the ACA based method is accurate.

The relative error of the last two examples is demonstrated by Figs. 4(c), 5(c), 6(c), and 7(c). In order to demonstrate the relative error of the proposed method, the formulation of relative error is defined as

$$error = \frac{\left|\mathbf{E}_{svd} - \mathbf{E}_{direct}\right|}{\left|\mathbf{E}_{direct}\right|} \ . \tag{9}$$
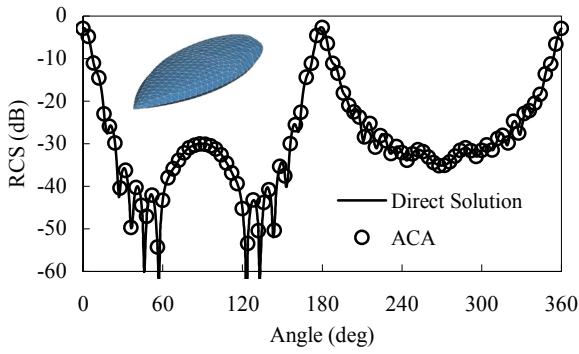
(a)
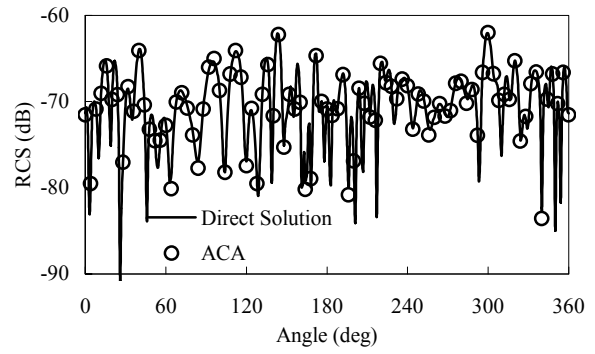
(b)
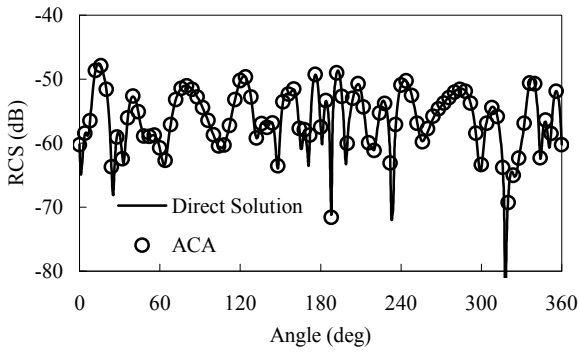
Fig. 1. monostatic RCS of NASA almond for simultaneous theta sweep: (a) HH-pol; (b) HV-pol.

(b)

Fig. 2. monostatic RCS of double-ogive for simultaneous theta sweep: (a) HH-pol; (b) HV-pol.
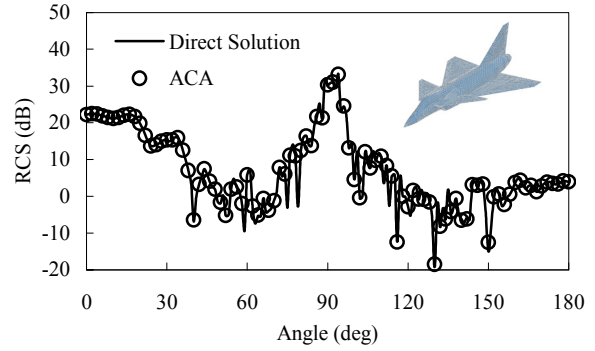
(a)
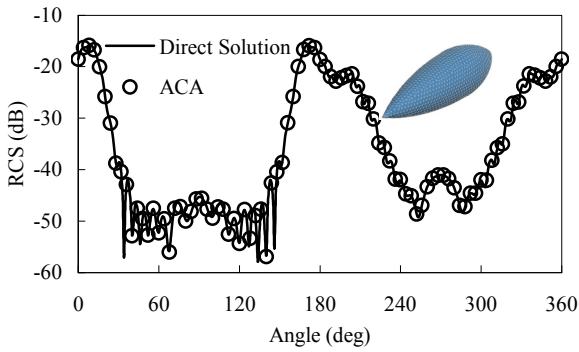
(a)
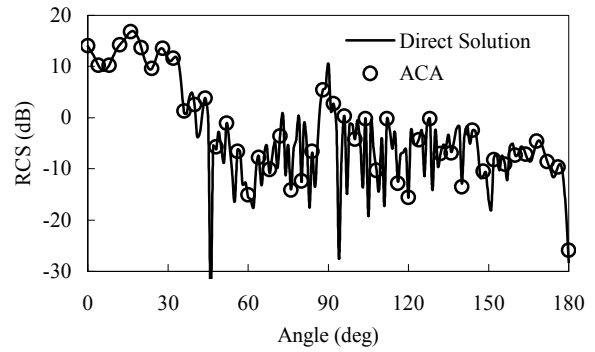
(b)

Fig. 3. monostatic RCS of VFY-218 for simultaneous theta sweep: (a) HH-pol; (b) HV-pol.

(a)

(b)
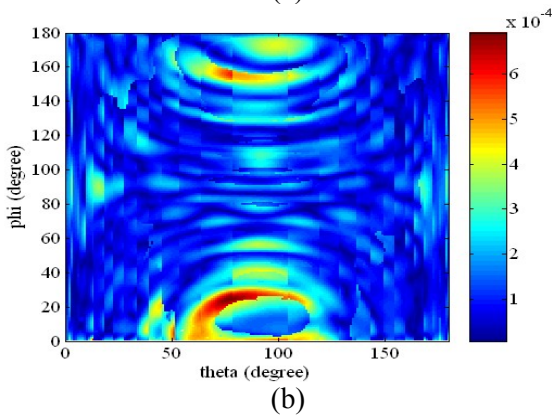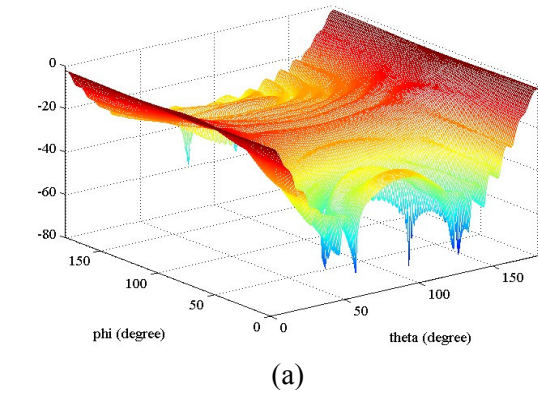
Fig. 4. Monostatic RCS of NASA almond for simultaneous theta and phi sweep, HH-pol: (a) RCS; (b) relative error.

(a)

(b)
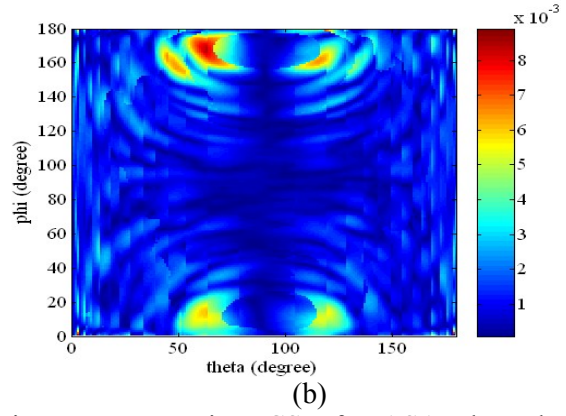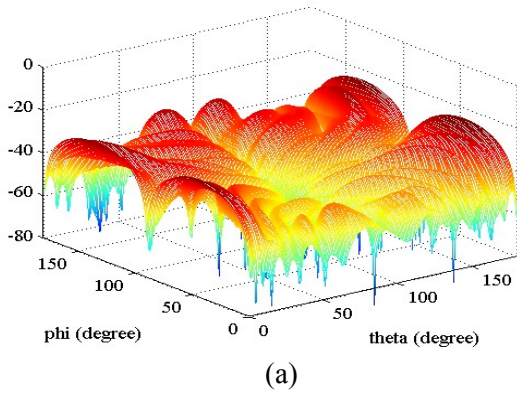
Fig. 5. Monostatic RCS of NASA almond for simultaneous theta and phi sweep, HV-pol: (a) RCS; (b) relative error.

(a)

(b)
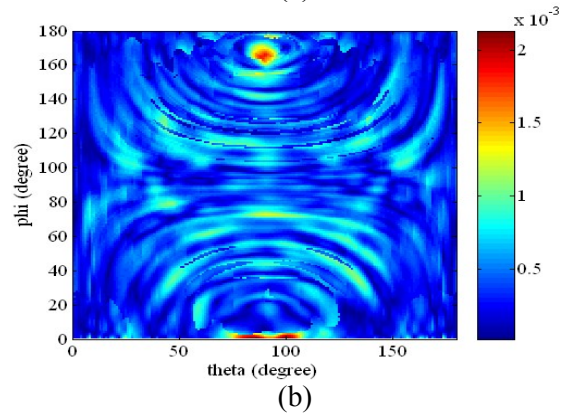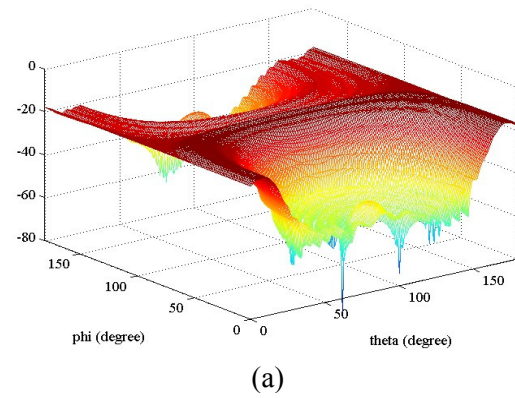
Fig. 6. Monostatic RCS of double-ogive for simultaneous theta and phi sweep, HH-pol: (a) RCS; (b) relative error.

Table 1: Computation time of monostatic RCS with 1-D angular sweep

| Object | f (Hz) | N | Pol | Angular Sweep | | Time (Second) / Number of Solutions | | |
				Theta (deg)	Phi (deg)	Direct Solution	Traditional SVD	ACA
Almond	5G	1815	HH	0~360	0	222 / 361	38 / 22	26 / 25
			HV	0~360	0	234 / 361	39 / 26	26 / 26
D-Ogive	12G	2571	HH	0~360	0	652 / 361	92 / 45	89 / 45
			HV	0~360	0	647 / 361	92 / 41	88 / 45
VFY-218	0.5G	40725	HH	90	0~180	106618 / 361	29855 / 73	28732 / 73
			HV	90	0~180	106545 / 361	29734 / 73	28744 / 73

Table 2: Computation time of monostatic RCS for simultaneous theta and phi sweep

| Object | f (Hz) | N | Pol | Angular Sweep | | Time (Second) / Number of Solutions | | |
				Theta (deg)	Phi (deg)	Direct Solution	Traditional SVD	ACA
Almond	5G	1815	HH	0~180	0~180	20315 / 32761	2340 / 158	570 / 159
			HV	0~180	0~180	20322 / 32761	2287 / 161	566 / 161
D-Ogive	12G	2571	HH	0~180	0~180	60832 / 32761	8714 / 293	2208 / 295
			HV	0~180	0~180	60813 / 32761	8862 / 295	2187 / 295

(a)

(b)
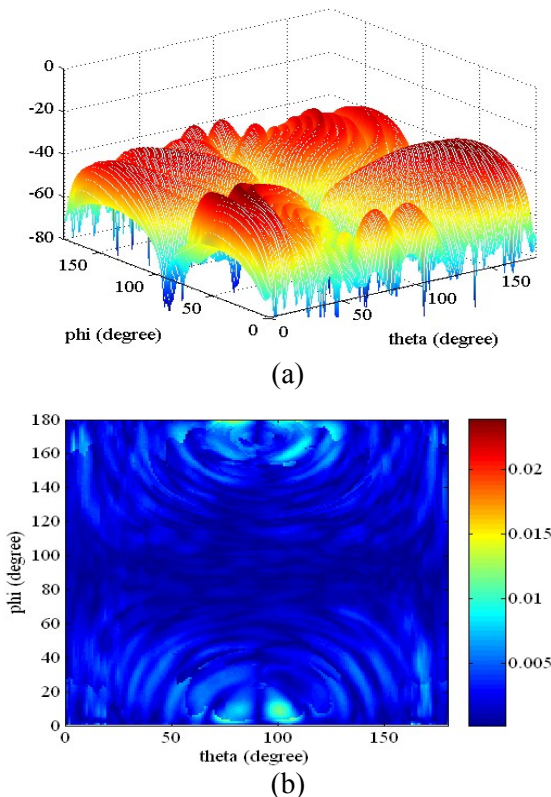
Fig. 7. Monostatic RCS of double-ogive for simultaneous theta and phi sweep, HV-pol: (a) RCS; (b) relative error.

From the error shown in Figs. 4(c), 5(c), 6(c), and 7(c), it is obvious that the error of cross-polarization is larger than co-polarization. However, the error of both polarizations is small enough to obtain the accurate result. Thus, the ACA based method can be considered as an accurate method.

Tables 1 and 2 show the CPU time of direct solution, traditional SVD based method, and ACA based method. It is shown that plenty of time can be saved in traditional SVD and ACA based method since the times of equation solutions is much fewer than solving the linear equations (4) repeatedly. Comparing the CPU time between the traditional SVD method and the ACA method, it is concluded that the ACA method is more efficient when the number of right hand side vectors is large enough.

V. CONCLUSION

In this paper, an ACA based method is proposed for efficient analysis of the monostatic scattering from electrically large objects over a wide angular band. After obtaining the eigenvalues and eigenvectors of the multiple right hand sides by the adaptive cross approximation algorithm, the total solution time can be saved since the iterative solution of linear system is only needed at several largest eigenvalues. In order to fast solution of the linear system, the MLFMA,

and Krylov subspace iterative solver are used to efficiently solve the linear equations. Numerical experiments demonstrate that our proposed method is more efficient when compared with the repeated solution at each angle for electromagnetic scattering from the electrically large objects.

ACKNOWLEDGMENT

REFERENCES

[1] R. F. Harrington, *Field computation by moment methods*, Malabar, Fla.: R. E. Krieger, 1968.

[2] W. C. Chew, J. M. Jin, E. Michielssen, and J. M. Song, *Fast and Efficient Algorithms in Computational Electromagnetics*. Boston, MA: Artech House, 2001.

[3] J. M. Song, C. C. Lu, and W. C. Chew, "Multilevel Fast Multipole Algorithm for Electromagnetic Scattering by Large Complex Objects," *IEEE Trans. Antennas Propagat.*, vol. 45, no. 10, pp. 1488-1493, 1997.

[4] Y. E. Erdemli, J. Gong, C. J. Reddy, and J. L. Volakis. "Fast RCS Pattern Fill Using AWE Technique," *IEEE Trans. Antennas Propagat*, vol. 46, no. 11, pp. 1752-1753, 1998.

[5] R. D. Slong, R. Lee, and J. F. Lee. "Multipoint Galerkin Asymptotic Waveform Evaluation for Model Order Reduction of Frequency Domain FEM Electromagnetic Radiation Problems," *IEEE Trans. Antennas Propagat*, vol. 49, no. 10, pp. 1504-1513, 2001.

[6] X. C. Wei, Y. J. Zhang, and E. P. Li. "The Hybridization of Fast Multipole Method with Asymptotic Waveform Evaluation for the Fast Monostatic RCS Computation," *IEEE Trans. Antennas Propagat*, vol. 52, no. 2, pp. 605-607, 2004.

[7] Z. W. Liu, R. S. Chen, and J. Q. Chen, "Adaptive Sampling Cubic-Spline Interpolation Method for Efficient Calculation of Monostatic RCS," *Micro. Opt. Tech. Lett.* vol. 50, no. 3, pp. 751-755, 2008.

[8] Z. W. Liu, D. Z. Ding, Z. H. Fan, and R. S. Chen, "Adaptive Sampling Bicubic Spline Interpolation Method for Fast Computation of Monstatic RCS," *Micro. Opt. Tech. Lett.* vol. 50, no. 7, pp. 1851-1857, 2008.

[9] Z. Q. Zhao, C. H. Ahn, and L. Carin, "Nonuniform Frequency Sampling with Active Learning: Application to Wide-Band Frequency-Domain Modeling and Design," *IEEE Trans. Antennas Propagat*, vol. 53, no. 9, pp. 3049-3057, 2005.

[10] Z. Q. Zhao, Z. P. Nie, and L. Carin, "Active Learning Applied to RCS Computations with Nonuniform Sampling using Different Objective Functions," *IEEE Trans. Antennas Propagat*, vol. 55, no. 4, pp. 1214-1217, 2007.

[11] Per Lotstedt and Martin Nilsson, "A Minimal Residual Interpolation Method for Linear Equations with Multiple Right-Hand Sides," *SIAM Journal on Scientific Computing*, vol. 25, pp. 2126-2144, 2004.

[12] J. M. Rius, E. Ubeda, and J. Parron, "On the Testing of Magnetic Field Integral Equation with RWG Basis Functions in Method of Moments," *IEEE Trans. Antennas Propagat*, vol. 49, no. 11, pp. 1550-1554, 2001.

[13] S. M. Rao, D. R. Wilton, and A. W. Glisson, "Electromagnetic Scattering by Surfaces of Arbitrary Shape," *IEEE Trans. Antennas Propagat*, vol. 30, no. 3, pp. 409-418, 1982.

[14] Y. Saad and M. Schultz, "GMRES: A Generalized Minimal Residual Algorithm for Solving Nonsymmetric Linear Systems," *SIAM J. Sci. Stat. Comput.*, vol. 7, no. 3, pp. 856-869, 1986.

[15] V. Simoncini and D. B. Szyld, "Flexible Inner-Outer Krylov Subspace Methods," *SIAM J. Numer. Anal.*, vol. 40, no. 6, pp. 2219-2239, 2003.

[16] A. C. Woo, Helen T. G. Wang, and M. J. Schuh. "Benchmark Radar Targets for the Validation of Computational Electromagnetics Programs," IEEE Trans. Antennas Propagat, vol. 35, no. 1, pp. 84-89, 1993.

[17] S. Kurz, O. Rain, and S. Rjasanow, "The Adaptive Cross-Approximation Technique for the 3-D Boundary-Element Method," IEEE Trans. Magnetics, vol. 38, no. 2, pp. 421-424, 2002.

[18] Venkatarayalu, N. V., Yeow-Beng Gan, Kezhong Zhao, and Jin-Fa Lee, "Fast Monostatic RCS Computation in FEM Based Solvers using QR Decomposition," Antennas

and Propagation, EuCAP 2006, First European Conference on, pp. 1-5, 6-10, 2006.

[19] Shaeffer, J., "Direct Solve of Electrically Large Integral Equations for Problem Sizes to 1 M Unknowns," IEEE Trans. Antennas and Propagation, vol. 56, no. 8, pp. 2306-2313, 2008.

[20] E. K. Miller, "Using Adaptive Estimation to Minimize the Number of Samples Needed to Develop a Pattern to a Specified Uncertainty," *Applied Computational Electromagnetic Society (ACES) Journal*, vol. 17, no. 3, pp. 176-186, 2002.

[21] G. K. Carvajal, D. J. Duque, and A. J. Zozaya, "RCS Estimation of 3D Metallic Targets Using the Moment Method and Rao-Wilton-Glisson Basis Functions," *Applied Computational Electromagnetic Society (ACES) Journal*, vol. 24, no. 5, pp. 487-492, 2009.

[22] M. D. Pocock and S. P. Walker, "Iterative Solution of Multiple Right Hand Side Matrix Equations for Frequency Domain Monostatic Radar Cross Section Calculations," *Applied Computational Electromagnetic Society (ACES) Journal*, vol. 13, no. 1, pp. 4-13, 1998.

Zhiwei Liu was born in Jiangxi Province, P. R. China in 1982. He received B.S. degree in Computer Science from Nanjing Univ. of Sci. & Tech. in 2003, M.S. degree in Nanjing Institute of Electro. & Tech. in 2006, and is currently working toward the Ph.D. degree at Nanjing Univ. of Sci. & Tech. His research interests focus on theory of electromagnetic scattering and inverse scattering.

Rushan Chen (M'01) was born in Jiangsu, P. R. China. He received his B.S. and M.S. degrees from the Dept. of Radio Eng., Southeast University, in 1987 and in 1990, respectively, and his Ph.D. from the Dept. of Electronic Engineering, City University of Hong Kong in 2001. He joined the Dept. of Electrical Engineering, Nanjing Univ. of Sci. & Tech., where he became a Teaching Assistant in 1990 and a Lecturer in 1992. His research interests mainly include microwave/millimeter-wave systems, measurements, antenna, RF-integrated circuits, and computational electromagnetics.
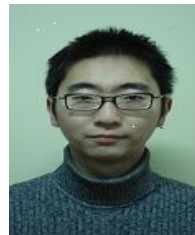
Jiaqi Chen was born in Gansu Province, P. R. China. He received the B.S. degree in Communication Engineering from Nanjing Univ. of Sci. and Tech., China, in 2005, and is currently working toward the Ph.D. degree at Nanjing Univ. of Sci. and Tech. His current research interests include computational electromagnetics, electromagnetic scattering and propagation and synthetic aperture radar imaging.

Zhen-Hong Fan was born in Jiangsu, the People's Republic of China in 1978. He received the M.Sc. and Ph.D. degrees in Electromagnetic Field and Microwave Technique from Nanjing University of Science and Technology (NJUST), Nanjing, China, in 2003 and 2007, respectively. During 2006, he was with the Center of wireless Communication in the City University of Hong Kong, Kowloon, as a Research Assistant. He is currently an associated Professor with the Electronic Engineering of NJUST. He is the author or coauthor of over 20 technical papers. His current research interests include computational electromagnetics, electromagnetic scattering, and radiation.

Reduction of Mutual coupling in Microstrip Array Antenna using Polygonal Defected Ground Structure

Ali Farahbakhsh [1], Gholamreza Moradi [2], and Shahram Mohanna[3]

[1] Technical Department, Intelligent Boards Electronic Co.
Kerman, Iran
farahbakhsh@ib-eco.com

[2] Electrical Engineering Department
Amirkabir University of Technology, Tehran, Iran
ghmoradi@aut.ac.ir

[3] Electrical Engineering Department
University of Sistan and Baluchestan, Zahedan, Iran
mohana@hamoon.usb.ac.ir

Abstract ─ The surface wave propagation is a significant problem in microstrip array antennas. Several methods have been reported to suppress the propagation of surface wave such as defected ground structure (DGS). The main problem in DGS is to determine the shape of ground slot. In this paper, a new method is proposed in which the slot is assumed to be a polygon and its shape is obtained by enhanced genetic algorithm (GA) and ant colony optimization (ACO) to have an array antenna with good gain and the least amount of return loss and mutual coupling.

Index Terms ─ ACO, GA, microstrip array antenna, mutual coupling, polygonal patch.

I. INTRODUCTION

Microstrip antennas are used widely due to their advantages such as small size, low cost, light weight, and simple manufacturing. The microstrip antennas, also, have some disadvantages such as narrow bandwidth, low radiation power, and surface wave excitation [1, 2]. When microstrip antennas are used to form an array antenna, the excitation of surface wave is significant, and it causes mutual coupling in and array antenna. Several methods are presented to reduce the mutual coupling effect [3-7] and some of them focus on surface waves suppression [6-8].

One solution to reduce the excitation of surface wave is defected ground structure [9, 10]. The DGS is implemented by cutting a portion of ground plane; therefore, the current distribution of ground plane is disturbed. So, by controlling the shape of DGS, the excitation and propagation of electromagnetic waves in the substrate layer can be controlled. As a result, surface wave and mutual coupling can be reduced by choosing an appropriate DGS shape.

Some simple shapes for DGS have been studied in the literatures and an optimal shape is obtained by changing the size and position of these simple shapes [11, 12]. In this paper, a new method is proposed in which the shape, size, and position of ground slot is obtained by enhanced GA and enhanced ACO [13].

II. ARRAY ANTENNA STRUCTURE

An array antenna with two microstrip rectangular patch antennas is used in the simulation. The layer structure includes two substrates and three conductive layers which are finite ground plane, feed line layer, and patch layer. The thicknesses of substrates are the same and equal to $0.508\,mm$. The permittivity of dielectric layer is 3.38. The array antenna is

designed at resonant frequency of $10\,GHz$ so its patches dimensions are $10\,mm$ and $7.5\,mm$. The patches are fed by proximity coupling method and the center to center distance between them are $15\,mm$. The dimensions of ground plane are $40 \times 43.5\,mm^2$. Array antenna structure and its layers structure are shown in Fig. 1-(a) and Fig. 1-(b), respectively.

(a)

(b)
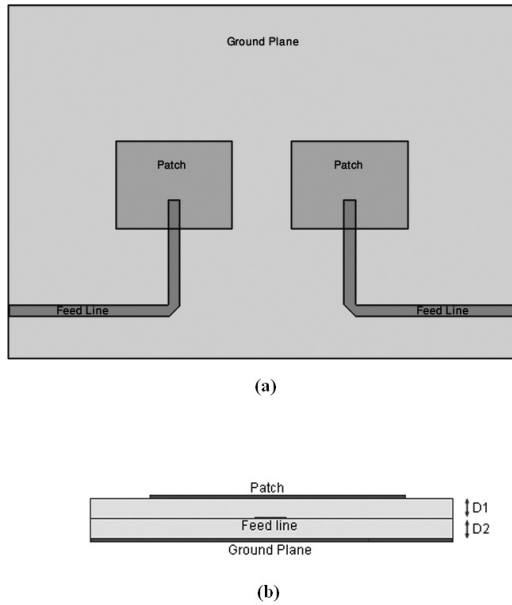
Fig. 1. Array antenna structure (a) and its layer structure (b).

III. DESIGN PROCEDURE

The DGS slot shape is considered as a non regular polygon. The number of polygon vertexes must be selected depending on the application needs. In this paper, slot shape is assumed to have 9 vertexes. Some constrains could be applied to the ground plane to simplify the design procedure. In this paper, the ground plane is assumed to be symmetric. But in array antenna with more elements, other constrains should be supposed.

The design procedure goal is to find the slot shape to have an array antenna with suitable gain and the least amount of return loss and mutual coupling. The mutual coupling in E-plane, H-plane, or both of them can be considered in the design method. But in this paper only the H-plane mutual coupling is considered in optimization procedure due to array antenna structure.

The slot shape is determined by positions of its vertexes, so the x and y values of vertexes are variables which must be optimized by enhanced GA. The x and y values of vertexes vary without any constrains in enhanced GA. So if they are connected together with a constant order, an invalid slot, that its edges intersect each other will be made as illustrated in Fig. 2.
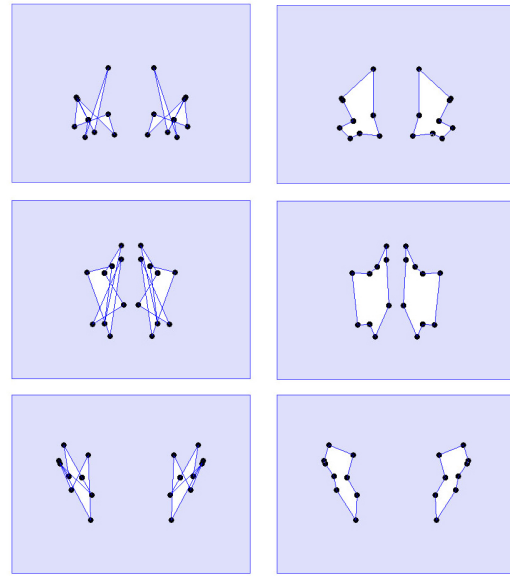
Fig. 2. Typical invalid ground planes (left column) and validated ones (right column).

To solve this problem, the correct order of vertexes connection must be found which can be achieved by enhanced ACO.

To do this, some artificial ants are generated and randomly placed on vertexes. Ants move from one vertex to another randomly and deposit trails of pheromone on their path. The ants' goal is to find the shortest path between all vertexes without intersection. In many cases, the shortest path is the path without intersection, so finding the shortest path is a good help to find the path without intersection. The ants move between vertexes with these simple rules [14]:

- Each ant moves only once through each vertex.
- Each ant must travel through all vertexes.
- Ant deposits more pheromone on shorter paths.
- Ant deposits less pheromone on the paths which have intersection with traveled paths.
- Ant prefers to travel through the path with more pheromone.

Some invalid ground planes and validated ones by ACO are illustrated in Fig. 2 and the flowchart of the mentioned method is shown in Fig. 3.
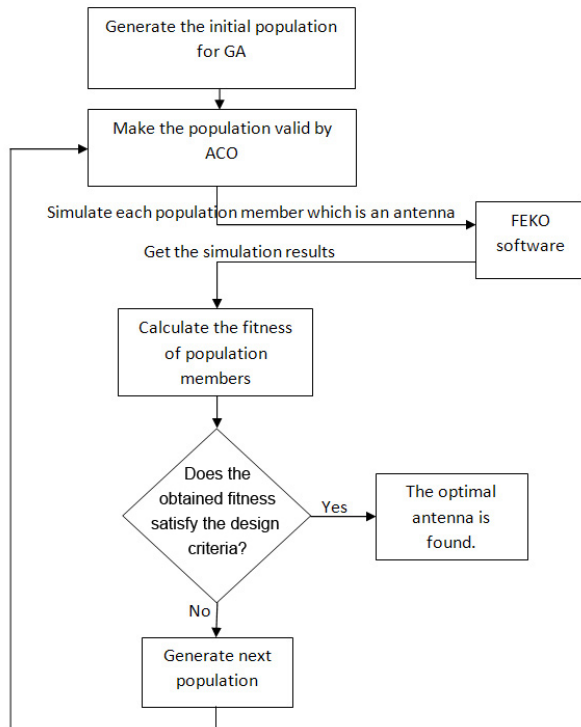
Fig. 3. Flowchart of design method.

The calculations of GA and ACO is run on the MATLAB [15] and the fitness of GA members, which are array antenna, is calculated by simulation that is based on the method of moments (MOM) [16]. Figure 4 shows an optimal array antenna which is obtained by the proposed design method.
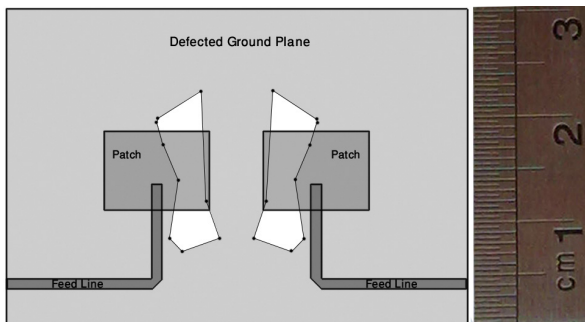
Fig. 4. The optimal array antenna with DGS.

The reflection coefficient and H-plane mutual coupling of array antenna with DGS are illustrated in Fig. 5 and are compared with those of the array

antenna without DGS. As can be seen in Fig.5 the reflection and coupling of DGS array antenna are respectively about $3\,dB$ and $4\,dB$ better than the reflection and coupling of the conventional array antenna at the resonant frequency. Also, the VSWR bandwidth of the proposed array antenna is greater than the ones for the conventional array antenna.

(a)

(b)
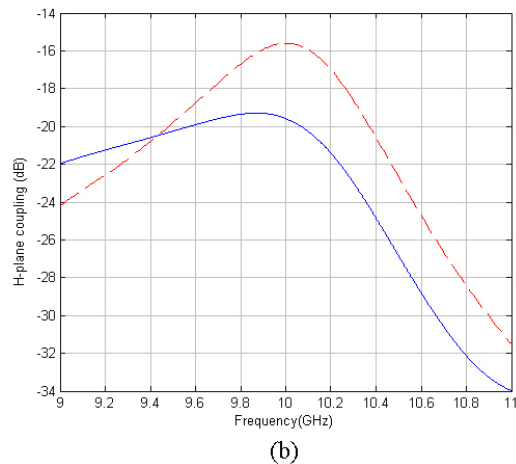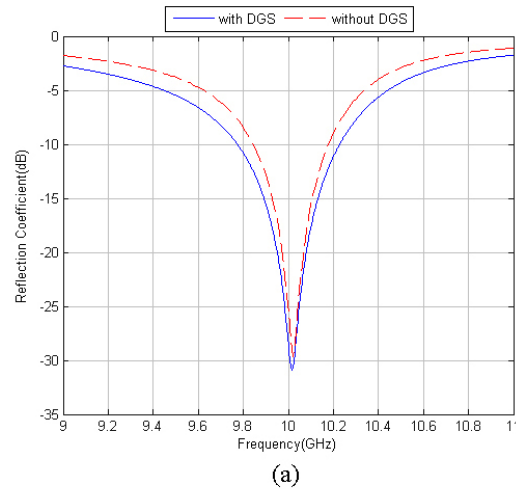
Fig. 5. Reflection coefficient (a) and the mutual coupling (b) of the array antenna with and without DGS.

The gain of the array antenna with and without DGS in $\theta = \varphi = 0°$ versus frequency is calculated and illustrated in Fig. 6. As shown in this figure, the gain and the gain bandwidth of the array antenna with DGS is improved. The dip in the gain graph shows that the radiation pattern of antenna is dependent on the frequency and the directivity of the array antenna at the resonant frequency is slightly decreased.
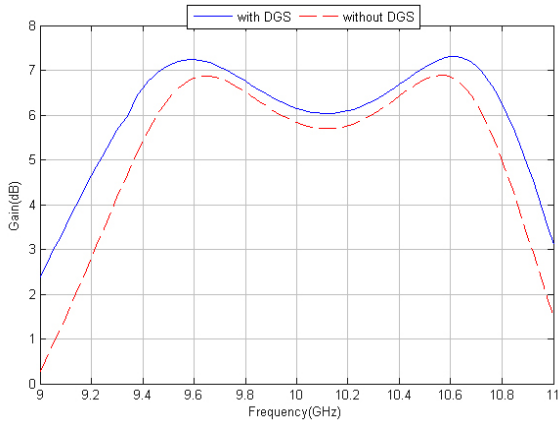
Fig. 6. Gain of array antenna with DGS and without it.

The radiation patterns of both array antennas at 10GHz are shown in Fig. 7. The back lobe level is increased in array antenna with DGS and it is due to the ground slots.
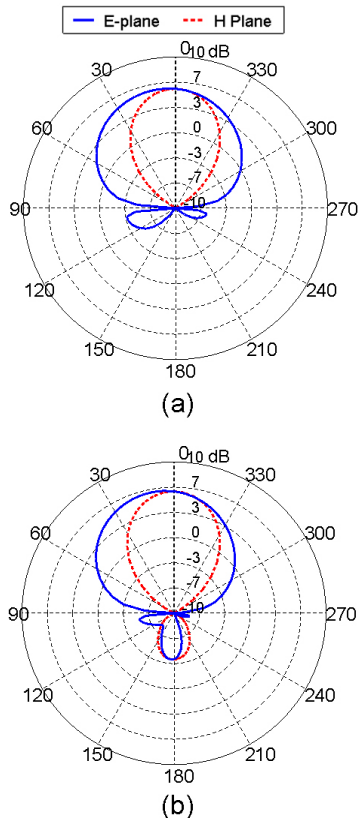
Fig. 7. Radiation pattern of array antenna without (a) and with DGS (b) at 10GHz.

The E-plane mutual coupling is not included in the optimization procedure. But it is simulated

to show the effect of DGS on E-plane coupling. The array antenna structure to simulate E-plane coupling is illustrated in Fig. 8. The center to center distance between patches is 15mm. The E-plane couplings of an array antenna with and without DGS are plotted in Fig. 9.
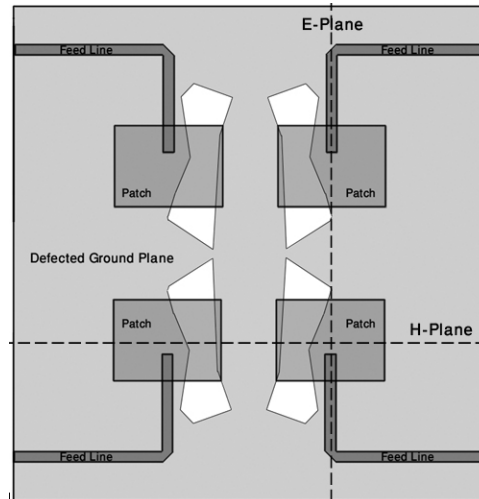
Fig. 8. Array antenna structure to obtain E-plane coupling.
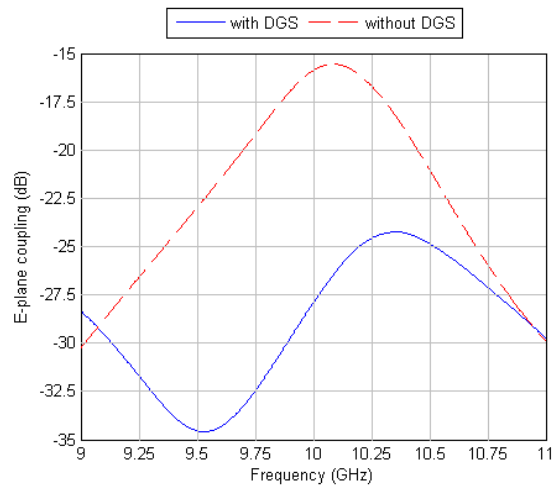
Fig. 9. E-plane mutual coupling of array antenna with and without DGS.

As shown in Fig. 9, the E-plane coupling of an array antenna with DGS is about 11dB better than coupling of array antenna without it and it shows that the DGS has a very good effect on the mutual coupling.

IV. CONCLUSION

In this paper, a new solution is proposed to control and decrease the surface wave of the array antenna. In this method, the shape of DGS is determined by enhanced GA and its results are verified by simulation. The return loss, mutual coupling, gain, and bandwidth of the proposed array antenna are improved in comparison to ordinary array antenna.

REFERENCES

[1] C. A. Balanis, "Antenna Theory: Analysis and Design," third ed., Wiley, 2005.

[2] C. A. Balanis, "Modern Antenna Handbook," John Wiley & Sons, Inc. Publication, 2008.

[3] N. Yousefzadeh, C. Ghobadi, and M. Kamyab, "Consideration of Mutual Coupling in a Microstrip Patch Array Using Fractal Elements," PIERS, vol. 66, pp. 41–49, 2006.

[4] M. Kara, "Techniques for the Computation of the Mutual Coupling between Two Rectangular Microstrip Antenna Elements with Thick Substrates," Microwave and Optical Technology Letters, vol. 16, no. 3, pp. 169-176, October 1997.

[5] A. Farahbakhsh, S. Mohanna, S. Tavakoli, and M. Oukati Sadegh, "New Patch Configurations to Reduce the Mutual Coupling in Microstrip Array Antennas," Antennas and Propagation Conference, Loughborough, England, November 2009.

[6] R. I. Macpherson, N. J. Ryan, and R. I. Macpherson, "Reducing Electromagnetic Coupling in Shielded Enclosures using a Genetic Algorithm -- Finite-Difference Time-Domain Solver," ACES Journal, vol. 18, no. 3, November 2003.

[7] W. Choi, T. K. Sarkar, O. Allen, J. Asvestas, "Approximate Compensation for Mutual Coupling in a Direct Data Domain Least Squares Approach using the In-situ Measured Element Patterns," ACES Journal, vol. 21, no. 3, November 2006.

[8] D. R. Jackson, J. T. Williams, A. K. Bhattacharyya, R. L. Smith, S. J. Buchheit, and S. A. Long, "Microstrip Patch Designs That Do Not Excite Surface Waves," IEEE Trans. Antennas Propag., vol. 41, pp. 1026–1037, Aug. 1993.

[9] R. Coccioli and T. Itoh, "Design of Photonic Band-Gap Substrates for Surface Waves Suppression," in Proc. IEEE MTT-S Symp., 1998, pp. 1259–1262.

[10] M. M. Nikolic´, A. R. Djordjevic´, and A. Nehorai, "Microstrip Antennas with Suppressed Radiation in Horizontal Directions and Reduced Coupling," IEEE Transactions on Antennas and Propagation, vol. 53, no. 11, pp. 3469-3476, November 2005.

[11] D. Ahn, J. S. Park, C. S. Kim, J. Kim, Y. Qian, and T. Itoh, "A Design of the Low-Pass Filter using the Novel Microstrip Defected Ground Structure," IEEE Trans Microwave Theory and Techniques 2001; 49: 86–93.

[12] G. Breed, "An Introduction to Defected Ground Structures in Microstrip Circuits," High Frequency Electronics, Summit Technical Media, LLC, November 2008.

[13] F. Y. Zulkifli, E. T. Rahardjo, and D. Hartanto, "Mutual Coupling Reduction using Dumbbell Defected Ground Structure for Multiband Microstrip Antenna Array," Progress In Electromagnetics Research Letters, vol. 13, pp. 29-40, 2010.

[14] A. Mahmoudian and J. Rashed-Mohassel, "Reduction of EMI and Mutual Coupling in Array Antennas by Using DGS and AMC Structures", PIERS Online, vol. 4, no. 1, 2008.

[15] A. Farahbakhsh, S. Tavakoli, and A. Seifolhosseini, "Enhancement of Genetic Algorithm and Ant Colony Optimization Techniques using Fuzzy Systems," IEEE International Advance Computing Conference, March 2009.

[16] A. Farahbakhsh and G. Moradi, "Design a Low Mutual Coupling Microstrip Array Antenna with Non Regular Polygonal Patches by GA and ACO," *IEICE Electronic Express*, vol. 7, no. 17, pp. 1271-1275, 2010.

[17] Matlab the language of technical computing, The Mathworks Inc.

[18] EM Software & Systems-S.A. (Pty) Ltd.

Ali Farahbakhsh was born in Kerman, Iran in 1985. He received his B.Sc. degree from Kerman Bahonar University, Kerman, Iran and his M.S. degree from Sistan and Baluchestan University,

Zahedan, Iran, both in Electrical Engineering, in 2007 and 2010, respectively. He has worked in the technical department of Intelligent Boards electronic company since 2007. His research interests are microstrip antenna and array antenna design.

Gholamreza Moradi was born in Shahriar, Iran in 1966. He received his B.Sc. in Electrical Communication Engineering from Tehran University, Tehran, Iran in 1989 and the M.Sc. in the same field from Iran University of Science and Technology in 1993. Then, he earned his Ph.D. degree in Electrical Engineering from Tehran Polytechnic University, Tehran, Iran in 2002. His main research interests are numerical Electromagnetics, antennas, active microwave and mm-wave circuits and systems. In 2003, he was selected as the exemplary researcher of Iranian Ministry of Road and Transportation. During 1997 till 2006, he was a faculty member at Civil Aviation Technology College, Tehran, Iran. He has published several papers in the referenced journals and the local and international conferences. Also, he authored/coauthored four books (in Persian) i.e. "Communication Transmission Lines", "Microwave Engineering", "Engineering Mathematics", and "Active Transmission Lines". The latter was selected as the book of the year of Iran in 2008. He is currently an assistant Professor of Electrical Engineering Department at Amirkabir University of Technology (Tehran Polytechnic), Tehran, Iran.

Shahram Mohanna received his B.Sc. and M.Sc. degrees in Electrical Engineering from the University of Sistan and Baluchestan, Iran and the University of Shiraz, Iran in 1990 and 1994, respectively. He then joined the University of Sistan and Baluchestan, Iran. In 2005, he obtained his Ph.D. degree in Electrical Engineering from the University of Manchester, England. As an assistant professor at the University of Sistan and Baluchestan, his areas of research include design of microwave circuits, antenna design, and applied electromagnetic. Dr. Mohanna has served as a reviewer for several journals and a number of conferences.

A DECOMPOSITION METHOD FOR THE ELECTROMAGNETIC SCATTERING FROM A CONDUCTIVE OBJECT BURIED IN A LOSSY MEDIUM

S. Makal and A. Kizilay

Department of Electronics and Communications Engineering
Yildiz Technical University, Istanbul, 34349, Turkey
smakal@yildiz.edu.tr, akizilay@yildiz.edu.tr

Abstract ─ A new numerical solution method is presented for the electromagnetic field scattered by a perfectly conducting (PEC) cylindrical object with an arbitrary cross-section buried in a lossy dielectric half-space. The dielectric half-space is considered to be flat, and the method is outlined for TM_z (horizontally) polarized incident wave. The surface equivalence principle and a decomposition method are utilized to form a set of electric field integral equations (EFIEs) for the currents on the object and the portion of the surface most strongly interacting with the object. To obtain the scattered electric field, the EFIEs are solved in the frequency domain using the method of moments (MoM).

Index Terms ─ Electromagnetic scattering, integral equations, method of moments, perturbational field.

I. INTRODUCTION

Solution of the electromagnetic scattering by buried objects has been the interest of many researches. Therefore, several techniques have been employed to obtain the scattered fields. This is because scattered field values can be used in nondestructive evaluation applications such as detecting landmines, buried pipes, near-surface geophysical exploration, and also archeological studies [1-6]. As a result, an efficient way of calculating scattered field is important for ground-penetrating radar applications.

Previously, the problem for a cylinder buried in a medium having a flat surface has been studied by many researches. For example, Uzunoglu et al.

have computed the scattered electric field from underground tunnels using a Green's function approach, and analyzed the scattered amplitude for various observation angles [7]. Kanellopoulos et al. have used the same analytical approach for conducting wires buried in earth [8]. Also, "B" approximation and Sommerfield integrals with fast evaluation methods have been the other ways to build an analytical solution for buried scatterer [9-11]. Naqvi et al. have used plane wave expansion and excitation of current on a cylinder for the scattered electric field from a conducting cylinder deeply buried in a dielectric half-space [12]. Another analytical method containing plane wave representation has been developed by Ahmed et al. [13].

In this paper, the scattered electric field from a PEC cylindrical object of arbitrary cross-section buried in a lossy half-space is computed by a new numerical solution method. The basis of the new solution method is that if an object is close to the surface, the electromagnetic fields will be nearly identical to that without the object, except within the region of finite extent near the object [14, 15]. Thus, the equivalent current on the surface will be affected only in a finite portion of the surface near the object. By using this assumption, the EFIEs for the induced current on the PEC object and the perturbation current (the difference current with object present and with object absent) on the surface are obtained. Then, the EFIEs are solved by MoM in frequency domain.

II. THEORY

The geometry of the problem is shown in

Fig.1. A TM$_z$ plane wave $\vec{E}^i$ is assumed to be incident on a cylindrical object of arbitrary cross-section buried in a two-dimensional infinite flat surface with the incidence angle of ϕ_i:

$$\vec{E}^i(x,y) = \hat{z}\, E_0\, e^{jk_0(x\cos\phi_i + y\sin\phi_i)}, \qquad (1)$$

where $k_0 = \omega\sqrt{\mu_0\varepsilon_0}$. A PEC object is located h_c below the surface. The distance between y-axis and the object axis is indicated by x_c. The flat surface is represented by S_d, and $\hat{n}_d$ is the outward unit normal vector to S_d. The object surface is represented by S_c, and $\hat{n}_c$ is the outward unit normal vector to S_c.
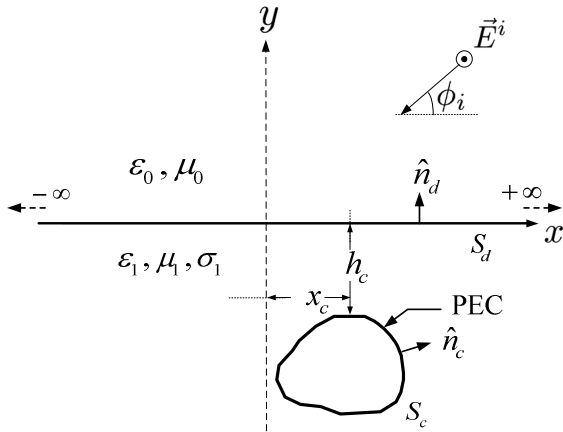
Fig. 1. The geometry of the problem.

The scattered electric field ($\vec{E}^s$) can be written as the sum of the scattered field from the PEC object and the flat surface:

$$\vec{E}^s = \vec{E}^S + \vec{E}^T. \qquad (2)$$

S and T indicate surface and object, respectively. The scattered electric field from the surface can be written as;

$$\vec{E}^S = \vec{E}^I + \vec{E}^P, \qquad (3)$$

where $\vec{E}^P$ is the perturbational field produced by the difference, or perturbation currents $\vec{J}_d^p$ and $\vec{M}_d^p$, and $\vec{E}^I$ is the field due to currents $\vec{J}^I$ and $\vec{M}^I$ on the surface which is impressed by the incident field without the object present. Therefore, the difference currents can be defined as $\vec{J}_d^p = \vec{J}^S - \vec{J}^I$ and $\vec{M}_d^p = \vec{M}^S - \vec{M}^I$. Here, $\vec{J}^S$

and $\vec{M}^S$ represent the equivalent currents on the surface. Then, substituting equation (3) into the equation (2) gives,

$$\vec{E}^s = \vec{E}^I + \vec{E}^P + \vec{E}^T. \qquad (4)$$

The unknown currents are the equivalent perturbation currents on the surface and the induced current on the object. These currents can be obtained by using the surface equivalence principle that is well-known in literature [16]. This principle has been used and explained by many researches [17, 20].

Before applying the surface equivalence principle to the original problem, the scattered electric field $\vec{E}^I$ should be obtained when the flat surface is the only scatterer. Thus, the flat surface is chosen to be the only scatterer shown in Fig. 2.
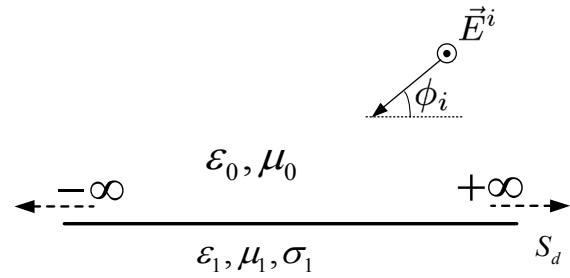
Fig. 2. The flat surface as a scatterer.

Figure 3 shows the external equivalence principle applied to the problem in Fig. 2. The whole space parameters are chosen as (ε_0, μ_0) [19, 20]. The surface is replaced by surface electric $(\vec{J}^I)$ and magnetic $(\vec{M}^I)$ currents. At any point outside the surface, the total fields are $\vec{E}$ and $\vec{H}$. The total fields are zero under the surface;

$$\vec{E}^i + \vec{E}_{ext}^I = 0 \Rightarrow S_d^-, \qquad (5)$$

$$\vec{H}^i + \vec{H}_{ext}^I = 0 \Rightarrow S_d^-. \qquad (6)$$

Here, ext means external and S_d^- represents the surface just inside S_d.

Then, the internal equivalence principle is applied in Fig. 4 to the problem shown in Fig. 2. Therefore, the whole space parameters are chosen as $(\varepsilon_1, \mu_1, \sigma_1)$ [19, 20]. The surface is replaced by surface electric $(-\vec{J}^I)$ and magnetic $(-\vec{M}^I)$ currents.
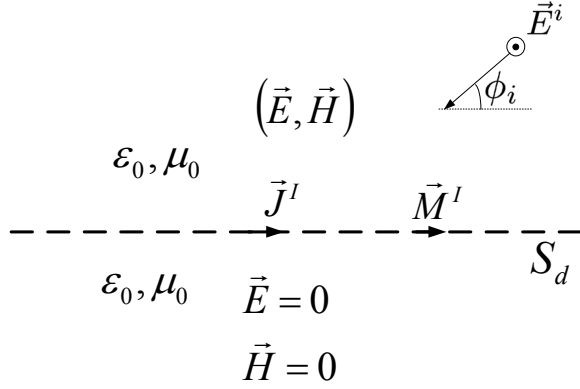
Fig. 3. External equivalence applied to the problem in Fig. 2.

The total fields are zero at any point external to S_d;

$$\vec{E}_{int}^{I} = 0 \Rightarrow S_d^{+}, \qquad (7)$$

$$\vec{H}_{int}^{I} = 0 \Rightarrow S_d^{+}. \qquad (8)$$

Here, *int* means internal, and S_d^{+} represents the surface just outside S_d.
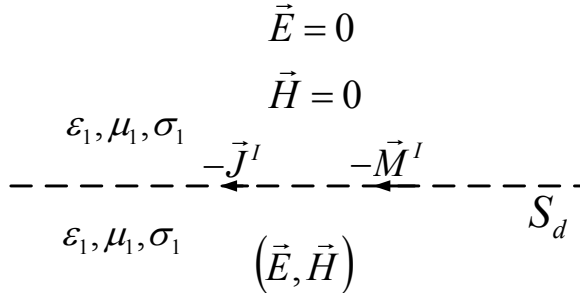
Fig. 4. Internal equivalence applied to the problem in Fig. 2.

Now, with the knowledge of scattered electric fields on the surface when there is not any object, the original problem in Fig. 1 can be solved. Initially, the external equivalence principle is applied in Fig. 5.

The total field outside the surface is the sum of the incident, and scattered field;

$$\vec{E} = \vec{E}^{i} + \vec{E}^{s}, \qquad (9)$$

$$\vec{H} = \vec{H}^{i} + \vec{H}^{s}, \qquad (10)$$

and the scattered electric field is;

$$\vec{E}^{s} = \vec{E}_{ext}^{I} + \vec{E}_{ext}^{P}. \qquad (11)$$

In Fig. 5, $\vec{J}_d^{p}$ and $\vec{M}_d^{p}$ are the perturbation currents;
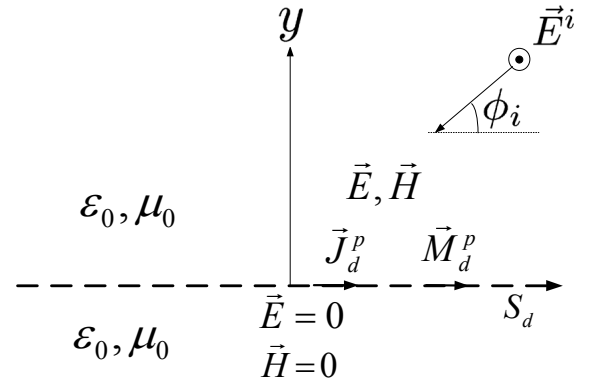
Fig. 5. The external equivalence principle applied to the problem in Fig. 1.

$$\vec{J}_d^{p} = \hat{n}_d \times \vec{H}(S_d^{+}), \qquad (12)$$

$$\vec{M}_d^{p} = \vec{E}(S_d^{+}) \times \hat{n}_d. \qquad (13)$$

The total field is zero just inside the surface S_d;

$$\vec{E}^{s} = -\vec{E}^{i} \Rightarrow S_d^{-}. \qquad (14)$$

Then, the field caused by perturbation currents becomes;

$$\vec{E}_{ext}^{P} = -\vec{E}_{ext}^{I} - \vec{E}^{i} \Rightarrow S_d^{-}. \qquad (15)$$

Now, equation (5) is used in equation (15), then the value of the perturbation field on S_d^{-} becomes,

$$\vec{E}_{ext}^{P}\left(\vec{J}_d^{p}, \vec{M}_d^{p}\right) = 0 \Rightarrow S_d^{-}. \qquad (16)$$

Then, the internal equivalence principle is applied in Fig. 6 to the problem shown in Fig. 1.
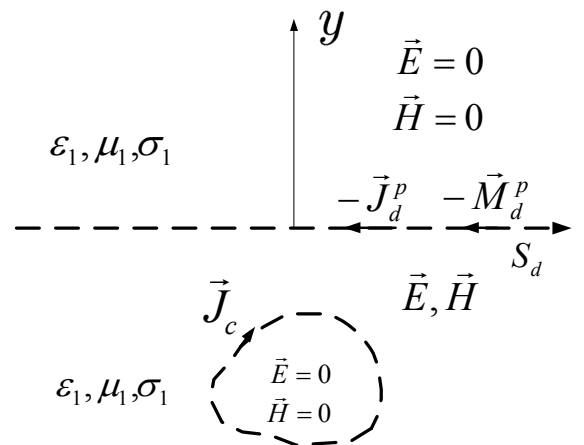
Fig. 6. The internal equivalence principle applied to the problem in Fig. 1.

There is no incident wave, and the total fields under the surface contain just the scattered fields;

$$\vec{E} = \vec{E}^s, \tag{17}$$

$$\vec{H} = \vec{H}^s. \tag{18}$$

The scattered electric field is expressed;

$$\vec{E}^s = \vec{E}_{int}^I + \vec{E}_{int}^P + \vec{E}^T \tag{19}$$

The total electric field is zero outside S_d:

$$\vec{E}_{int}^P\left(-\vec{J}_d^p, -\vec{M}_d^p\right) + \vec{E}^T\left(\vec{J}_c\right) = -\vec{E}_{int}^I \Rightarrow S_d^+. \tag{20}$$

After equation (7) is used in equation (20), the scattered electric field on S_d^+ becomes,

$$\vec{E}_{int}^P\left(-\vec{J}_d^p, -\vec{M}_d^p\right) + \vec{E}^T\left(\vec{J}_c\right) = 0 \Rightarrow S_d^+. \tag{21}$$

The total field is also zero inside S_c,

$$\vec{E}_{int}^P\left(-\vec{J}_d^p, -\vec{M}_d^p\right) + \vec{E}^T\left(\vec{J}_c\right) = -\vec{E}_{int}^I \Rightarrow S_c^-, \tag{22}$$

where S_c^- represents the surface just inside S_c and $\vec{J}_c$ is the equivalent current on the object;

$$\vec{J}_c = \hat{n}_c \times \vec{H}(S_c^+). \tag{23}$$

$\vec{E}_{int}^I$ on S_c^- is the electric field value on the object points when the object is absent. Therefore, this electric field can be obtained analytically in a closed form as;

$$\vec{E}_{int}^I = \hat{z}\, T\, E_0 e^{jk_1(x\sin\phi_t + y\cos\phi_t)}. \tag{24}$$

Here, $k_1 = \omega\sqrt{\mu_1\varepsilon_c}$ and $\varepsilon_c = \varepsilon_1\left(1 - j\dfrac{\sigma_1}{\omega\varepsilon_1}\right)$. The transmission coefficient indicated by T;

$$T = \frac{2\eta_1\cos\phi_i}{\eta_1\cos\phi_i + \eta_0\cos\phi_t}, \tag{25}$$

where $\eta_0 = \sqrt{\mu_0/\epsilon_0}$ and $\eta_1 = \sqrt{\mu_1/\epsilon_c}$ are the intrinsic impedance of free and lossy half-space, respectively. Here, ϕ_t is the transmission angle and defined by Snell's law;

$$\phi_t = \sin^{-1}\left(\sqrt{\frac{\varepsilon_0\mu_0}{\varepsilon_c\mu_1}}\cos\phi_i\right). \tag{26}$$

In other words, there are three equations (16), (21), and (22) to be solved by using MoM and the three unknown currents to calculate the scattered field.

The electric field is expressed in terms of electric and magnetic potential functions [17], and equations (16), (21), and (22) can be rewritten as;

$$-j\omega A_z^{ext}\left(\vec{J}_d^p\right) - \frac{1}{\varepsilon_0}\left[\nabla \times \vec{F}^{ext}\left(\vec{M}_d^p\right)\right]_z = 0, \ S_d^-, \tag{27}$$

$$-j\omega A_z^{int}\left(-\vec{J}_d^p\right) - j\omega A_z^{int}\left(\vec{J}_c\right)$$
$$-\frac{1}{\varepsilon_c}\left[\nabla \times \vec{F}^{int}\left(-\vec{M}_d^p\right)\right]_z = 0, \ S_d^+, \tag{28}$$

$$-j\omega A_z^{int}\left(-\vec{J}_d^p\right) - j\omega A_z^{int}\left(\vec{J}_c\right)$$
$$-\frac{1}{\varepsilon_c}\left[\nabla \times \vec{F}^{int}\left(-\vec{M}_d^p\right)\right]_z = -\left[\vec{E}_{int}^I\right]_z, \ S_c^-, \tag{29}$$

where $\vec{A}$ and $\vec{F}$ denote the magnetic and electric vector potential, respectively. They are given by the following line integrals:

$$\vec{A}(\vec{\rho}) = \frac{\mu}{4j}\int_{C_j} \vec{J}(\vec{\rho}')H_0^{(2)}\left(k|\vec{\rho} - \vec{\rho}'|\right)dl', \tag{30}$$

$$\vec{F}(\vec{\rho}) = \frac{\varepsilon}{4j}\int_{C_m} \vec{M}(\vec{\rho}')H_0^{(2)}\left(k|\vec{\rho} - \vec{\rho}'|\right)dl', \tag{31}$$

where $\vec{\rho}'$ represents the source points, and $\vec{\rho}$ is a two-dimensional position vector. The contours over $\vec{J}$ and $\vec{M}$ are C_j and C_m, respectively.

Three equations (27, 28, 29) are solved numerically using MoM for three unknown surface currents $(\vec{J}_d^p, \vec{M}_d^p, \vec{J}_c)$. The currents on the surfaces of S_d and S_c are approximated by linear segments:

$$\vec{J}_c(\vec{\rho}') = \hat{z}\sum_{i=1}^{N_c} I_i^c P_i^c(\vec{\rho}'), \tag{32}$$

$$\vec{J}_d^p(\vec{\rho}') = \hat{z}\sum_{i=1}^{N_d} I_i^d P_i^d(\vec{\rho}'), \tag{33}$$

$$\vec{M}_d^p(\vec{\rho}') = \sum_{i=1}^{N_d} \hat{\tau}_i K_i^d P_i^d(\vec{\rho}'), \tag{34}$$

where N_c and N_d are the numbers of segments on S_c and S_d, respectively. I_i^c and I_i^d are the unknown values of electric current on the ith segment of S_c and S_d, respectively. K_i^d denotes the value of the magnetic current on the ith segment of N_d. The unit vector in the

circumferential direction tangent to the ith segment of S_d is denoted by $\hat{\tau}_i$, and the unit vector in the z-direction is denoted by $\hat{z}$. Pulse functions (P^c, P^d) are chosen as the expansion functions.

Equations (27), (28), and (29) can be rewritten using equations (32), (33), and (34);

$$-\frac{\omega\mu_0}{4}\sum_{i=1}^{N_d} I_i^d \int_{C_{di}} H_0^{(2)}\left(k_0\left|\vec{\rho}-\vec{\rho}'\right|\right)dl'$$

$$-\frac{jk_0}{4}\sum_{i=1}^{N_d} K_i^d \int_{C_{di}} H_1^{(2)}\left(k_0\left|\vec{\rho}-\vec{\rho}'\right|\right) \qquad (35)$$

$$\times\frac{\hat{n}_i^d\cdot\left(\vec{\rho}-\vec{\rho}'\right)}{\left|\vec{\rho}-\vec{\rho}'\right|}dl' = 0, \quad S_d^-,$$

$$\frac{\omega\mu_1}{4}\sum_{i=1}^{N_d} I_i^d \int_{C_{di}} H_0^{(2)}\left(k_1\left|\vec{\rho}-\vec{\rho}'\right|\right)dl'$$

$$-\frac{\omega\mu_1}{4}\sum_{i=1}^{N_c} I_i^c \int_{C_{ci}} H_0^{(2)}\left(k_1\left|\vec{\rho}-\vec{\rho}'\right|\right)dl'$$

$$+\frac{jk_1}{4}\sum_{i=1}^{N_d} K_i^d \int_{C_{di}} H_1^{(2)}\left(k_1\left|\vec{\rho}-\vec{\rho}'\right|\right) \qquad (36)$$

$$\times\frac{\hat{n}_i^d\cdot\left(\vec{\rho}-\vec{\rho}'\right)}{\left|\vec{\rho}-\vec{\rho}'\right|}dl' = 0, \quad S_d^+,$$

$$\frac{\omega\mu_1}{4}\sum_{i=1}^{N_d} I_i^d \int_{C_{di}} H_0^{(2)}\left(k_1\left|\vec{\rho}-\vec{\rho}'\right|\right)dl'$$

$$-\frac{\omega\mu_1}{4}\sum_{i=1}^{N_c} I_i^c \int_{C_{ci}} H_0^{(2)}\left(k_1\left|\vec{\rho}-\vec{\rho}'\right|\right)dl'$$

$$+\frac{jk_1}{4}\sum_{i=1}^{N_d} K_i^d \int_{C_{di}} H_1^{(2)}\left(k_1\left|\vec{\rho}-\vec{\rho}'\right|\right) \qquad (37)$$

$$\times\frac{\hat{n}_i^d\cdot\left(\vec{\rho}-\vec{\rho}'\right)}{\left|\vec{\rho}-\vec{\rho}'\right|}dl' = -E_{int}^I, \quad S_c^-,$$

where $H_0^{(2)}$ is the zeroth-order Hankel function of the second kind, $H_1^{(2)}$ is the first-order Hankel function of the second kind, C_d and C_c are the contours representing of S_d and S_c, respectively. Then, pulse weighting functions are used to transform these EFIEs to linear equations. These linear equations are solved to obtain the unknown

currents, and the far scattered field can be computed using only $\vec{J}_d^p$ and $\vec{M}_d^p$:

$$E_z^s = -\frac{\omega\mu_0}{4}\sqrt{\frac{2j}{k_0\pi}}\frac{e^{-jk_0\rho}}{\sqrt{\rho}}\sum_{i=1}^{N_d} I_i^d e^{-jk_0\left(x'\cos\phi_s+y'\sin\phi_s\right)}\Delta_i^d$$

$$+\frac{jk_0}{4}\sqrt{\frac{2j}{k_0\pi}}\frac{e^{-jk_0\rho}}{\sqrt{\rho}}\sum_{i=1}^{N_d} K_i^d e^{-jk_0\left(x'\cos\phi_s+y'\sin\phi_s\right)}\Delta_i^d,$$

$$(38)$$

where ϕ_s is the scattering angle, and Δ^d is the length of the segment on S_d.

III. NUMERICAL RESULTS

If it is not indicated otherwise; for all MoM solutions, the value of 20 points per free-space wavelength (λ_0) is used to represent the currents on the object and the surface. The object is chosen to be a PEC cylinder with circular cross-section of radius r_a (Fig. 7), and the perturbation currents' behaviors are investigated in Fig. 8 to validate the assumption that the equivalent current on the surface will be affected only in a finite portion of the surface near the object. As expected, when the object is buried deeper, the perturbation currents spread along the surface. So, it is important to select the truncation width (wl) carefully.
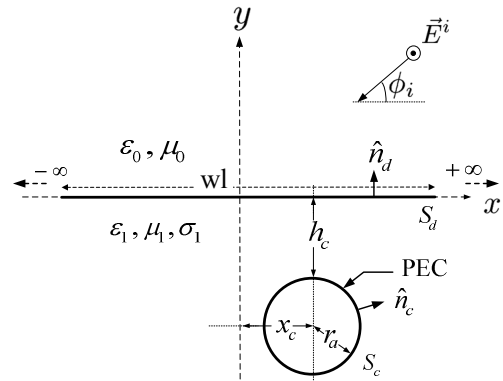

Fig. 7. The geometry used for the numerical results.

After establishing the validity of our assumption, it is also necessary to determine the accuracy of the method. This can be done by choosing the space parameters under the flat surface as (ε_0, μ_0). Thus, the scattered field is expected to behave like a PEC cylinder. The

scattered E-field is first solved by the decomposition method, and then by the analytical method [21]. Then, these two results are compared in Fig. 9. It is seen that if the truncation width is chosen to be sufficiently long, the decomposition method gives very accurate results.

The root-mean square error (E_{RMS}) between the decomposition method and the analytical solution is calculated by using;

(a)

(b)
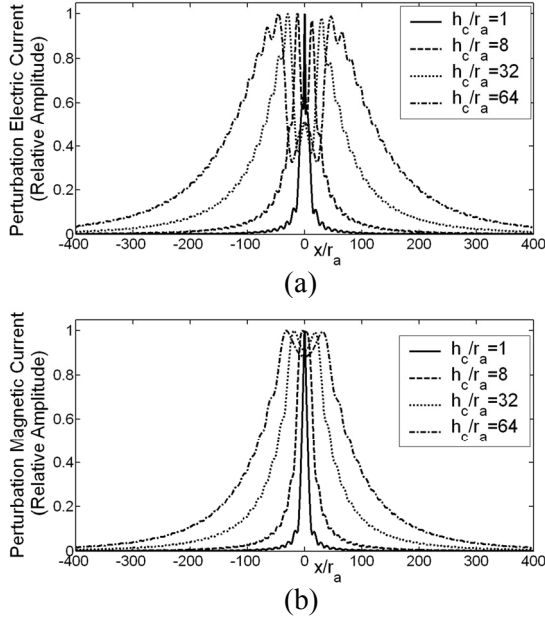
Fig. 8. Perturbation (a) electric and (b) magnetic currents on the flat surface for f=1 GHz, $\phi_i = 20°$, $r_a = 0.01$ m, $x_c / r_a = 0.0$, $\varepsilon_1 = 15\varepsilon_0$ F/m, $\mu_1 = \mu_0$ H/m, and $\sigma_1 = 0.01$ Sm^{-1}.

(a)

(b)
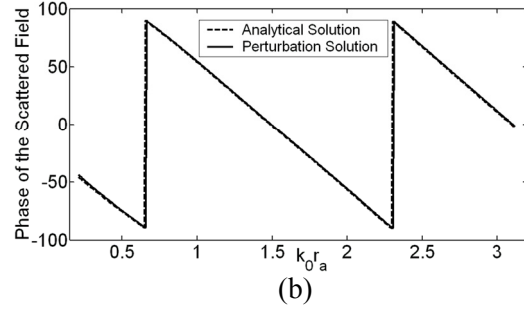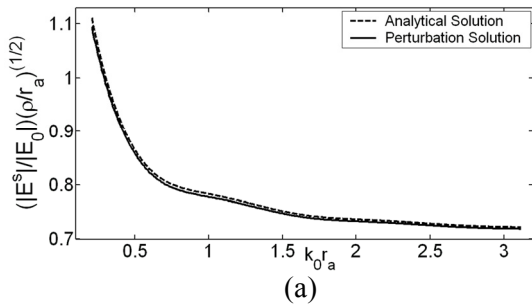
Fig. 9. Scattered field (a) normalized amplitude and (b) phase for $r_a = 0.01$ m, $\phi_i = 90°$, $h_c / r_a = 1.0$, $x_c / r_a = 0.0$, wl$/ r_a = 500$, $\varepsilon_1 = \varepsilon_0$ F/m, and $\mu_1 = \mu_0$ H/m.

$$E_{RMS}\left(\%\right) = \sqrt{\frac{\left|E^A - E^P\right|^2}{\left|E^A\right|^2}}, \qquad (39)$$

where E^A and E^P, show analytical and decomposition solutions, respectively. The number of points on the cylinder is chosen to be 50. Then, the RMS error is calculated and shown in Fig. 10. It is seen that $E_{RMS}(\%) \leq 0.227\, e^{-0.0033\,\text{wl}/h_c}$, so the solution converges exponentially with respect to wl/h_c and the solution becomes more accurate for increasing truncation width.
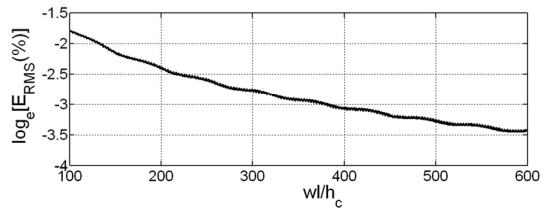
Fig. 10. The approximation difference for $r_a = 0.01$ m, $\phi_i = 90°$, $h_c / r_a = 1.0$, $x_c / r_a = 0.0$, $\varepsilon_1 = \varepsilon_0$ F/m, and $\mu_1 = \mu_0$ H/m.

To validate the decomposition method for lossy half-space, the solution is compared to the results in [8] including Green's function approach. The comparison is shown in Fig. 11. Increasing the truncation width makes the solution to converge the result of Green's function approach.
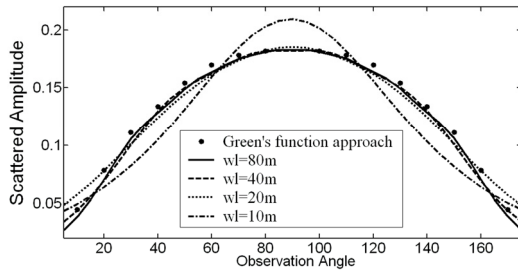
Fig. 11. Scattered amplitude from a cylindrical scatterer with circular cross-section for $r_a = 0.3$ m, $h_c = 1.7$ m, $x_c / r_a = 0.0$, $\varepsilon_1 = 15\varepsilon_0$ F/m, $\mu_1 = \mu_0$ H/m, $\phi_i = 60^\circ$, $f = 30$ MHz, and $\sigma_1 = 0.01$ Sm^{-1}.

After determining the method's accuracy, the object is chosen as a cylinder with elliptical cross-section in Fig. 12. The effect of the incident angle is noticeable on the scattered amplitude. There is a reduction of the magnitude of the scattered field as the incident angle deviates from 90°. Also, the scattered energy is concentrated around a scattering angle of 90° even for a very small incident angle.
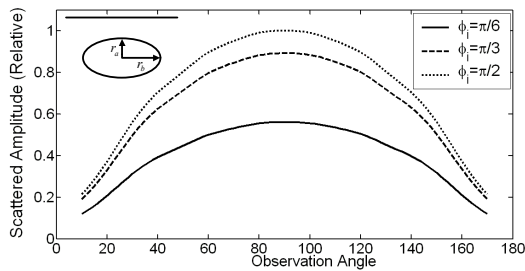
Fig. 12. Relative scattered amplitude from a cylindrical scatterer with elliptical cross-section for $r_a = 0.02$ m, $r_b = 0.01$ m, $h_c / r_b = 1.0$, $x_c / r_a = 0.0$, $\varepsilon_1 = 15\varepsilon_0$ F/m, $\mu_1 = \mu_0$ H/m, and $\sigma_1 = 0.01$ Sm^{-1}.

IV. CONCLUSION

The scattered electric field from a conducting cylinder buried in a lossy medium having an infinite flat surface excited by a TM$_z$ polarized electromagnetic wave has been solved by a new numerical solution method. The validity of perturbation assumption is shown by calculating the perturbation currents on the flat surface. It is shown that the perturbation currents on the flat surface become negligible except within the region of finite extent near the object for lossy medium. Also, to investigate the accuracy of the method, the medium parameters are taken to be space parameters. It is seen that the method is very accurate. A detailed study of short-pulse scattering from objects buried in a lossy half-space will be undertaken in the future.

REFERENCES

[1] T. Dogaru, L. Carin, "Time-Domain Sensing of Targets Buried under a Rough Air-Ground Interface," *IEEE Transactions on Antennas and Propagation*, vol. 46, no. 3, pp. 360-372, 1998.

[2] Y. Altuncu, I. Akduman, and A. Yapar, "Detecting and Locating Dielectric Objects Buried under a Rough Interface," *IEEE Geoscience and Remote Sensing Letters*, vol. 4, no. 2, pp. 251-255, 2007.

[3] G. L. Plett, T. Doi, and D. Torrieri, "Mine Detection using Scattering Parameters," *IEEE Transactions on Neural Networks*, vol. 8, no. 6, pp. 1456-1467, 1997.

[4] W. Chien and C-C. Chiu, "Cubic-Spline Expansion with GA for Half-Space Inverse Problems," *Applied Computational Electromagnetic Society (ACES) Journal*, vol. 20, no. 2, pp. 136-143, 2005.

[5] C. Huang, C. Chen, C. Chiu, and C. Li, "Reconstruction of the Buried Homogenous Dielectric Cylinder by FDTD and Asynchronous Particle Swarm Optimization," *Applied Computational Electromagnetic Society (ACES) Journal*, vol. 25, no. 8, pp. 672-681, 2010.

[6] K. P. Prokopidis and T. D. Tsiboukis, "Modeling of Ground-Penetrating Radar for Detecting Buried Objects in Dispersive Soils," *Applied Computational Electromagnetic Society (ACES) Journal*, vol. 22, no. 2, pp. 287-294, 2007.

[7] N. K. Uzunoglu and J. D. Kanellopoulos, "Scattering From Underground Tunnels,"

Journal of Physics A: Mathematical and General, vol. 15, no. 2, pp. 459-471, 1982.

[8] J. D. Kanellopoulos and N. E. Buris, "Scattering From Conducting Cylinders Embedded in a Lossy Medium," *International Journal of Electronics*, vol. 57, no. 3, pp. 391-401, 1984.

[9] D. A. Hill, "Electromagnetic Scattering by Buried Objects of Low Contrast," *IEEE Transactions on Geoscience and Remote Sensing*, vol. 26, no. 2, pp. 195-203, 1988.

[10] T. J. Cui and W. C. Chew, "Efficient Evaluation of Sommerfeld Integrals for TM Wave Scattering by Buried Objects," *Journal of Electromagnetic Waves and Applications*, vol. 12, no. 5, pp. 607-657, 1998.

[11] T. J. Cui, W. C. Chew, and W. Hong, "New Approximate Formulations for EM Scattering by Dielectric Objects," *IEEE Transactions on Antennas and Propagation*, vol. 52, no. 3, pp. 684-692, 2004.

[12] Q. A. Naqvi, A. A. Rizvi, and Z. Yaqoob, "Scattering of Electromagnetic Waves from a Deeply Buried Circular Cylinder," *Progress in Electromagnetics Research*, vol. 27, pp. 37-59, 2000.

[13] S. Ahmed and Q. A. Naqvi, "Electromagnetic Scattering from a Perfect Electromagnetic Conductor Cylinder Buried in a Dielectric Half-Space," *Progress in Electromagnetics Research*, vol. 78, pp. 25-38, 2008.

[14] A. Kizilay, *A Perturbation Method for Transient Multipath Analysis of Electromagnetic Scattering from Objects above Periodic Surfaces*, Ph.D. Dissertion, Michigan State University, 2000.

[15] A. Kizilay and E. Rothwell, "Efficient Computation of Transient TM Scattering from a Cylinder above an Infinite Periodic Surface," *Journal of Electromagnetic Waves and Applications*, vol. 13, no. 7, pp. 943-961, 1999.

[16] R. F. Harrington, *Time Harmonic Electromagnetic Fields*, McGraw-Hill, New York, 1961.

[17] A. W. Glisson, "An Integral Equation for Electromagnetic Scattering from Homogeneous Dielectric Bodies," *IEEE Transactions on Antennas and Propagation*, vol. 32, no. 2, pp. 173-175, 1984.

[18] A. J. Booysen, "A Physical Interpretation of the Equivalence Theorem," *IEEE Transactions on Antennas and Propagation*, vol. 48, no. 8, pp. 1260-1262, 2000.

[19] E. Arvas, M. Ross, and Y. Qian, "TM Scattering from a Conducting Cylinder of Arbitrary Cross-Section Covered by Multiple Layers of Lossy Dielectrics," *IEE Proceedings H*, vol. 135, no. 4, pp. 226-230, 1988.

[20] E. Arvas, M. Ross, and Y. Qian, "TE Scattering from a Conducting Cylinder of Arbitrary Cross-section Covered by Multiple Layers of Lossy Dielectrics," *IEE Proceedings H*, vol. 136, no. 6, pp. 425-430, 1989.

[21] C. A. Balanis, *Advanced Engineering Electromagnetics*, John WileySons, 1989.

Senem Makal was born in Tunceli, Turkey, in 1983. She received B.Sc. and M.Sc. degrees in Electronics and Communications Engineering from Yildiz Technical University in 2005 and 2007. She is a research assistant in the Department of Electronics and Communications Engineering at Yildiz Technical University. Her main research interests include electromagnetic wave theory, electromagnetic scattering, artificial neural networks, and radar target identification.

Ahmet Kizilay was born in Istanbul, Turkey, in 1969. He received B.Sc. degree in Electronics and Communications Engineering from Yildiz University in 1990, M.Sc. and Ph.D. degrees in Electrical Engineering from Michigan State University in 1994 and 2000. In July 2001, he joined the Department of Electronics and Communications Engineering at Yildiz Technical University, where he is currently working as Associate Professor. His main research interests include time domain electromagnetic scattering, electromagnetic wave theory, and fiber optics.

A New Ultra Wideband Fractal Monopole Antenna

Abolfazl Azari

Member of Young Researchers Club
Gonabad Branch, Islamic Azad University, Gonabad, Iran
azari@ieee.org

Abstract — Ultra wideband antennas are used greatly in commercial and military communication systems. A reduction in physical size and multi-band capability are very important in the design of ultra wideband antennas. The use of fractal geometry in antenna design provides a good method for achieving the desired miniaturization and multi-band properties.

In this paper, a compact, multi-band, and broad-band antenna based on new fractal geometry is designed, simulated, and measured. The proposed design is achieved by applying the 2nd iteration of a new fractal geometry to a wire monopole antenna. A numerical electromagnetics simulation is performed using SuperNEC electromagnetic simulator software. The results show that the proposed antenna can be used for 6 GHz – 30 GHz frequency range. Radiation patterns are also studied.

Index Terms — Bandwidth, fractals, fractal antenna, ultra wideband.

I. INTRODUCTION

One of the essential requirements of wireless systems is a low profile and multi-band antenna. Ultra wideband (UWB) wireless systems require antennas with more bandwidth and smaller dimensions. A fractal geometry is a very good solution to fabricate these antennas. Traditional UWB antennas are based on quarter-wavelength elements, which require different antenna elements for different frequency bands. Applying fractals to antenna elements allows for smaller size, multi-band, and broad-band properties. This is the cause of widespread research on fractal antennas in recent years [1-4].

Fractals have self-similar shapes and can be subdivided in parts such that each part is a reduced size copy of the whole. The self-similarity of fractals makes it possible to design antennas with UWB performance. Fractal geometries have complex and convoluted shapes such that these discontinuities increase bandwidth and the effective radiation of antennas. Also, the space-filling property of fractals leads to curves which have long electrical length but fit into a compact physical volume. This property can be utilized to miniaturize antenna elements [5-10].

Several wire antenna configurations based on fractal geometries have been investigated including Koch, Minkowski, Hilbert, and fractal tree antennas in recent years. These antennas have been simulated using the moment method, as well as fabricated and measured. The simulation and experimental results of these antennas are available in literature to date.

The Koch fractal curve is one of the most well-known fractal shapes. In this paper, a new fractal geometry that looks similar to the Koch fractal geometry is presented. By applying this fractal generator to a wire monopole antenna, we have achieved an ultra wideband antenna. The huge bandwidth is the main advantage of this fractal antenna over conventional fractal antennas.

The moment method based electromagnetic simulator SuperNEC has been used for the design and simulation of the proposed antenna. According to the results, this new fractal monopole antenna is multi-band, and broad-band

and is applicable between 6 GHz - 30 GHz frequency range. Also, the radiation patterns are studied at multi frequencies.

This paper is arranged in four sections. Design of proposed antenna is discussed in Section II. Simulated and measured results are presented in Section III and the conclusions are summarized in Section IV.

II. ANTENNA STRUCTURE

The most well-known fractal antenna is Koch antenna such that the various types of it, are used greatly in telecommunication systems. In initial process of this project, many designs and simulations are performed over fractal antennas. The various types of fractal antennas are considered and finally a new fractal shape is introduced because of its good performances in bandwidth and radiation patterns.

The geometric configuration of this new fractal curve starts with a straight line, called the initiator, which is shown in Fig. 1 (n=0). This is partitioned into four equal parts, and the two centric segments are replaced with four others of the same length with the indentation angle $\theta = 60°$ which is shown in Fig. 1 (n=1). This is the first iterated version of the new fractal geometry and is called the generator. The process is repeated in the 2nd iteration which is shown in Fig. 1 (n=2).
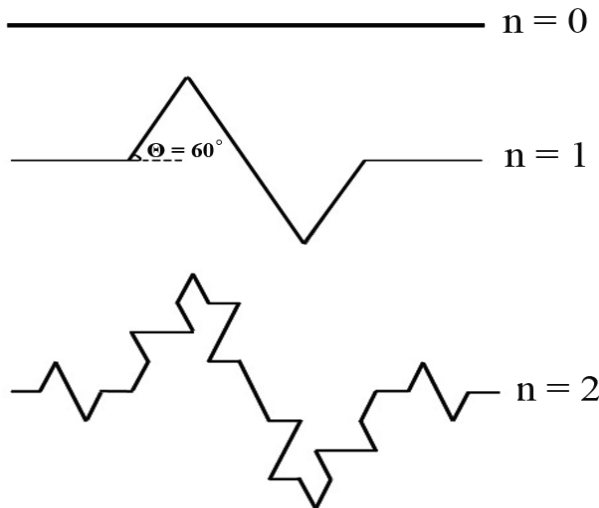
Fig. 1. Iterations of the proposed fractal geometry.

Each segment in the first iteration (generator) is ¼ the length of the initiator. There are six such

segments. Thus for the nth iteration, the length of the curve is $\left(\frac{6}{4}\right)^n$.

An iterative function system (IFS) can be defined to generate the generator. A 3×3 matrix must be defined for each segments of the generator. The length of each segment is a quarter of straight line and the indentation angle is 60°. Thus, the transformations to achieve the segments of the generator are:

$$W_1 = \begin{bmatrix} \frac{1}{4} & 0 & 0 \\ 0 & \frac{1}{4} & 0 \\ 0 & 0 & 1 \end{bmatrix},$$

$$W_2 = \begin{bmatrix} \frac{1}{4}\cos 60° & -\frac{1}{4}\sin 60° & \frac{1}{4} \\ \frac{1}{4}\sin 60° & \frac{1}{4}\cos 60° & 0 \\ 0 & 0 & 1 \end{bmatrix},$$

$$W_3 = \begin{bmatrix} \frac{1}{4}\cos 60° & \frac{1}{4}\sin 60° & \frac{3}{8} \\ -\frac{1}{4}\sin 60° & \frac{1}{4}\cos 60° & \frac{1}{4}\sin 60° \\ 0 & 0 & 1 \end{bmatrix},$$

$$W_4 = \begin{bmatrix} \frac{1}{4}\cos 60° & \frac{1}{4}\sin 60° & \frac{1}{2} \\ -\frac{1}{4}\sin 60° & \frac{1}{4}\cos 60° & 0 \\ 0 & 0 & 1 \end{bmatrix},$$

$$W_5 = \begin{bmatrix} \frac{1}{4}\cos 60° & -\frac{1}{4}\sin 60° & \frac{5}{8} \\ \frac{1}{4}\sin 60° & \frac{1}{4}\cos 60° & -\frac{1}{4}\sin 60° \\ 0 & 0 & 1 \end{bmatrix},$$

$$W_6 = \begin{bmatrix} \frac{1}{4} & 0 & \frac{3}{4} \\ 0 & \frac{1}{4} & 0 \\ 0 & 0 & 1 \end{bmatrix}. \quad (1)$$

The generator is then achieved as:

$$W(A) = W_1(A) \cup W_2(A) \cup W_3(A) \cup W_4(A) \cup W_5(A) \cup W_6(A) \quad (2)$$

This process can be repeated for higher iterations of this fractal geometry. The similarity

dimension of this geometry can be calculated as:

$$D = \frac{\log 6}{\log 4} = 1.29248 \ . \tag{3}$$

This is due to the observation that at each iteration there are six equal copies of the original geometry that are scaled down by a factor of 4. Therefore, this amount is more than the similarity dimension of Koch geometry.

The proposed design is based on a loaded 2nd iteration of the new generator to a wire monopole antenna. If the length of monopole is assumed to be "X", by applying the 2nd iteration of this generator, the length will be $X \times (\frac{6}{4})^2$.

In this paper, we have supposed the length of monopole is 3.2 cm and 1 mm in diameter. Therefore, the length of the fractal curve is $3.2 \times (\frac{6}{4})^2 = 7.2 cm$.

The structure of this fractal monopole antenna is shown in Fig. 2.
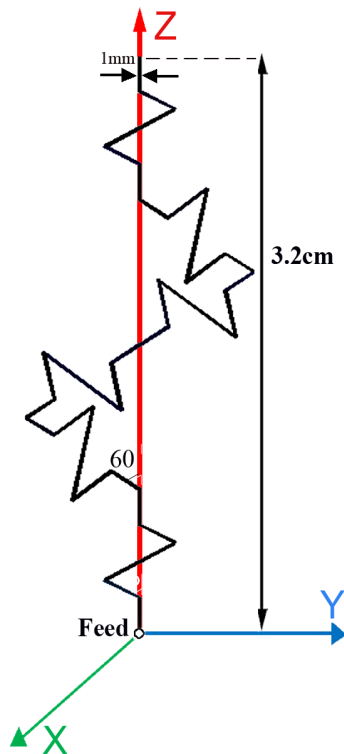
Fig. 2. Antenna structure.

The fractal antenna is made by copper and vertically installed above a ground plane which is from aluminum metal. The proposed structure has

a physical dimensions of 32 × 16 mm². The fabricated fractal monopole antenna is shown in Fig. 3.
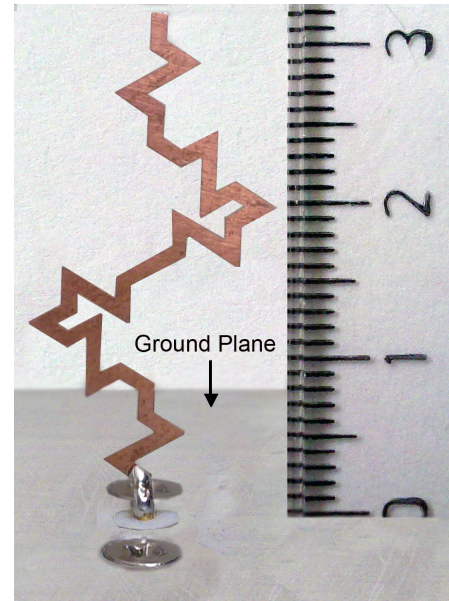
Fig. 3. Photograph of the fractal antenna prototype.

III. SIMULATION AND MEASUREMENT RESULTS

The MoM (method of moments) is a very powerful technique which can be applied to the analysis of complicated geometries such as fractal structures. MoM is used for simulation of this antenna based on the SuperNEC electromagnetic simulator software. One starts with defining the antenna structure for the software, then specifying the feed location. The wire conductivity of all conductors is assumed to be 5.7E7. Also, the ground plane is assumed perfect. The voltage source is 1 volt and the frequency range is from 5 GHz – 30 GHz.

Figure 4 shows the simulated and measured reflection coefficient versus frequency.

According to the input reflection coefficient, this UWB antenna is applied in 6 - 30 GHz frequency range and can be matched with a 50 Ω coaxial cable. So, the bandwidth of this structure is more than the variations of the Koch monopole antennas.

To study the radiation pattern, Figure 5 presents the radiation patterns for three frequencies, including 8 GHz, 15 GHz, and 20 GHz for the *x-y*, *x-z,* and *y-z* planes.
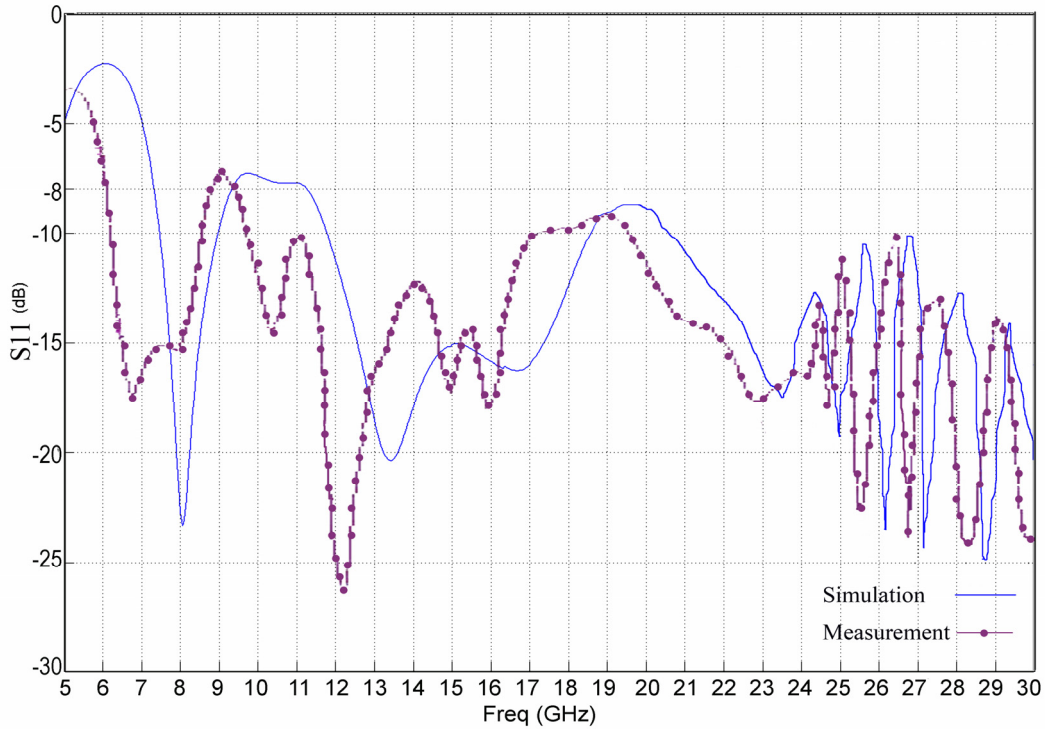
Fig. 4. The simulated and measured S_{11}.
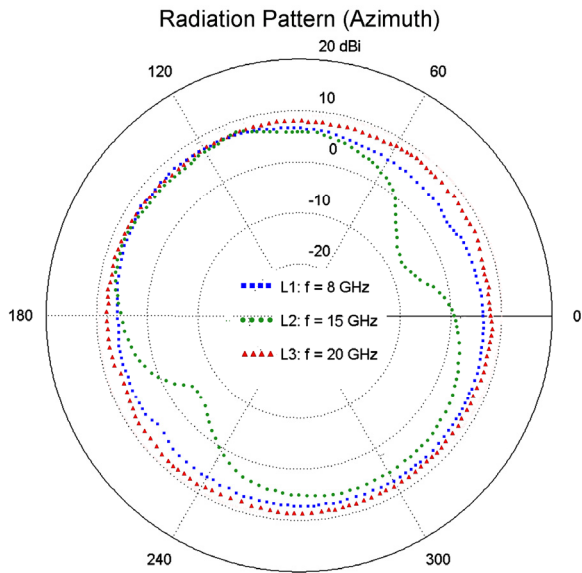
Fig. 5a. Radiation Patterns (*x-y* plane).
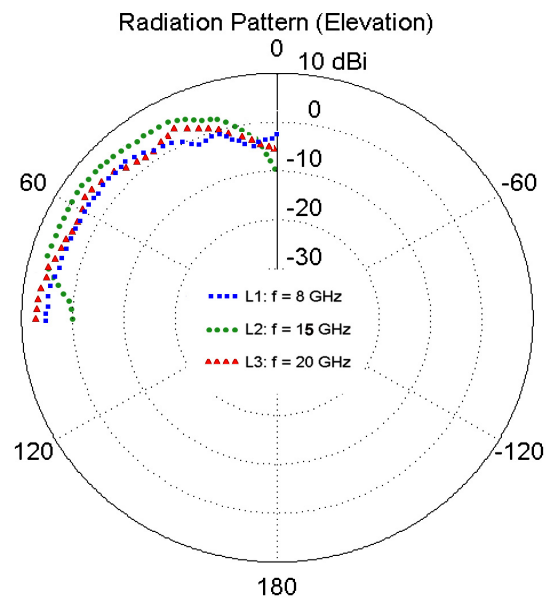
Fig. 5b. Radiation Patterns (*x-z* plane).

It can be observed that the antenna provides a nearly omnidirectional pattern over the desired frequency bandwidth.
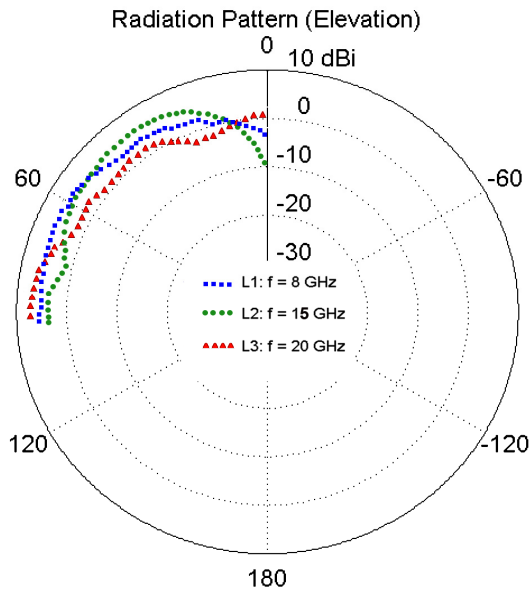
Fig. 5c. Radiation Patterns (*y-z* plane).

IV. CONCLUSION

Fractals have been used to achieve miniaturization and multi-band operation in antenna systems. Fractal geometries have miniaturized antenna elements. It has also been used in the design of multi-band antennas.

The unique fractal monopole antenna was simulated and fabricated, with similar results in the modeled and measured performance. The proposed antenna has a compact structure, a second iteration of a new fractal geometry, and measuring only 3.2×1.6 cm^2 when fabricated. Simulations show usable performance from 6 to 30 GHz. Measurements and fabrication show that the antenna works according to predictions, is simple to design, and is relatively easy to construct.

REFERENCES

[1]   A. Azari and J. Rowhani, "Ultra Wideband Fractal Microstrip Antenna Design," *Progress In Electromagnetics Research C*, vol. 2,7-12, 2008.

[2]   D. H. Werner and S. Ganguly, "An Overview of Fractal Antenna Engineering Research," *IEEE Antenna and Propagation Magazine*, vol. 45, pp. 38-57, Feb. 2003.

[3]   K. J. Vinoy, J. K. Abraham, and V. K. Varadan, "Generalized Design of Multi-

Resonant Dipole Antennas using Koch Curves," *Applied Computational Electromagnetic Society (ACES) Journal*, vol. 19, no. 1, pp. 22–31, March 2004.

[4]   K. J. Vinoy, J. K. Abraham, and V. K. Vardan, "On the Relationship Between Fractal Dimension and the Performance of Multi-Resonant Dipole Antennas using Koch Curves," *IEEE Transactions on Antennas and Propagations*, vol. 51, no. 9, 2296 – 2303, Sep. 2003.

[5]   A. Azari, "A New Fractal Antenna for Super Wideband Applications," *Progress in Electromagnetics Research Symposium*, Cambridge, MA, USA, pp. 885-888, Jul. 2010.

[6]   J. P. Gianvittorio and Y. R. Samii, "Fractal Antennas: A Novel Antenna Miniaturization Technique and Applications," *IEEE Antenna and Propagation Magazine*, vol. 44, no. 1, Feb. 2002.

[7]   J. Romeu and J. Soler, "Generalized Sierpinski Fractal Multiband Antenna," *IEEE Trans. Antennas Propagat.*, vol. 49, no. 8, pp. 1237–1239, Aug. 2001.

[8]   D. H. Werner, R. L. Haupt, and P. L. Werner, "Fractal Antenna Engineering: The Theory and Design of Fractal Antenna Arrays," *IEEE Ant. Propagation Mag.*, vol. 41, no. 5, pp. 37-59, 1999.

[9]   J. Gouyet, *Physics and Fractal Structures,* New York: Springer, 1996.

[10] D. H. Werner and R. Mittra, *Frontiers in Electromagnetics*, New York: IEEE Press 2000.

[11] C. A. Balanis, *Antenna Theory: Analysis and Design*, 3rd edition, Wiley, 2005.

[12] A. Azari, "A New Ultra Wideband Fractal Antenna" *Electromagnetic Theory Symposium*, Berlin, Germany, pp. 471-474 Aug. 2010.

[13] A. Azari, "Super Wideband Fractal Antenna Design," *IEEE MAPE*, Beijing, CHINA, pp. 249-252, Oct. 2009.

[14] A. Azari, "A New Fractal Monopole Antenna for Super Wideband Applications," *IEEE MICC*, Kuala lumpur, Malaysia, 2009.

[15] A. Azari and J. Rowhani, "Ultra Wideband Fractal Antenna Design," *IASTED ARP*, Baltimore, MD, USA, 2008.

Numerical Simulation of Substation Grounding Grids Buried in Vertical Earth Model Based on the Thin-Wire Approximation with Linear Basis Functions

Zhong-Xin Li, Guang-Fan Li, Jian-Bin Fan, and Yu Yin

Department of High Voltage
China Electrical Research Institute, Beijing, China
lizx@epri.sgcc.com.cn, ligf@epri.sgcc.com.cn, fanjb@epri.sgcc.com.cn, yiny@epri.sgcc.com.cn

Abstract ─ In order to improve the precision of the numerical result, the fast convergent Galerkin's type of boundary element method (BEM) with one order basis function is developed to calculate the grounding system buried in the vertical multilayer earth model. In this paper, the method is taken to simulate and analyze a grounding system including a floating electrode with any complicated structure, which can be located anywhere in the vertical multilayer earth model. The quasi-static complex image method (QSCIM) and the closed form of Green's function for the vertical multilayer earth model are introduced; the QSCIM is implemented by the matrix pencil (MP) approach.

Index Terms ─ Boundary element method, grounding system, quasi-static complex image method.

I. INTRODUCTION

There have been lots of papers researching the transient performance of AC substation grounding systems [1-8]; meanwhile, there also have been many papers studying the steady performance of AC substation grounding systems, especially in the low-frequency domain (about 50 to 60 Hz) [9-29]. This paper focuses on steady performance in low frequency of the AC substation grounding systems. References [9-17] are based on the unequal potential mathematical model, and references [18-29] are based on the equipotential mathematical model. In this paper, only the equipotential mathematical models for grounding problems buried in the vertical multilayer earth model will be discussed, and we can observe these equipotential mathematical model references [18-29] with some variations: electrostatic theory is used in [18-26], while quasi-static electric field theory is used in [27-29]. For grounding problems in the vertical earth model case at a low frequency domain, [17] discusses the grounding problem based on an unequal potential mathematical model; however, [27-29] discusses the grounding problem basing on equal potential mathematical model.

In the papers [27 and 28], the infinite Maclaurin series is used to expand the integral kernel of Green's function of a Hertz dipole to avoid infinite integrals about Bessel function. Meanwhile, the complex image method based on the same Maclaurin's series expansion has been studied for horizontal multilayer earth model in the early references [30 and 31]. To avoid an infinite series, a method named quasi-static complex image for horizontal and vertical multilayer earth model is used in references [13-17, and 29]. It points out that the integral kernel of Green's function can be expanded to the finite exponential term series, and hence, the complex image method requires only four to six images to obtain accurate results.

BEM for solving the grounding system problem has been pioneer researched in [25 and 26]. However, the applications of the BEM for grounding systems are also based on the direct current electrical field theory. The BEM has been developed to calculate the AC grounding system's problem based on the quasi-static electrical field theory in paper [29], recently. However, the zero order basis function is used in paper [29].

To improve the precision of numerical results, a hybrid with the closed form of Green's function of the vertical multilayer earth model, fast

convergent Galerkin's type of the BEM combined with one order basis function is developed in this paper, the QSCIM and the closed form of Green's function for vertical multilayer earth model are introduced, and the QSCIM is implemented by the MP approach. So it can be used to calculate the currents distribution along both the grounding system and the floating metallic conductors buried in the vertical multilayer earth model; meanwhile, not only the conductive effect of current leaking into the vertical multilayer earth model, but also capacitive effects from the vertical multilayer earth model, have been considered in the method.

II. THE BASIS OF THE SIMULATION METHOD

A. 2D BEM

In the numerical simulation of the grounding system including a floating electrode buried in N_s-layer earth model, the grounding system including the floating electrode is divided into small cylindrical segments. First, supposing the system consists of total N_l segments of cylindrical bars. Then, considering the leakage currents density J_i ($i = 1,\ldots,N_l$) emanating from the surface of each segment as unknowns. Next, constructing an equation system, and supposing the grounding system and floating electrode are equipotential, and the scalar electrical potential (SEP) of each segment are also unknown. In this way, by solving the equation system, the currents can be obtained. Finally, the SEP at any point can be calculated by the contributions of all the currents.

From [25, 29, and 35], applying BEM, we have weighted the residual method as

$$\int_{S_j} \sum_{m=1}^{M} W_m^{(s)}(\overline{r})\varphi_j(\overline{r})dS_j$$

$$= \sum_{i=1}^{N_l} \int_{S_j} \sum_{m=1}^{M} W_m^{(s)}(\overline{r}) \int_{S'_i} G_\phi(\overline{r},\overline{r}\,') \sum_{n=1}^{M} J_n N_n^{(s)}(\overline{r}\,')dS'_i\, dS_j.$$
(1)

Here, $j = 1,\ldots,N_l$, S_i and S_j are the surfaces of ith and jth segments, dS'_i and dS_j are the infinite small surface elements of the cylindrical segments. Both basis functions and weight function $\{N_n^{(s)}(\overline{r}\,'), W_m^{(s)}(\overline{r}\,'), m,n = 1,\ldots,M\}$ defined on S.

It should be pointed out that 2D discretizations required to solve the above equations in real cases (grounding grids) imply an extremely large number

of degrees of freedom. Taking into account that the coefficients matrix in Eq. (1) is not sparse, and that 2D integration in Eq. (1) must be performed twice over the electrode surface, some reasonable simplifications must be introduced to reduce computational cost under an acceptable level.

B. Approximated 1D BEM

It is reasonable to suppose that the leakage current density is constant around the cross section of the cylindrical electrode [32-35], and seems not restrictive whatsoever if we take into account the real geometry of the grounding grids.

Let l be the whole set of axial lines of the buried conductors; let $\hat{r} \in l$ be the orthogonal projection of a generic point $\overline{r} \in S$; let $D(\hat{r})$ be the conductor diameter and suppose all diameters of the conductor segments are the same; and let $J(\hat{r})$ be the approximated leakage current density at this point (assumed uniform around the cross section) in each segment, we can have

$$\phi_j(\overline{r}) = \sum_{i=1}^{N_l} \int_{l_j} \tilde{G}_\phi(\overline{r},\hat{r}\,')J_i(\hat{r}\,')D(\hat{r}\,')dt_i,$$
(2)

where $j = 1,\ldots,N_s$ and the Green's function of a point current source within the half infinite homogenous earth model is

$$\tilde{G}_\phi(\overline{r},\hat{r}\,') = \frac{1}{4\overline{\sigma}_1}\left(\frac{1}{\tilde{R}} - \frac{k_{01}}{\tilde{R}'}\right).$$
(3)

$\tilde{G}_\varphi(\overline{r},\hat{r}\,')$ is the average of kernel $G_\varphi(\overline{r},\overline{r}\,')$ around the cross-section at $\hat{r}'$ [25], $\overline{\sigma}_1 = \sigma_1 + j\omega\varepsilon_1$ is the complex conductivity of the homogenous earth.

As the leakage current is not really uniform around the cross-section, variational equality Eq. (1) does not hold anymore if we use Eq. (2). Therefore, it is necessary to restrict the class of weighting functions to those with circumferential uniformity, obtaining

$$\int_{l_j} W(\hat{r})\varphi_j(\hat{r})D(\hat{r})dt_j$$

$$= \sum_{i=1}^{N_l} \int_{l_j} W(\hat{r}) \int_{l'_i} \hat{G}_\phi(\hat{r},\hat{r}\,')J(\hat{r}\,')D(\hat{r})dt'_i\, D(\hat{r})dt_j,$$
(4)

where $j = 1,\ldots,N_l$, dt_i and dt_j lie on l_i and l_j, respectively. For all members $W(\hat{r})$ of a suitable class of weighting functions on l, $\hat{G}_\varphi(\hat{r},\hat{r}\,')$ is the average of kernel $G_\varphi(\overline{r},\overline{r}\,')$

around cross sections at $\hat{r}$ and $\hat{r}'$ [25]. The Green's function of a point current source within the half infinite homogenous earth model is

$$\hat{G}_\phi(\hat{r},\hat{r}') = \frac{1}{4\overline{\sigma}_1}(\frac{1}{\hat{R}} - \frac{k_{01}}{\hat{R}'}). \qquad (5)$$

For a given set of 1D boundary elements $\{l^i; i = 1,\cdots,N_l\}$ and basis functions $\{N_{l_i}(\hat{r}), i = 1,\cdots,M\}$ defined on l, the whole set of axial lines of the buried conductors l and the unknown leakage current density $J_l(\hat{r})$ of each segment can be discretized as

$$J_l(\hat{r}) = \sum_{i=1}^{M} J_{l_i}(\hat{r}), \qquad (6)$$

$$l = \bigcup_{i=1}^{N_l} l_i. \qquad (7)$$

Finally, for a given set $\{W_{l_j}(\hat{r}); \; j = 1,\cdots,M\}$ of weighting functions defined on l, variational statement of Eq. (4) is reduced to a linear equations system:

$$\int_{l_j} \sum_{m=1}^{M} W_{l_m}(\hat{r})\varphi_j(\hat{r})dt_j$$

$$= \sum_{i=1}^{N_l} \int_{l_j} \sum_{m=1}^{M} W_{l_m}(\overline{r})\int_{l'_i} \hat{G}_\phi(\hat{r},\hat{r}')\sum_{n=1}^{M} J_{l_n} N_{l_n}(\overline{r}')dt'_i \, dt_j, \qquad (8)$$

where $j = 1,\ldots,N_l$.

To apply a Galerkin-type of the BEM, we use Galerkin's weighting approach (weighting functions are identical to basis functions), $W_{l_i}(\hat{r}) = N_{l_i}(\hat{r})$, not like [29], which supposes that the current density $J_{l_i}(\hat{r})$ ($i = 1,\ldots,N_l$) uniformly emanates from the surface of each segment, in order to improve that of the numerical result's precision, here one order basis function is used, and set $M = 2$,

$$\sum_{i=1}^{2} J_{l_i} N_{l_i}(\hat{r}) = \begin{bmatrix} \dfrac{t_i}{l_i} & \dfrac{1}{l_i} \end{bmatrix}\begin{bmatrix} J^1_{l_i} \\ J^0_{l_i} \end{bmatrix} = \dfrac{J^1_{l_i}}{l_i}t_i + \dfrac{J^0_{l_i}}{l_i}. \qquad (9)$$

Thus, we have

$$\int_{l_j} \begin{bmatrix} \dfrac{t_j}{l_j} \\ \dfrac{1}{l_j} \end{bmatrix}\phi_j dt =$$

$$\sum_{i=1}^{N_l} \int_{l_j} \begin{bmatrix} \dfrac{t_j}{l_j} \\ \dfrac{1}{l_j} \end{bmatrix}\int_{l_i} \hat{G}_\phi(\hat{r},\hat{r}')\begin{bmatrix} \dfrac{t_i}{l_i} & \dfrac{t_i}{l_i} \end{bmatrix}\begin{bmatrix} J^1_{l_i} \\ J^0_{l_i} \end{bmatrix}dt_i dt_j. \qquad (10)$$

Furthermore,

$$\begin{bmatrix} \dfrac{l_j^2}{2} \\ 1 \end{bmatrix}\phi_j = \sum_{i=1}^{N_l} \frac{1}{l_j}\int_{l_j} \frac{1}{l_i}\int_{l_i} \hat{G}_\phi(\hat{r},\hat{r}')\begin{bmatrix} t_j t_i & t_j \\ t_i & 1 \end{bmatrix}\begin{bmatrix} J^1_{l_i} \\ J^0_{l_i} \end{bmatrix}dt_i dt_j, \qquad (11)$$

where $j = 1,\ldots,N_l$. The coefficient matrix in the linear system Eq. (11) is symmetric and positive definite [36].

The SEP at any point can be calculated by all leakage currents.

$$\phi_j(\overline{r}) = \sum_{i=1}^{N_l} \int_{l_i} \tilde{G}\phi(\overline{r},\hat{r}')(\frac{J^1_{l_i}}{l_i}t_i + \frac{J^0_{l_i}}{l_i})dt_i, \qquad (12)$$

where $j = 1,\ldots,N_s$.

Extensive computing is still required to evaluate the averaged kernels $\tilde{G}_\varphi(\overline{r},\hat{r}')$ and $\hat{G}_\varphi(\hat{r},\hat{r}')$ by means of circumferential integration around cross sections at point $\hat{r}$ for $\tilde{G}_\varphi(\overline{r},\hat{r}')$ and at points $\hat{r}$ and $\hat{r}'$ for $\hat{G}_\varphi(\hat{r},\hat{r}')$. The circumferential integration can be avoided by means of the following approximations [25]

$$\hat{R} = \sqrt{(\hat{r}-\hat{r}')^2 + \frac{D(\hat{r}')^2}{4}} = \sqrt{(\hat{r}-\hat{r}')^2 + \frac{D^2}{4}}, \qquad (13)$$

$$\tilde{R} = \sqrt{(\hat{r}-\hat{r}')^2 + \frac{D(\hat{r})^2 + D(\hat{r}')^2}{4}} = \sqrt{(\hat{r}-\hat{r}')^2 + \frac{D^2}{2}}. \qquad (14)$$

Let the total leakage current from grounding system be I_0, and the total current into and out of the floating electrode be zero.

For simple expression, we just consider there is only a grounding system and no floating electrode there, the equation system can be expanded as:

$$\begin{bmatrix} Z_{1,1}^{11} & \cdots & Z_{1,N_l}^{11} & Z_{1,1}^{10} & \cdots & Z_{1,N_l}^{10} & -\dfrac{l_1}{2} \\ \vdots & \vdots & \vdots & \vdots & \vdots & \vdots & \vdots \\ Z_{N_l,1}^{11} & \cdots & Z_{N_l,N_l}^{11} & Z_{N_l,1}^{10} & \cdots & Z_{N_l,N_l}^{10} & -\dfrac{l_{N_l}}{2} \\ Z_{1,1}^{01} & \cdots & Z_{1,N_l}^{01} & Z_{N_l,1}^{00} & \cdots & Z_{1,N_l}^{00} & -1 \\ \vdots & \vdots & \vdots & \vdots & \vdots & \vdots & \vdots \\ Z_{N_l,1}^{01} & \cdots & Z_{N_l,N_l}^{01} & Z_{N_l,1}^{00} & \cdots & Z_{N_l,N_l}^{00} & -1 \\ \dfrac{l_1}{2} & \cdots & \dfrac{l_{N_l}}{2} & 1 & \cdots & 1 & 0 \end{bmatrix} \begin{bmatrix} J_{l_1}^1 \\ \vdots \\ J_{l_{N_l}}^1 \\ J_{l_1}^0 \\ \vdots \\ J_{l_{N_l}}^0 \\ \phi_1 \end{bmatrix} = \begin{bmatrix} 0 \\ \vdots \\ 0 \\ 0 \\ \vdots \\ 0 \\ I_0 \end{bmatrix},$$

(15)

where $Z_{ij,(i,j=1,\cdots,N_l)}^{nm,(n,m=0,1_l)}$ is the mutual impedance coefficient between a pair of segments with J^n or J^m in grounding system, $J_{l_i,(i=1,\cdots,N_l)}^{n,(n=0,1_l)}$ are currents with J^n emanating from the grounding system, φ_1 is the SEP of the grounding system. If floating electrodes existed, we can deal with it in the same way.

Supposing the total grounding currents I_0 emanating from the grounding system are known, the leakage current of each segment and the SEP of the grounding system and floating electrode can be obtained by solving Eq. (15). The SEP at any point can then be calculated by the known currents. The grounding impedance and admittance are given by the relation

$$Z_g = \frac{1}{Y_g} = \frac{\phi_1}{I_0} = R_g + jX_g. \tag{16}$$

The element $Z_{ij,(i,j=1,\cdots,N_l)}^{nm,(n,m=0,1_l)}$ is defined as

$$Z_{ij}^{nm} = \frac{1}{l_i l_j} \int_{l_i} \int_{l_j} \hat{G}_\phi(\hat{r},\hat{r}') t_i^m dt_i t_j^n dt_j. \tag{17}$$

For a semi-infinite, homogenous earth model, we have

$$Z_{ij}^{nm} = \frac{1}{l_i l_j} \int_{l_i} \int_{l_j} (\frac{1}{\hat{R}} - \frac{k_{01}}{\hat{R}'}) t_i^m dt_i t_j^n dt_j. \tag{18}$$

III. THE GREEN'S FUNCTIONS

The main task of simulating grounding systems is to calculate the mutual impedance coefficients shown in Eq. (17). If the earth is a half infinite homogenous conductive medium, Eq. (18) will be calculated easily. However, as the earth is sometimes regarded as a horizontal or vertical multilayer conductive medium in practice, an infinite integral about Bessel function in the Green's function must be calculated, and some fast calculation techniques must be adopted to avoid the integral. As the result, the corresponding closed form of Green's function of a point source in the vertical multilayer earth model must be defined. In order to explain the Green's function of a vertical multilayer earth model, we will explain the Green's function of a horizontal multilayer earth model first.

A. Horizontal multilayer earth model

Considering the low frequency (50 or 60 Hz and higher harmonic wave) and limited size of the substation, the electromagnetic wave's propagating effect can be neglected, so the electromagnetic field can be regarded as a quasi-static electrical field, in this way, the SEP φ of a point source with unit current δ buried in a horizontal multilayer earth model satisfies the Poisson equation, supposing the point source is located at the origin of the coordinate system (Fig. 1), the Poisson equation can be expressed as:

$$\nabla^2 \phi_{ij}(x,y,z) = -\frac{\delta(x)\delta(y)\delta(z)\varsigma(ij)}{\bar{\sigma}_i}, \tag{19}$$

$$\phi_{ij}(x,y,z) = \phi_{i(j+1)}(x,y,z), \tag{20}$$

$$\bar{\sigma}_j \frac{d\phi_{ij}(x,y,z)}{dz} = \bar{\sigma}_{j+1} \frac{d\phi_{i(j+1)}(x,y,z)}{dz}, \tag{21}$$

where $\bar{\sigma}_1$ is the complex conductivity of ith layer soil, and δ is the Dirac delta function. The subscript i represents the medium in which the unit current is located, and j is the medium in which the SEP is calculated. $\varsigma(ij)$ is Kronecker's symbol.
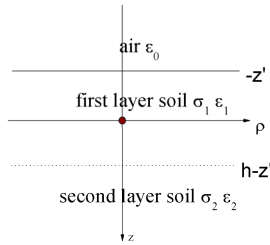
Fig. 1. A scalar point source buried in a horizontal 2-layer earth model.

The procedure for the closed form of the Green's function of a point source in an arbitrary horizontal multilayer earth model can be referred in [29].

Here, two layer earth models are used as an example, according to the procedure in [29], the expression of G_{11} can be given as follows:

$$G_{11}(x,y,z) = \frac{1}{4\pi\bar{\sigma}_1}\int_0^\infty [e^{-k_\rho|z|} - k_{01}e^{-k_\rho(2z'+z)}$$

$$+ f(k_\rho)(k_{01}^2 k_{12}e^{-k_\rho(2h+2z'+z)} - k_{01}k_{12}e^{-k_\rho(2h+z)}$$

$$+ k_{12}e^{-k_\rho(2h-2z'-z)} - k_{01}k_{12}e^{-k_\rho(2h-z)})]J_0(k_\rho\rho)dk_\rho,$$

$$(22)$$

where $f(k_\rho) = \dfrac{1}{1+k_{01}k_{12}e^{-k_\rho 2h}}$, $k_{01} = \dfrac{\bar{\sigma}_0 - \bar{\sigma}_1}{\bar{\sigma}_0 + \bar{\sigma}_1}$,

$k_{12} = \dfrac{\bar{\sigma}_1 - \bar{\sigma}_2}{\bar{\sigma}_1 + \bar{\sigma}_2}$, h is the thickness of the top earth layer. $\bar{\sigma}_0$, $\bar{\sigma}_1$, and $\bar{\sigma}_2$ are the complex conductivity of air and two-layer earth, respectively.

In order to avoid Maclaurin's infinite series, we can develop the $f(k_\rho)$ as an exponential series with finite terms by the MP approach as follows [38]:

$$f(k_\rho) = \sum_{i=1}^M \alpha_i e^{\beta_i k_\rho}, \qquad (23)$$

where α_i and β_i are constants to be determined by choosing sample points of function $f(k_\rho)$. The MP approach can give highly accurate results with only a few terms, usually four terms, once $f(k_\rho)$ is a monotonic function. How to achieve the exponential series with finite terms by MP can further refer to the appendix part. By employing

the development expression of $f(k_\rho)$ Eq. (23) and the Lipschitz integration, we can obtain

$$G_{11}(x,y,z) = \frac{1}{4\pi\bar{\sigma}_1}[\frac{1}{R_0} - \frac{k_{01}}{R'_0}$$

$$+ \sum_{i=1}^M \alpha_i(\frac{k_{01}^2 k_{12}}{R_{i1}} - \frac{k_{01}k_{12}}{R_{i2}} + \frac{k_{12}}{R_{i3}} - \frac{k_{01}k_{12}}{R_{i4}})], \quad (24)$$

where the origin of the coordinate system shown in Fig. 1 has been moved to the surface between air and earth, and the source point at $(0,z')$, and the field point at (ρ,z'), so $R_0 = \sqrt{\rho^2 + (z-z')^2}$,

$R'_0 = \sqrt{\rho^2 + (z+z')^2}$,

$R_{i(1\sim4)} = \sqrt{\rho^2 + (sign_a \cdot z + sign_b \cdot z' + z_i)^2}$. in which $sign_a = 1$ and $sign_b = -1$ for R_{i1} and R_{i3} , $sign_a = -1$ and $sign_b = 1$ for R_{i3} and R_{i4} , $sign_a = sign_b = 1$ for others, $z_i = 2h - \beta_i$.

Each term except $\dfrac{1}{R_0}$ of Eq. (24) can be regarded as an image point source, whose location is indicated by R_i and amplitude by α_i. However, R_i and α_i in Eq. (24) are complex numbers, and the electromagnetic field here was regarded as a quasi-static electrical field so that this approach is named the QSCIM.

Similarly, we can get G_{11} and G_{12}.

B. Vertical multilayer earth model

Just like a point source buried in a horizontal multilayer earth model, here the SEP φ of a point source with unit current δ buried in a vertical multilayer earth model also satisfies the Poisson equation, as we can see in Fig. 2, here we choose the vertical three layers earth model as an example.
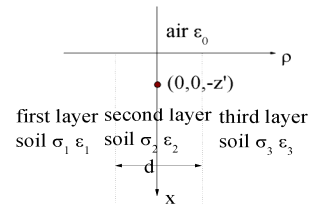

Fig. 2. A scalar point source buried in a vertical, 3-layer earth model.

First, an image point source $\delta' = -k_{12}\delta$ $(0,0,-z')$ can be found in air opposite to the point source $\delta(0,0,z')$, which can be seen in Fig. 3(a), in this way, vertical three-layer medium is full of the air. Second, the coordinate axes ρ is inverted from the right direction to the left direction. Then, the coordinate axes ρ is anticlockwise circumvolved downwards with 90 degrees. Last, we can reset the coordinate axes x instead of old ρ and new ρ instead of z, which can be seen in Fig. 3(b).
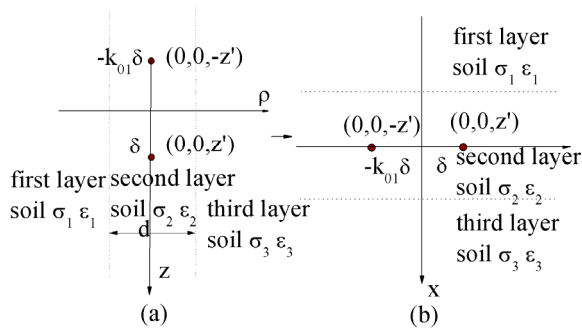

Fig. 3. How to transform the vertical, 3-layer earth model into a horizontal model.

From Fig. 3(b), we can see that each point source δ or δ' can be considered to be buried in a horizontal three layer conductive medium, just like the point source in Fig. 1; so Green's function of point source δ or δ' can be gotten just like the one buried in the horizontal three layer conductive media model. Apply the theory of superposition; the Green's function of a point source buried in the vertical three layer earth model can be gotten.

$$G_{22}(r,r') = \frac{1}{4\pi\overline{\sigma}_1}\{\frac{1}{R_{00}} - \frac{k_{12}}{R_{00}} - \frac{k_{01}}{R'_{00}} + \frac{k_{01}k_{12}}{R'_{01}}$$

$$+ \sum_{i=1}^{M}\alpha_n[(\frac{k_{23}}{R_{i1}} - \frac{k_{12}k_{23}}{R_{i2}} - \frac{k_{12}k_{23}}{R_{i3}} - \frac{k_{12}}{R_{i4}})$$

$$-k_{01}(\frac{k_{23}}{R'_{i1}} - \frac{k_{12}k_{23}}{R'_{i2}} - \frac{k_{12}k_{23}}{R'_{i3}} - \frac{k_{12}}{R'_{i4}})]\}, (22)$$

where R_{00} and R'_{00} are same as t R_0 and R'_0 of Eq. (24),

$$R_{01} = \sqrt{(x+x')^2 + (y-y')^2 + (z-z')^2},$$

$$R'_{01} = \sqrt{(x+x')^2 + (y-y')^2 + (z+z')^2},$$

$$R_{i(1\sim4)} = \sqrt{(sign_a \cdot x + sign_b \cdot x' + x_i)^2 + (y-y')^2 + (z-z')^2},$$

and

$$R_{i(1\sim4)} = \sqrt{(sign_a \cdot x + sign_b \cdot x' + x_i)^2 + (y-y')^2 + (z+z')^2}.$$

The signs are $sign_a = 1$ and $sign_b = -1$ for R_{i1} and R_{i3}, $sign_a = -1$ and $sign_b = 1$ for R_{i3} and R_{i4}, and $sign_a = sign_b = 1$ for others, $x_i = 2h - \beta_i$. Note that here $f(k_\rho) = \frac{1}{1 + k_{12}k_{23}e^{-k_\rho 2h}}$ has been expanded into the finite exponential terms series, which is different from the one of the horizontal multilayer earth model. Meanwhile, when the two layers vertical earth model is considered, the complex images of the point source will disappear. This is also different from the one of the horizontal multilayer earth model.

Similarly, we can get G_{21}, G_{23}, G_{11}, G_{12}, G_{13}, G_{31}, G_{32} and G_{33}. The Green's function of a point source buried in the arbitrary vertical multilayer earth model can be achieved in a similar way.

Once the closed form of Green's function of a point source in the vertical multilayer earth model has been derived, the mutual impedance coefficient can be fastly calculated through Eq. (17). It should be pointed out that the integral of Eq. (17) can be analytically calculated with the closed form of Green's function, for 0 order (n=0, m=0) term, which is described in [24], and one order (n=0, m=1; n=1, m=0; n=1, m=1) terms can refer to [25].

IV. SIMULATION RESULTS AND ANALYSIS

According to the approach introduced in this paper, a FORTRAN language program has been implemented; the program can simulate a grounding system and up to the vertical three-layer earth model.

A. Verification of the approach

To verify the result of the method proposed in this work, some cases solved by other authors are studied.

The first case, from [28], is a horizontal grounding electrode of 20m length and 0.16m radius, buried at $l_0 = 1m$ depth in the vertical,

three-layer earth, where $p_{21} = \dfrac{\overline{\sigma}_2}{\overline{\sigma}_1}$, $p_{32} = \dfrac{\overline{\sigma}_3}{\overline{\sigma}_2}$, $\sigma_1 = 0.01 S/m$, $\varepsilon_1 = 81\varepsilon_0$, $\varepsilon_2 = 5\varepsilon_0$, $\varepsilon_3 = 2\varepsilon_0$, $d = 3m$, $f = 50Hz$, and $I_e = 300A$, which can be seen in Fig. 4.
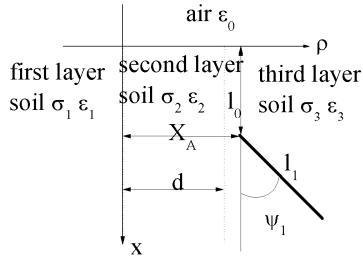

Fig. 4. Configuration of a simulated grounding conductor.

There are two results in [19]: (1) $X_A = d+1 = h+1 = 4m$, $\theta_1 = 90^o$, and $\psi_1 = 0^o$, the result can be seen in Table I; and (2) $X_A = d+1 = h+1$, $\theta_1 = \psi_1 = 90^o$, the result can be seen in Tables 2 and 3.

The second case also comes from [28], which can also be seen in Fig. 4. The vertical three-layer earth model is considered, whose left layer soil's conductivity and permittivity are $\sigma_1 = \sigma_0 = 0.0 S/m$ and $\varepsilon_1 = \varepsilon_0$, the middle layer soil's conductivity and permittivity are $\sigma_2 = 1000.0^{-1} S/m$ and $\varepsilon_2 = 5\varepsilon_0$, its thickness is $d = 1.5m$, the right layer soil's conductivity and permittivity are $\sigma_2 = 250.1^{-1} S/m$ and $\varepsilon_3 = 9\varepsilon_0$, a horizontal grounding electrode of $l_1 = 20m$ length and 9.23mm radius and buried at $l_0 = 1m$ depth in the vertical three-layer earth is chosen. Other parameters are $X_A = 4.5m$, $Y_A = 0.0m$, $f = 50Hz$, and $\theta_1 = 90^o$. Good agreements can be seen in Table 4.

B. The computational cost and accuracy of the approach

First, by considering some reasonable simplification, the approach calculates the grounding system based on the 1D Galerkin type

of BEM. Second, the main task of simulating grounding system is to calculate the mutual

Table 1: Comparison of our results $Z_g(\Omega)$ with a published model: $p_{21} = 0.01$ and $p_{32} = 10.0$

Ref. [9]	Zero-order function	One-order function
5.30–j7.17e–6	5.37–j7.74e–6	5.37–j7.72e–5

Table 2: Comparison of our results $Z_g(\Omega)$ with a published model: $p_{21} = 0.01$ and $p_{32} = 10.0$

h	Ref. [9]	Zero-order function	One-order function
0	2.77-j5.34e-6	2.75-j2.42e-6	2.75-j2.41e-6
1e-3	2.78-j2.56e-6	2.34-j4.14e-6	2.34-j4.14e-6
1e-1	3.45-j9.75e-6	3.24-j12.89e-6	3.24-j12.88e-6
1e-0	5.44-j17.83e-6	5.67-j21.18e-6	5.67-j21.19e-6
1e1	7.23-j13.54e-6	7.58-j15.11e-6	7.58-j15.12e-6
1e3	7.72-j11.88e-6	7.99-j11.99e-6	7.99-j11.98e-6
1e5	7.70-j11.01e-6	8.00-j11.95e-6	8.00-j11.97e-6

Table 3: Comparison of our results $Z_g(\Omega)$ with a published model: $p_{21} = 100.0$ and $p_{32} = 0.1$

h	Ref. [9]	Zero-order function	One-order function
0	7.70-j115.34e-6	7.80-j135.55e-6	7.80-j135.54e-6
1e-3	7.69-j130.01e-6	8.20-j152.16e-6	8.20-j152.15e-6
1e-1	7.04-j104.27e-6	7.30-j118.11e-6	7.30-j118.12e-6
1e-0	5.06-j46.46e-6	4.87-j49.01e-6	4.87-j49.02e-6
1e1	3.25-j11.27e-6	2.96-j10.11e-6	2.96-j10.10e-6
1e3	2.81-j4.65e-6	2.55-j2.94e-6	2.55-j2.93e-6
1e5	2.77-j4.28e-6	2.54-j2.87e-6	2.54-j2.86e-6

Table 4: Comparison of our results $Z_g(\Omega)$ with a published model [19]

ψ_1	Ref. [9]	Zero-order function	One-order function
0	15.51-j9.84e-5	15.12-j9.14e-5	15.04-j9.10e-5
90	15.58-j9.90e-5	15.16-j9.14e-5	15.08-j9.09e-5
60	15.85-j12.82e-5	15.32-j9.16e-5	15.24-j9.16e-5
90	16.82-j12.29e-5	15.96-j9.34e-5	15.96-j9.34e-5

impedance coefficients as shown in Eq. (17). Although the multilayer earth model must be considered in a real practice problem, the closed form of Green's function of a point source in the multilayer earth model can be taken to avoid verbose calculation about infinite integral or Maclaurin's series [25-35] by applying the QSCIM. Third, the analytical formula about mutual impedance is adopted to avoid numerical integral in the approach. Therefore, the approach is very fast. For a general real practiced grounding system, it needs only several seconds on a P4 computer. Verification of the approach has been shown in the above section, by comparing our results with those from a different method in other references, especially with measurement data. We can see that the accuracy of our approach is good.

C. Numerical result analysis

A complex grounding system can be seen in Fig. 5. The earth is modeled as a three vertical layers conductive media, whose conductivities and permittivity are $\sigma_1 = 100.0^{-1}\,S/m$, $\sigma_2 = 800.0^{-1}\,S/m$, $\sigma_3 = 300.0^{-1}\,S/m$, $\varepsilon_1 = 5\varepsilon_0$, $\varepsilon_2 = 12\varepsilon_0$, and $\varepsilon_3 = 10\varepsilon_0$. The middle layer's thickness is $d = 5m$. All the conductors' radius of grid is 10mm, and rods' radius of 16mm. The external excited AC current 1000A of current with power frequency (50Hz) is injected from the corner of the grounding system.

The calculated numerical results can be seen in Table 5. Note: Z_g is the grounding impedance; GPR_g is the grounding potential rise (GPR) of the grounding grid; SEP_f is the SEP of the floating grid; I_0 is the total leakage current of the

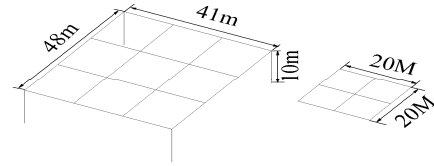grounding system; and if is the total net current flowing into and out of the floating grid.

Fig. 5. Grounding system and floating grid.

Table 5: Numerical results

	f=50Hz case	f=800Hz case
$Z_g(\Omega)$	1.78-j0.62e-5	1.78-j0.99e-4
$GPR_g(V)$	1775.74-j6.e-3	1775.74-j003
$SEP_f(V)$	437.19-j2.e-3	437.18-j0.03
$I_0(A)$	100.0-j1.24e-10	100.0+j3.26e-9
$I_f(A)$	-1.9e-6+j2.9e-11	1.7e-6-j5.8e-10

It can be seen that the total leakage current of the grounding system is close to the external injected current and net current flowing into and out of the small grid is near zero. All these verify the accuracy of this model.

The 3D distribution of SEP's absolute value along the earth surface is given in Fig. 6, and the 3D distribution of step voltage's absolute value along the earth surface is given in Fig. 7.
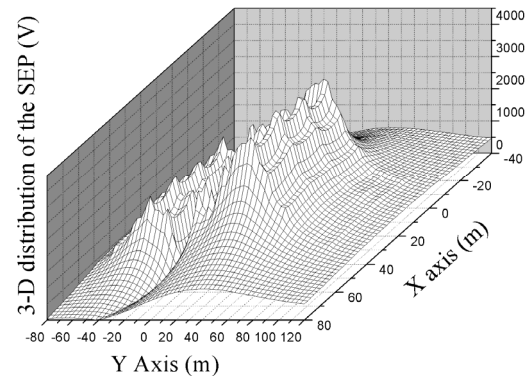

Fig. 6. The 3D distribution of the SEP absolute value for a vertical, three-layer earth model, obtained by the QSCIM.

It can be seen from Fig. 6, that (1) the SEP rise of the surface above the grounding grid is much higher, meanwhile, the distribution has been divided into three parts. This is because an external excited AC current was injected from the

grounding grid; the vertical three layer earth model has re-distribution of the leakage current along the grid. (2) the GPR is centralized above the grounding grid, the ground surface's SEP becomes lower around the grounding grid, meanwhile, the GPR along the interface between the different vertical layer earth has become small, so the step voltage will become bigger, the large value of step voltage is distributed around the earth surface above the edge of the grounding grid and the interface, which can be seen from Fig. 7. So some safety measures must be taken to mitigate the question.
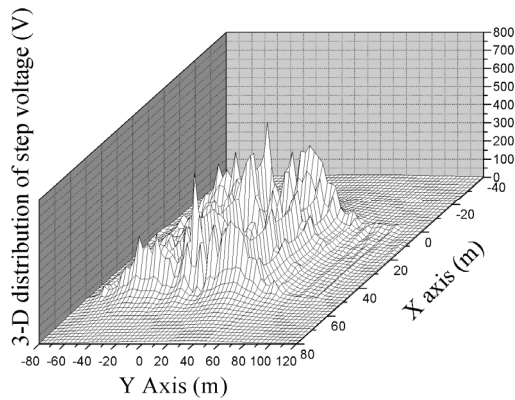

Fig. 7. The 3D distribution of the step voltage absolute value for a vertical, three-layer earth model, obtained by the QSCIM.

V. CONCLUSION

1. The quasi-static complex image approach is very efficient to simulate the grounding grids in vertical multilayer earth models. Usually, few quasi-static complex images can provide accurate simulation results.
2. Novel closed form of Green's functions for vertical multilayered earth model achieved by the method of quasi-static complex images have been introduced in this paper.
3. Linear basis function has succeeded in being realized in the BEM for simulating grounding systems.
4. A program based on Galerkin's BEM has been developed for simulating grounding systems with any complicated structure buried in up to the vertical three-layer earth models.

APPENDIX: THE QSCIM BASED ON MP METHOD

The QSCIM can be implemented with a MP approach. The MP approach is approximating a function by a sum of complex exponentials, and works well once the function monotonically decays.

From [38] and [39], if a function $f(x)$ can be expanded into finite exponential series, as below

$$f(x) = \sum_{i=1}^{M} \alpha_i e^{\beta_i x}. \qquad (26)$$

There are three parameters to be decided, such as M, α_i, and β_i.

In order to get these parameters, we first decide maximum sample points according to the characteristic of function $f(x)$, that means maximum value for x_{max} can be obtained. Once x_{max} has been known, we can get uniformly discrete values of $f(x)$ within scope $(0 \le x \le x_{max})$. So, we have uniform discrete function values of $f(x)$ with $(f(0), f(1), f(2), \cdots, f(N-1))$ corresponding to value of x as $(0, \Delta x, 2\Delta x, \cdots, (N-1)x)$ or $(0, x_1, x_2, \cdots, x_{max})$. Here, Δx is the rate of sampling. We can obtain

$$f(x) \approx \sum_{i=1}^{M} \alpha_i z_i^k \quad (k = 0, \cdots, N-1), \quad (27)$$

where

$$z_i^k = e^{\beta_i \Delta x} \qquad (i = 0, \cdots, M). \quad (28)$$

A. How to decide the number M

Since, we have the total N number of uniform discrete function values of $f(x)$, we can get the matrix $[Y]$ from the sampling data $f(x)$ by combining $[Y_1]$ and $[Y_2]$ as

$$[Y] = \begin{bmatrix} f(0) & f(1) & \cdots & f(L-1) \\ f(1) & f(2) & \cdots & f(L+1) \\ \vdots & \vdots & \cdots & \vdots \\ f(N-L-1) & f(N-L) & \cdots & f(N-1) \end{bmatrix}_{(N-L) \times (L+1)},$$

$$(29)$$

$$[Y_1] = \begin{bmatrix} f(0) & f(1) & \cdots & f(L-1) \\ f(1) & f(2) & \cdots & f(L) \\ \vdots & \vdots & \cdots & \vdots \\ f(N-L-1) & f(N-L) & \cdots & f(N-2) \end{bmatrix}_{(N-L) \times L} ,$$

(30)

$$[Y_2] = \begin{bmatrix} f(1) & f(2) & \cdots & f(L) \\ f(2) & f(3) & \cdots & f(L+1) \\ \vdots & \vdots & \cdots & \vdots \\ f(N-L) & f(N-L+1) & \cdots & f(N-1) \end{bmatrix}_{(N-L) \times L} ,$$

(31)

where L is referred to as the pencil parameter [38] and [39].

Note that $[Y_1]$ is obtained from $[Y]$ by omitting the last column, and $[Y_2]$ is obtained from $[Y]$ by omitting the first column. The parameter L can be chosen between $N/3$ and $N/2$.

Next, singular-value decomposition (SVD) of the matrix $[Y]$ can be implemented out as

$$[Y] = [U][\sum][V]^H ,$$

(32)

where $[U]$ and $[V]$ are unitary matrices, comprised of the eigenvector of $[Y][Y]^H$ and $[Y]^H[Y]$, respectively, and $[\sum]$ is a diagonal matrix including the singular values of $[Y]$, i. e.

$$[U]^H[Y][V] = [\sum].$$

(33)

The choice of the parameter M can be achieved at this stage by studying the ratios of various singular values to the largest one. Typically, the singular values beyond M are set equal to zero. The way M is chosen is as follows. Observe the singular value σ_c such that

$$\frac{\sigma_c}{\sigma_{\max}} \approx 10^{-p} ,$$

(34)

where p is the number of significant decimal digits in the data. For example, if the sampling data is accurate up to three significant digits, the singular values for which the ratio in Eq. (34) is below 10^{-3} are essentially useless singular values, and they should not be used in the reconstruction of the sampling data.

We next introduce the "filtered" matrix, $[V']$, constructed so that it contains only M predominant right-singular vectors of $[V]$;

$$[V'] = [v_1, v_2, \cdots, v_M].$$

(35)

The right-singular vectors from $M+1$ to L, corresponding to the small singular values, are omitted. Therefore,

$$[Y_1] = [U][\sum'][V'_1]^H ,$$

(36)

$$[Y_2] = [U][\sum'][V'_2]^H ,$$

(37)

where $[V_1']$ is obtained from $[V']$ with the last row of $[V']$ omitted, $[V_2']$ is obtained by deleting the first row of $[V']$; and $[\sum']$ is obtained from the M columns of $[\sum]$ corresponding to the M predominant singular values.

B. How to decide β_i

To motivate the MP method, we can use the two $(N-L) \times L$ matrices, Y_1 and Y_2. We can rewrite

$$[Y_2] = [Z_1][R][Z_0][Z_2],$$

(38)

$$[Y_1] = [Z_1][R][Z_2],$$

(39)

where

$$[Z_1] = \begin{bmatrix} 1 & 1 & \cdots & 1 \\ z_1 & z_2 & \cdots & z_M \\ \vdots & \vdots & \cdots & \vdots \\ z_1^{N-L-1} & z_2^{N-L-1} & \cdots & z_M^{N-L-1} \end{bmatrix}_{(N-L) \times M} , \quad (40)$$

$$[Z_2] = \begin{bmatrix} 1 & z_1 & \cdots & z_1^{L-1} \\ 1 & z_2 & \cdots & z_2^{L-1} \\ \vdots & \vdots & \cdots & \vdots \\ 1 & z_M & \cdots & z_M^{L-1} \end{bmatrix}_{M \times L} , \quad (41)$$

$$[Z_0] = diag[z_1, z_2, \cdots, z_M],$$

(42)

$$[R] = diag[R_1, R_2, \cdots, R_M],$$

(43)

where $diag[\bullet]$ represents a $M \times M$ diagonal matrix.

Now, we introduce the matrix pencil

$$[Y_2] - \lambda[Y_1] = [Z_1][R]\{[Z_0] - \lambda[I]\}[Z_2], \quad (44)$$

where $[I]$ is the $M \times M$ identity matrix. We can demonstrate that, in general, the rank of $\{[Y_2] - \lambda[Y_1]\}$ will be M ,

provided $M \le L \le N-M$. However, if $\lambda = z_i$, $i = 1,2,\cdots,M$, the ith row of $\{[Z_0]-\lambda[I]\}$ is zero, and the rank of this matrix is $M-1$. Hence, the parameters z_i , may be found as generalized eigenvalues of the matrix pair $\{[Y_2];[Y_1]\}$. Equivalently, the problem of solving for z_i can be transformed into an ordinary eigenvalue problem,

$$\{[Y_1]^+[Y_2]-\lambda[I]\}, \tag{45}$$

where $[Y_1]^+$ is Moore-Penrose pseudo-inverse of $[Y_1]$, and is defined as

$$[Y_1]^+ = \{[Y_1]^H[Y_1]\}^{-1}[Y_1]^H, \tag{46}$$

where the superscript ``H" denotes the conjugate transpose.

The eigenvalues of the matrix

$$\{[Y_2]-\lambda[Y_1]\}_{L\times M} \Rightarrow \{[Y_1]^+[Y_2]-\lambda[I]\}_{M\times M}, \tag{47}$$

are equivalent to the eigenvalues of the matrix

$$\{[V'_2]^H-\lambda[V'_1]^H\} \Rightarrow \{[V'_1]^H\}^+\{[V'_2]^H\}^+-\lambda[I]. \tag{48}$$

This methodology can be used to solve for z_i .

Lastly, we point out that in this case z_i represents β_i .

C. How to decide α_i

Once M and the z_i are known, α_i , are solved with the help of the following least-squares problem:

$$\begin{bmatrix} f(0) \\ f(1) \\ \vdots \\ f(N-1) \end{bmatrix} = \begin{bmatrix} 1 & 1 & \cdots & 1 \\ z_1 & z_2 & \cdots & z_M \\ \vdots & \vdots & \cdots & \vdots \\ z_1^{N-1} & z_2^{N-1} & \cdots & z_M^{N-1} \end{bmatrix} \begin{bmatrix} \alpha_1 \\ \alpha_2 \\ \vdots \\ \alpha_M \end{bmatrix}. \tag{49}$$

D. Example for MP

The kernel of Green's function of point source lying in the vertical multilayer earth model can be expanded into a sum of complex exponential terms. Generally speaking, only a few terms of quasi-static complex images can arrive at a very high precision. We will show merit of this method through the vertical three-layer earth model.

Earth's conductivities and permittivity's are $\sigma_1 = 100.0^{-1} S/m$, $\sigma_2 = 200.0^{-1} S/m$,

$\sigma_3 = 300.0^{-1} S/m$, $\varepsilon_1 = 5\varepsilon_0$, $\varepsilon_2 = 12\varepsilon_0$, and $\varepsilon_2 = 10\varepsilon_0$, respectively. The middle layer earth thickness is $5m$. With the MP approach, only two terms of the quasi-static complex images can arrive at relative error 0.1% . From Fig. 8 and Fig. 9, we can see that the two curves are superposed to each other, the two terms of quasi-static complex images' coefficients are given in Table 6.
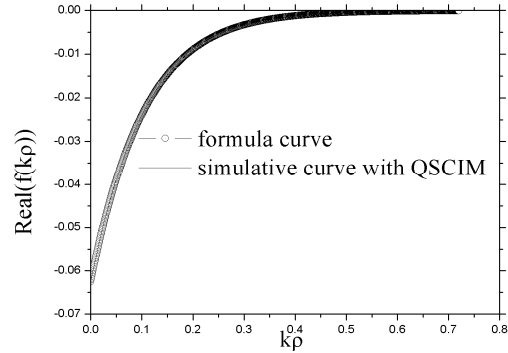

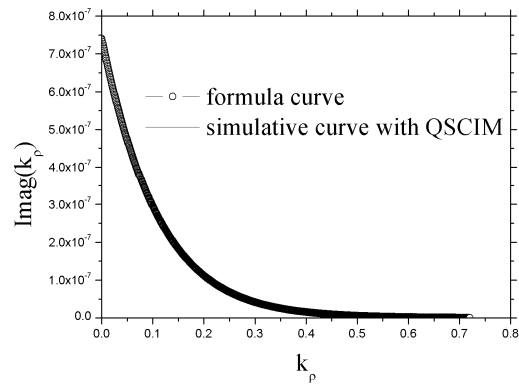Fig. 8. Two curves from function and simulation (real part).

Fig. 9. Two curves from function and simulation (imaginary part).

Table 6: Coefficients of the quasi-static complex images for a vertical, three-layer earth model

i	α_i	β_i
1	6.692e-2-j7.298e-4	10.009-j1.341e-6
2	4.423e-3-j1.451e-3	19.027+j3.627e-5

REFERENCES

[1] M. Mamaoorty, M. M. B. Narayanan, S. Parameswaran, and D. Mukhedkar, "Transient Performance of Grounding Grids," *IEEE Transactions on Power Delivery*, vol. PWRD-4, no. 4, pp. 2053-2059, 1989.

[2] W. Xiong and F. P. Dawalibi, "Transient Performance of Substation Grounding Systems Subjected to Lighting and Similar Surge Currents," *IEEE Transactions on Power Delivery*, vol. PWRD-9, no. 3, pp. 1412-1420, 1994.

[3] M. Heimbach and L. D. Grcev, "Grounding System Analysis in Transient Program Applying Electromagnetic Field Approach," *IEEE Transactions on Power Delivery*, vol. PWRD-12, no. 1, pp. 186-193, 1997.

[4] R. Andolfato, L. Bernardi, and L. Fellin, "Aerial and Grounding System Analysis by the Shifting Complex Images Method," *IEEE Transactions on Power Delivery*, vol. PWRD-15, no. 3, pp. 1001-1009, 2000.

[5] Y. Q Liu, N. Theethayi, and R. Thottappillil, "An Engineering Model for Transient Analysis of Grounding System under Lighting Strikes: Nonuniform Transmission Line Approach," *IEEE Transactions on Power Delivery*, vol. PWRD-20, no. 2, pp. 722-730, 2005.

[6] D. Poljak and V. Doric, "Wire Antenna Model for Transient Analysis of Simple Ground Systems, Part I: The Vertical Grounding Electrode," *Progress In Electromagnetics Research*, vol. PIER 64, pp. 149–166, 2006.

[7] D. Poljak and V. Doric, "Wire Antenna Model for Transient Analysis of Simple Ground Systems, Part I: The Horizontal Grounding Electrode," *Progress In Electromagnetics Research*, vol. PIER 64, pp. 167–189, 2006.

[8] M. Osman Goni, E. Kaneko, and A. Ametani, "Finite Difference Time Domain Method for the Analysis of Transient Grounding Resistance of Buried Thin Wires," *ACES Journal*, vol. 22, no. 3, 2007.

[9] A. F. Otero, J. Cidras, and J. L. Alamo, "Frequency-Dependent Grounding System Calculation by Means of a Conventional Nodal Analysis Technology," *IEEE Transactions on Power Delivery*, vol. PWRD-14, pp. 873-877, 1999.

[10] F. Dawalibi, "Electromagnetic Fields Generated by Overhead and Buried Short Conductors, Part 2-Ground Network," *IEEE Transactions on Power Delivery*, vol. PWRD-1, pp. 112-119, 1986.

[11] L. Huang and D. G. kasten, "Model of Ground Grid and Metallic Conductor Currents in High Voltage A.C. Substations for the Computation of Electromagnetic Fields," *Electric Power Systems Research*, vol. 59, pp. 31-37, 2001.

[12] H. O. Brodskyn, M. C. Costa, J. R. Cardoso, N. M. Abe, and A. Passaro, "Ground-3D Linked to Line Parameters: A Method to Fault Current Distribution and Earth Potential Determination," *ACES Journal*, vol. 12, no. 1, 1997.

[13] Z. X. Li, W. J. Chen, J. B. Fan, and J. Y. Lu, "A Novel Mathematical Modeling of Grounding System Buried in Multilayer Earth," *IEEE transactions on Power Delivery*, vol. PWRD-21, pp. 1267-1272, 2006.

[14] Z. X. Li and W. J. Chen, "Numerical Simulation Grounding System Buried Within Horizontal Multilayer Earth in Frequency Domain," *Communications in Numerical Methods in Engineering*, vol. 23, pp. 11-27, 2007.

[15] Z. X. Li and J. B. Fan, "Numerical Calculation of Grounding System in Low Frequency Domain Based on Boundary Element Method," *International Journal for Numerical Methods in Engineering*, vol. 73, pp. 685-705, 2008.

[16] Z. X. Li, J. B. Fan, and W. J. Chen, "Numerical Simulation of Substation Grounding Grids Buried in Both Horizontal and Vertical Multilayer Earth Model," *International Journal for Numerical Methods in Engineering*, vol. 69, pp. 2359-2380, 2007.

[17] Z. X. Li, G. F. Li, J. B. Fan, and C. X. Zhang, "Numerical Simulation of Grounding System Buried in Vertical Multilayer Earth Model in Low Frequency Domain Based on the Boundary Element Method," *European Transactions on Electrical Power*, vol. 19, pp. 1177-1190, 2009.

[18] L. Zhang, J. Yuan, and Z. X. Li, "The Complex Image Method and its Application in Numerical Simulation of Substation Grounding Grids," *Communications in*

Numerical Methods in Engineering, vol. 15, pp. 835-839, 1999.

[19] Y. L. Chow, J. J. Yang, and K. D. Srivastavaa, "Complex Images of a Ground Electrode in Layered Soils," *Journal of Applied Physics*, vol. 71, pp. 569-574, 1992.

[20] S. Vujevic and M. Kurtovic, "Numerical Analysis of Earthing Grids Buried in Horizontal Stratified Multilayer Earth," *International Journal for Numerical Methods in Engineering*, vol. 41, pp. 1297-1319, 1998.

[21] Y. L. Chow, M. M. Elsherbiny, and M. M. A. Salama, "Surface Voltages and Resistance of Grounding System of Grid and Rods in Two-Layer Earth by the Rapid Galerkin's Moment Method," *IEEE Transactions on Power Delivery*, vol. PWRD-12, pp. 179-185, 1997.

[22] A. P. Sakis Meliopoulos, F. Xia, G. J. Cokkinides, "An Advanced Computer Model for Grounding System Analysis," *IEEE Transactions on Power Delivery*, vol. PWRD-8, no. 1, pp. 13-23, 1993.

[23] L. M. Livshitz, P. D. Einziger, and J. Mizrahi, "A Model of Finite Electrodes in Layered Biological Media: Hybrid Image Series and Moment Method Scheme," *ACES Journal*, vol. 16, no. 2, pp. 145-154, 2001.

[24] R. J. Heppe, "Computation of Potential at Surface Above an Energized Grid or Other Electrode, Allowing for Non-Uniform Current Distribution," *IEEE Transactions on Power Apparatus and System*, vol. PAS-98, no. 6 pp. 1978-1989, 1979.

[25] I. Colominas, F. Navarrina, and M. Casteleiro, "A Boundary Element Numerical Approach for Grounding Grid Computation," *Computer Methods in Applied Mechanics and Engineering*, vol. 174, pp. 73-90, 1999.

[26] U. Adriano, O. Bottauscio, and M. Zucca, "Boundary Element Approach for the Analysis and Design of Grounding Systems in Presence of Non-Homogeneousness," *IEE Proceedings on Generation, Distribution and distribution*, vol.150, no. 3, pp. 360-366, 2003.

[27] P. D. Rancic, L. V. Stefanovic, and D. R. Djordjevic, "An Improved Linear Grounding System Analysis in Two-Layer Earth," *IEEE Transactions on Magnetic*, vol. 32, no. 5, part 3, pp. 5179-5187, 1996.

[28] P. D. Rancic, L. V. Stefanovic, and D. R. Djordevic, "Analysis of Linear Ground Electrodes Placed in Vertical Three-Layer Earth," *IEEE Transactions on Magnetic*, vol. 32, no. 3, pp. 1505-1508, 1996.

[29] Z. X. Li, J. B. Fan, and W. J. Chen, "Numerical Simulation Grounding Grids Buried in Both Horizontal and Vertical Multilayer Earth Model," *International Journal for Numerical Methods in Engineering*, vol. 69, no. 11, pp. 2359-2380, 2007.

[30] J. R. Wait and K. P. Spies, "On the Representation of the Quasi-Static Fields of a Line Current Source above the Ground," *Canadian Journal of Physics*, vol. 47, pp. 2731-2733, 1969.

[31] D. J. Thomson, J. T. Weaver, and et. al, "The Complex Image Approximation for Induction in a Multilayer Earth," *Journal of Geophysical Research*, vol. 80, pp. 123-129, 1975.

[32] J. G. Sverak, W. K. Dick, T. H. Dodds, and R.H. Heppe, "Substations Grounding. Part I," *IEEE Transactions on Power Apparatus and Systems*, vol. PAS-100, no. 9, pp. 4281-4290, 1981.

[33] J. G. Sverak, W. K. Dick, T. H. Dodds, and R.H. Heppe, "Substations Grounding. Part II," *IEEE Transactions on Power Apparatus and Systems*, vol. PAS-101, no. 10, pp. 4006-4023, 1982.

[34] D. L. Garrett and J. G. Pruitt, "Problems Encountered with the Average Potential Method of Analyzing Substation Grounding Systems," *IEEE Transactions on Power Apparatus and Systems*, vol. PAS-104, no. 12, pp. 3586-3596, 1985.

[35] I. Colominas, F. Navarrina, and M. Casteleiro, "A Numerical Formulation for Grounding Analysis in Stratified Soils," *IEEE Transactions on Power Delivery*, vol. PWRD-17, pp. 587-595, 2002.

[36] C. Johnson, *Numerical Solution of Partial Differential Equations by the Finite Element Method*. Cambridge, U.K.: Cambridge Univ. Press, 1987.

[37] E. D. Sunde, *Earth Conduction Effects in Transmission Systems*, Dover Pub., New York, 1968.

[38] R. S. Adve and T. K. Sarkar, "Extrapolation of Time-Domain Responses from Three-Dimensional Conducting Objects Utilizing the Matrix Pencil Technique," *IEEE Transactions*

on Antenna and Propagation, vol. AP-45, no. 1, pp. 147-156, 1997.

[39] T. K. Sakar and O. Pereira, "Using the Matrix Pencil Method to Estimate the Parameters of a Sum of Complex Exponentials," *IEEE antenna and Propagation Magazine*, vol. 37, no. 1, pp. 48-55, February 1995.

Zhong-Xin Li was born in Xi'an, Shaangxi, China. He received the Bachelor's and Master's degree from Xi'an Jiaotong University in 1989 and 1994, respectively, and the Ph.D. degree from Tsinghua University in March 1999.

He joined Fudan University in 1999, first as a Postdoctoral Fellow and then becoming an Associate Professor in 2001. From 2003 to 2004, he was with the Branch of Electromagnetic Environment Research, Electrical Power Research Institute of China. From January 2004 to May 2005, he was with the Department of Electronic Engineering, Hong Kong City University, as a Senior Research Associate. From May 2005 to May 2007, he was an Associate Professor at the Electromagnetic Academy, Zhejiang University. Since May 2007, he has been with the Branch of Overvoltage and Insulation Coordination of the China Electrical Power Research Institute. His special fields of interest included grounding system analysis and high-frequency electromagnetic wave and remote sensing.

Guang-Fan Li received the Master's degree from China Electric Power Research Institute (CEPRI), Beijing, China, in 1983.

He joined CEPRI in 1983, where he is currently the Head of the High Voltage Research Institute. His research interests include ac and dc UHV transmission technology.

Jian-Bin Fan was born in Shanxi Province, China in 1967. He received the B.Sc. and M.Sc. degrees from the Department of Electrical Engineering, Xi'an Jiaotong University, Xi'an China, in 1990 and 1995, respectively. After two years of work in a transformer plant, he studied at China Electric Power Research Institute and received the Ph.D. degree there in 2000.

Currently, he is the Vice Director of High Voltage Department, China Electric Power Research Institute. He is also the Vice Director of Electric Power Industry Quality Inspection & Test Centre. He is the member of IEC SB1 (Electricity transmission and distribution), IEC TC36 WG11, CIGRE B3.22 and so on. He is the Secretary General of National UHV AC Transmission Technology Standardization Committee of China, Vice Secretary General of National HVDC Transmission Technology Standardization Committee of China, and so on. His main research interests include external insulation and operation of high voltage transmission lines and equipment, especially in UHV areas.

Yu Yin was born in March, 1975 in Xi'an city of Shaangxi Province. He graduated from Tsinghua University with Ph.D. in 2004. Since then he joined in the China Electric Power Research Institute. His research interest is high volte technology.

2011 INSTITUTIONAL MEMBERS

DTIC-OCP LIBRARY
8725 John J. Kingman Rd, Ste 0944
Fort Belvoir, VA 22060-6218

AUSTRALIAN DEFENCE LIBRARY
Northcott Drive
Canberra, A.C.T. 2600 Australia

BEIJING BOOK CO, INC
701 E Linden Avenue
Linden, NJ 07036-2495

DARTMOUTH COLLEGE
6025 Baker/Berry Library
Hanover, NH 03755-3560

DSTO EDINBURGH
AU/33851-AP, PO Box 830470
Birmingham, AL 35283

SIMEON J. EARL – BAE SYSTEMS
W432A, Warton Aerodome
Preston, Lancs., UK PR4 1AX

ENGINEERING INFORMATION, INC
PO Box 543
Amsterdam, Netherlands 1000 Am

ETSE TELECOMUNICACION
Biblioteca, Campus Lagoas
Vigo, 36200 Spain

GA INSTITUTE OF TECHNOLOGY
EBS-Lib Mail code 0900
74 Cherry Street
Atlanta, GA 30332

TIMOTHY HOLZHEIMER
Raytheon
PO Box 1044
Rockwall, TX 75087

HRL LABS, RESEARCH LIBRARY
3011 Malibu Canyon
Malibu, CA 90265

IEE INSPEC
Michael Faraday House
6 Hills Way
Stevenage, Herts UK SG1 2AY

INSTITUTE FOR SCIENTIFIC INFO.
Publication Processing Dept.
3501 Market St.
Philadelphia, PA 19104-3302

LIBRARY – DRDC OTTAWA
3701 Carling Avenue
Ottawa, Ontario, Canada K1A OZ4

LIBRARY of CONGRESS
Reg. Of Copyrights
Attn: 407 Deposits
Washington DC, 20559

LINDA HALL LIBRARY
5109 Cherry Street
Kansas City, MO 64110-2498

MISSOURI S&T
400 W 14th Street
Rolla, MO 56409

MIT LINCOLN LABORATORY
Periodicals Library
244 Wood Street
Lexington, MA 02420

NATIONAL CHI NAN UNIVERSITY
Lily Journal & Book Co, Ltd
20920 Glenbrook Drive
Walnut, CA 91789-3809

JOHN NORGARD
UCCS
20340 Pine Shadow Drive
Colorado Springs, CO 80908

OSAMA MOHAMMED
Florida International University
10555 W Flagler Street
Miami, FL 33174

NAVAL POSTGRADUATE SCHOOL
Attn:J. Rozdal/411 Dyer Rd./ Rm 111
Monterey, CA 93943-5101

NDL KAGAKU
C/0 KWE-ACCESS
PO Box 300613 (JFK A/P)
Jamaica, NY 11430-0613

OVIEDO LIBRARY
PO BOX 830679
Birmingham, AL 35283

DAVID PAULSEN
E3Compliance
1523 North Joe Wilson Road
Cedr Hill, TX 75104-1437

PENN STATE UNIVERSITY
126 Paterno Library
University Park, PA 16802-1808

DAVID J. PINION
1122 E Pike Street #1217
SEATTLE, WA 98122

KATHERINE SIAKAVARA
Gymnasiou 8
Thessaloniki, Greece 55236

SWETS INFORMATION SERVICES
160 Ninth Avenue, Suite A
Runnemede, NJ 08078

YUTAKA TANGE
Maizuru Natl College of Technology
234 Shiroya
Maizuru, Kyoto, Japan 625-8511

TIB & UNIV. BIB. HANNOVER
DE/5100/G1/0001
Welfengarten 1B
Hannover, Germany 30167

UEKAE
PO Box 830470
Birmingham, AL 35283

UNIV OF CENTRAL FLORIDA
4000 Central Florida Boulevard
Orlando, FL 32816-8005

UNIVERSITY OF COLORADO
1720 Pleasant Street, 184 UCB
Boulder, CO 80309-0184

UNIVERSITY OF KANSAS –
WATSON
1425 Jayhawk Blvd 210S
Lawrence, KS 66045-7594

UNIVERSITY OF MISSISSIPPI
JD Williams Library
University, MS 38677-1848

UNIVERSITY LIBRARY/HKUST
Clear Water Bay Road
Kowloon, Honk Kong

CHUAN CHENG WANG
8F, No. 31, Lane 546
MingCheng 2nd Road, Zuoying Dist
Kaoshiung City, Taiwan 813

THOMAS WEILAND
TU Darmstadt
Schlossgartenstrasse 8
Darmstadt, Hessen, Germany 64289

STEVEN WEISS
US Army Research Lab
2800 Powder Mill Road
Adelphi, MD 20783

YOSHIHIDE YAMADA
NATIONAL DEFENSE ACADEMY
1-10-20 Hashirimizu
Yokosuka, Kanagawa,
Japan 239-8686

INFORMATION FOR AUTHORS

PUBLICATION CRITERIA

Each paper is required to manifest some relation to applied computational electromagnetics. **Papers may address general issues in applied computational electromagnetics, or they may focus on specific applications, techniques, codes, or computational issues.** While the following list is not exhaustive, each paper will generally relate to at least one of these areas:

1. **Code validation.** This is done using internal checks or experimental, analytical or other computational data. Measured data of potential utility to code validation efforts will also be considered for publication.

2. **Code performance analysis.** This usually involves identification of numerical accuracy or other limitations, solution convergence, numerical and physical modeling error, and parameter tradeoffs. However, it is also permissible to address issues such as ease-of-use, set-up time, run time, special outputs, or other special features.

3. **Computational studies of basic physics.** This involves using a code, algorithm, or computational technique to simulate reality in such a way that better, or new physical insight or understanding, is achieved.

4. **New computational techniques** or new applications for existing computational techniques or codes.

5. **"Tricks of the trade"** in selecting and applying codes and techniques.

6. **New codes, algorithms, code enhancement, and code fixes.** This category is self-explanatory, but includes significant changes to existing codes, such as applicability extensions, algorithm optimization, problem correction, limitation removal, or other performance improvement. **Note: Code (or algorithm) capability descriptions are not acceptable, unless they contain sufficient technical material to justify consideration.**

7. **Code input/output issues.** This normally involves innovations in input (such as input geometry standardization, automatic mesh generation, or computer-aided design) or in output (whether it be tabular, graphical, statistical, Fourier-transformed, or otherwise signal-processed). Material dealing with input/output database management, output interpretation, or other input/output issues will also be considered for publication.

8. **Computer hardware issues.** This is the category for analysis of hardware capabilities and limitations of various types of electromagnetics computational requirements. Vector and parallel computational techniques and implementation are of particular interest.

Applications of interest include, but are not limited to, antennas (and their electromagnetic environments), networks, static fields, radar cross section, inverse scattering, shielding, radiation hazards, biological effects, biomedical applications, electromagnetic pulse (EMP), electromagnetic interference (EMI), electromagnetic compatibility (EMC), power transmission, charge transport, dielectric, magnetic and nonlinear materials, microwave components, MEMS, RFID, and MMIC technologies, remote sensing and geometrical and physical optics, radar and communications systems, sensors, fiber optics, plasmas, particle accelerators, generators and motors, electromagnetic wave propagation, non-destructive evaluation, eddy currents, and inverse scattering.

Techniques of interest include but not limited to frequency-domain and time-domain techniques, integral equation and differential equation techniques, diffraction theories, physical and geometrical optics, method of moments, finite differences and finite element techniques, transmission line method, modal expansions, perturbation methods, and hybrid methods.

Where possible and appropriate, authors are required to provide statements of quantitative accuracy for measured and/or computed data. This issue is discussed in "Accuracy & Publication: Requiring, quantitative accuracy statements to accompany data," by E. K. Miller, *ACES Newsletter,* Vol. 9, No. 3, pp. 23-29, 1994, ISBN 1056-9170.

SUBMITTAL PROCEDURE

All submissions should be uploaded to ACES server through ACES web site (http://aces.ee.olemiss.edu) by using the upload button, journal section. Only pdf files are accepted for submission. The file size should not be larger than 5MB, otherwise permission from the Editor-in-Chief should be obtained first. Automated acknowledgment of the electronic submission, after the upload process is successfully completed, will be sent to the corresponding author only. It is the responsibility of the corresponding author to keep the remaining authors, if applicable, informed. Email submission is not accepted and will not be processed.

EDITORIAL REVIEW

In order to ensure an appropriate level of quality control, papers are peer reviewed. They are reviewed both for technical correctness and for adherence to the listed guidelines regarding information content and format.

PAPER FORMAT

Only camera-ready electronic files are accepted for publication. The term **"camera-ready" means that the material is neat, legible, reproducible, and in accordance with the final version format listed below.**

The following requirements are in effect for the final version of an ACES Journal paper:

1. The paper title should not be placed on a separate page.

The title, author(s), abstract, and (space permitting) beginning of the paper itself should all be on the first page. The title, author(s), and author affiliations should be centered (center-justified) on the first page. The title should be of font size 16 and bolded, the author names should be of font size 12 and bolded, and the author affiliation should be of font size 12 (regular font, neither italic nor bolded).

2. An abstract is required. The abstract should be a brief summary of the work described in the paper. It should state the computer codes, computational techniques, and applications discussed in the paper (as applicable) and should otherwise be usable by technical abstracting and indexing services. The word "Abstract" has to be placed at the left margin of the paper, and should be bolded and italic. It also should be followed by a hyphen (─) with the main text of the abstract starting on the same line.

3. All section titles have to be centered and all the title letters should be written in caps. The section titles need to be numbered using roman numbering (I. II. ….)

4. Either British English or American English spellings may be used, provided that each word is spelled consistently throughout the paper.

5. Internal consistency of references format should be maintained. As a guideline for authors, we recommend that references be given using numerical numbering in the body of the paper (with numerical listing of all references at the end of the paper). The first letter of the authors' first name should be listed followed by a period, which in turn, followed by the authors' complete last name. Use a coma (,) to separate between the authors' names. Titles of papers or articles should be in quotation marks (" "), followed by the title of journal, which should be in italic font. The journal volume (vol.), issue number (no.), page numbering (pp.), month and year of publication should come after the journal title in the sequence listed here.

6. Internal consistency shall also be maintained for other elements of style, such as equation numbering. Equation numbers should be placed in parentheses at the right column margin. All symbols in any equation have to be defined before the equation appears or right immediately following the equation.

7. The use of SI units is strongly encouraged. English units may be used as secondary units (in parentheses).

8. Figures and tables should be formatted appropriately (centered within the column, side-by-side, etc.) on the page such that the presented data appears close to and after it is being referenced in the text. When including figures and tables, all care should be taken so that they will appear appropriately when printed in black and white. For better visibility of paper on computer screen, it is good to make color figures with different line styles for figures with multiple curves. Colors should also be tested to insure their ability to be distinguished after black and white printing. Avoid the use of large symbols with curves in a figure. It is always better to use different line styles such as solid, dotted, dashed, etc.

9. A figure caption should be located directly beneath the corresponding figure, and should be fully justified.

10. The intent and meaning of all text must be clear. For authors who are not masters of the English language, the ACES Editorial Staff will provide assistance with grammar (subject to clarity of intent and meaning). However, this may delay the scheduled publication date.

11. Unused space should be minimized. Sections and subsections should not normally begin on a new page.

ACES reserves the right to edit any uploaded material, however, this is not generally done. It is the author(s) responsibility to provide acceptable camera-ready files in pdf and MSWord formats. Incompatible or incomplete files will not be processed for publication, and authors will be requested to re-upload a revised acceptable version.

COPYRIGHTS AND RELEASES

PUBLICATION CHARGES

ACES Journal is abstracted in INSPEC, in Engineering Index, DTIC, Science Citation Index Expanded, the Research Alert, and to Current Contents/Engineering, Computing & Technology.